Institut für Neurowissenschaften,

Technische Universität München

Development of a deep two-photon calcium imaging method for the analysis of cortical processing in the mammalian brain

Antje Birkner

Vollständiger Abdruck der von der Fakultät für Medizin der Technischen Universität München zur Erlangung des akademischen Grades eines

Doktors der Naturwissenschaften (Dr. rer. nat.)

genehmigten Dissertation.

Vorsitzender: Prof. Dr. Claus Zimmer

Prüfer der Dissertation:

        1. Prof. Dr. Arthur Konnerth

        2. Prof. Dr. Andreas Bausch

        3. Prof. Dr. Laura Busse

Die Dissertation wurde am 24.04.2018 bei der Fakultät für Medizin der Technischen Universität München eingereicht und durch die Fakultät für Medizin am 13.12.2018 angenommen.

Abstract

Two-photon microscopy is the major tool for investigating single-cell function of brain cells *in vivo*. The nonlinearity of two-photon excitation restricts the fluorescence generation to the focal spot of the laser light beam, which is scanned across the sample. Thin optical sections of the sample are thereby created, resulting in images with single-cell resolution deep inside biological tissue. Despite the increased depth penetration compared to confocal microscopy, for example, the imaging depth is still limited to a few hundred micrometers. In the present study, a new method was developed to overcome this limit, which is based on two major strategies: the reduction of excitation light scattering by using laser light with long wavelengths (> 1000 nm) and the minimization of out-of-focus fluorescence. A new two-photon microscope was setup, optimized for deep imaging with red-shifted excitation wavelengths and for enhanced fluorescence generation and detection from deep inside the brain tissue. Subsequently, a new commercially available red-emitting calcium dye was introduced and characterized with *in vivo* experiments. For increasing the imaging depth by use of this dye, it was crucial to minimize the background fluorescence excited in superficial cortical layers. Therefore, a new visually-guided staining approach was developed, which spatially restricts the labeled cell volume to the cell layer of interest and spares the surrounding tissue. The combination of the red-shift, the optimized two-photon setup and the local staining procedure, allowed for functional two-photon imaging *in vivo*, down to ~900 µm below the surface, corresponding to the deepest cortical layer, layer 6, of the mouse brain. The new deep imaging approach was used to study sensory-evoked activity in layer 5 neurons of the barrel cortex of the anesthetized or awake behaving mouse. Interestingly, only 5% of the recorded neurons responded to the sensory stimulation with large signal amplitudes and with high response probabilities. These cells were defined here as 'super-responding' (SR) neurons. To further analyze the SR neurons, the new deep imaging approach was combined with more classical techniques, allowing for multi-color imaging, simultaneous electrical recordings and pharmacological manipulations. The experimental results suggest that glutamatergic inputs to the dendritic tufts in layer 1 of the SR neurons are responsible for regenerative calcium spikes initiated at the main bifurcation of the tuft dendrites. The calcium spikes determined the strong output firing of the SR neurons in response to sensory stimulation. These new insights about cell population coding and single-cell processing of sensory inputs of cortical layer 5 neurons were only made possible by the new, versatile deep two-photon calcium imaging method introduced here.

Abbreviations

AM	acetoxymethyl
AMPA-R	α-amino-3-hydroxy-5-methyl-4-isoxazolepropionic acid receptor
AOD	acousto-optical deflector
AP	action-potential
AP5	NMDA-receptor blocker d(-)-2-amino-5-phosphonovaleric acid
CNQX	AMPA-receptor blocker 6-cyano-7-nitroquinoxaline-2,3-dione
GaAsP	gallium arsenide phosphide
GABA	γ-aminobutyric acid
GCaMP	genetically-encoded calcium indicator protein containing circularly permutated green fluorescent protein, calmodulin and calmodulin-binding domain from the myosin light chain kinase
HPD	hybrid photodetector
M1	primary motor cortex
NA	numerical aperture
NIR	near-infrared
NMDA-R	N-methyl-D-aspartate receptor
PMT	photomultiplier tube
POm	posterior medial nucleus of the thalamus
RCaMP	red-shifted GCaMP variant
ROI	region-of-interest
S2	secondary somatosensory cortex
SD	standard deviation
SEM	standard error mean
SNR	signal-to-noise ratio
SR	super-responding
Ti:Sa	Titanium:Sapphire
VPM	ventral posterior medial nucleus of the thalamus

Table of contents

1   Introduction

Two-photon fluorescence laser-scanning microscopy is the method of choice for imaging living brain cells in the intact mouse brain of the anesthetized or even awake behaving animal (for review see, for example, (Rochefort *et al.*, 2008; Grienberger & Konnerth, 2012)). Neuronal populations, single cells or even subcellular structures can be visualized morphologically and functionally in real time and with high sensitivity and high spatial resolution (for example (Stosiek *et al.*, 2003; Chen *et al.*, 2012a)). Neurons and glial cells can be imaged during sensory processing, development, during active manipulations, either under healthy or pathological conditions such as Alzheimer disease (for example (Busche *et al.*, 2008)). But between the theoretical prediction of multi-photon excitation 85 years ago by Goeppert-Mayer (Goeppert-Mayer, 1931) and two-photon calcium imaging *in vitro* and *in vivo* more than 60 years have passed. Many technical developments were necessary without any of each functional two-photon imaging would not be possible. First of all, Goeppert-Mayer's theoretical prediction of two-photon absorption had to be demonstrated in practice, which was highly unlikely regarding the low cross-sections of this second-order process in the range of 10^{-50} cm^4s or 1 GM. Thus a very high photon flux is needed for efficient two-photon excitation that could only be achieved with lasers that were invented in 1960 (Maiman, 1960). Considering the huge range of applications for lasers today the importance of the invention of the first laser can hardly be overestimated. But at that time this relevance was not anticipated with Maiman's scientific article covering only half a page of the journal. Only one year later, in 1961, two-photon excitation of $CaF^2{:}Eu^{2+}$ fluorescence was shown by Kaiser and colleagues (Kaiser & Garrett, 1961). The combination with microscopy was invented by Winfried Denk who demonstrated the first two-photon laser-scanning fluorescence microscopy in 1990 (Denk *et al.*, 1990). Its application to calcium imaging in living brain tissue (Stosiek *et al.*, 2003) (for review (Grienberger & Konnerth, 2012)) made two-photon microscopy popular and opened a door in biology and medicine to gain more insight into biological processes in living tissue under health and disease.

1.1   Objectives and structure of the thesis

Even though the penetration depth of two-photon microscopy is large compared to confocal microscopy, for example, it is still limited to few hundreds of micrometers in the living brain tissue (Helmchen & Denk, 2005). In the mouse brain, functional imaging of dense cell populations is mainly restricted to the upper three of six cortical cells layers. The main objective of this thesis was the increase of the maximum two-photon imaging depth to provide direct access to all cortical layers of the mouse brain *in vivo*. Layer 5 was of special interest, as it is the main output cell layer of the cortex. Most of the previous studies of cortical layer 5 relied on traditional extracellular recordings of action-potential activity (Hubel,

1957). These recordings are strongly biased towards active cells whereas weakly responding or not-responding neurons remain undiscovered (Shoham *et al.*, 2006). Accurate population response distributions to sensory stimuli could thus not be provided. A more recent approach to overcome this problem is blind patching of multiple single cells, which are randomly chosen (O'Connor *et al.*, 2010; Velez-Fort *et al.*, 2014). However, only one neuron at a time can be recorded with this method and the activity of the surrounding cells is undetected. To represent the enormous diversity of single-cell responses across dense cell populations (for example (Hromadka *et al.*, 2008; O'Connor *et al.*, 2010)) with single-cell attach recordings is thus challenging. In addition, layer 5 neurons span dendrites across almost all cortical layers and are in principle able to integrate information from multiple brain regions. Previous studies analyzed dendritic signaling of these cells *in vivo* by imaging just the most superficial dendrites of these cells (Xu *et al.*, 2012; Takahashi *et al.*, 2016), limited by the imaging depth limit of two-photon microscopy. In this work presented here, a new method to directly access all cortical layers of the mouse brain *in vivo* with two-photon imaging was developed and applied to the investigation of sensory processing of cortical layer 5 cells on a cellular and subcellular level.

Before establishing a new strategy for deep imaging, the current imaging depth limit was determined experimentally. Afterwards, a first attempt to increase the imaging depth was initiated by implementing three-photon microscopy. Subsequently, a new two-photon microscope was set up, with new two-photon excitation laser sources and optics optimized for long-wavelength excitation, up to 1300 nm. In combination with optimized experimental procedures and a red-shifted calcium indicator, which became recently commercially available, the imaging depth was increased from ~300 to ~900 µm below the cortical surface. This means, the deepest cell layer, layer 6, of the mouse primary visual cortex was accessible for functional imaging with single-cell resolution. It was also shown that these recordings are not limited to experiments with anesthetized animals, but can also be performed with awake behaving animals. These experiments were finally used to address the initial scientific question and new insights about layer 5 coding of sensory inputs were elucidated. It turned out that only a small subset of cells shows salient responses to specific sensory stimuli. Possible reasons for this unique response pattern of these few cells were identified by multi-color imaging and the combination of calcium imaging with electrophysiology plus pharmacological manipulations. The detailed results are provided in the last part of the thesis. Before presenting the results, background information is provided in the following sections about basic concepts of two-photon microscopy, its implementation and limitations, as well as about the mouse whisker system, cortical layer 5 and dendritic computation.

1.2 Two-photon fluorescence microscopy

1.2.1 Basic principles of two-photon microscopy

(The basic principle of two-photon microscopy is well described in (So *et al.*, 2000; Masters & So, 2008) and is shortly summarized in the following.)

For fluorescence emission, a fluorophore needs to undergo a molecular transition from the ground to an excited electronic state. Some of the absorbed energy is converted to heat by vibrational relaxation before the electrons fall back to the ground state under emission of a photon. The emitted photon has the energy corresponding to the gap between the lowest vibrational level of the excited state and ground state and is thus lower than the energy of the excitation photon. The associated shift to a longer wavelength is called Stoke's shift.

For two-photon excitation, two photons with approximately half the energy of the energy gap between ground and excited state are absorbed by the fluorophore almost simultaneously. In case of green emitting fluorescence molecules two photons with a wavelength in the near-infrared range are absorbed instead of a single one with a wavelength in the blue or UV range. Thereby, the first photon excites the molecule to a virtual intermediate state and the second photon excites the molecule to the final excited state, but only if it is absorbed before the decay of the virtual state that is in the range of 10^{-16} s. To increase the probability of this rare event an extremely high photon flux in the range of GW/cm^2 is necessary, whereby the two-photon absorption rate depends on the square of the excitation light intensity. At the same time the average laser power should not exceed values which can be tolerated by the tissue without photodamage. To achieve high laser intensities at low average power values the laser light needs to be concentrated in space and time. Therefore, the laser light source used for two-photon excitation is pulsed and focused by high NA objective lenses. Under these experimental configurations, the number of photon pairs being absorbed by a fluorophore depends on the square of the incident average laser power and is inversed proportional to the time width of a single laser pulse τ and to the square of the pulse repetition rate f. Hence, the more photons within a single pulse and within a short time the higher the chance of two-photon absorption (Denk *et al.*, 1990):

$$n_a \sim \frac{\langle P \rangle^2}{\tau f^2} \left(\frac{(NA)^2}{2\hbar c \lambda} \right)^2 \qquad (1)$$

Compared to single-photon absorption, two-photon absorption has multiple advantages for imaging highly scattering biological tissue. The squared dependence of two-photon absorption on the excitation light intensity confines the volume that is excited to a size down to ~0.1 μm^3 (Zipfel *et al.*, 2003). This leads to an improved depth discrimination and low fluorescence background and hence to a good signal-to-noise ratio (SNR) in scattering

media. The resulting images created are optical sections of the sample with high image contrast (Denk *et al.*, 1990). Another advantage of the restricted volume of excitation is that the place of origin of the emitted photons is well defined by the excitation spot. A pinhole used in confocal microscopy is thus not required and all photons detected contribute to the signal, regardless of scattering (Denk *et al.*, 1990). Furthermore, the spectral difference between excitation and emission light is way larger in case of two-photon compared to single-photon excitation. Consequently, the fluorescence emission can be well separated from the excitation light without any cut-off by optical filters. Another advantage of the confined small volume of two-photon excitation is the reduced region of photointeraction minimizing the place of photodamage and photobleaching (Denk *et al.*, 1990). Those are further reduced by the red-shifted wavelengths compared to single-photon excitation light. In addition, NIR light penetrates deeper into the tissue, in consequence of reduced scattering and absorption of the excitation light (So *et al.*, 2000; Zipfel *et al.*, 2003; Helmchen & Denk, 2005).

1.2.2 Implementation of a two-photon laser-scanning fluorescence microscope

The three major building blocks of a two-photon laser scanning microscope are a pulsed near-infrared laser light source for fluorescence excitation, a laser light scanner including scan mirrors and optics for excitation light deflection and the light detection unit for collecting and detecting the fluorescence. In fig. 1 a generic two-photon setup is illustrated. The excitation light emitted by a pulsed laser light source enters an electro-optical modulator which is used to adjust the laser power at the sample. Following the laser beam the next component is a laser shutter that blocks the laser light in between imaging trials. A telescope enlarges the laser beam diameter usually to be slightly larger than the back aperture of the objective lens. The enlarged laser beam hits two scan mirrors that deflect the beam horizontally and vertically parallel to the sample surface. Behind the scan mirrors the laser beam passes through the scan and tube lens resulting in a collimated beam which enters the back aperture of the objective lens under different scan angles. A dichroic mirror is positioned between tube and objective lens which transmits the excitation and reflects the emission light. The objective lens focuses the laser light into the specimen and also collects the fluorescence emission light. The fluorescence is reflected by the dichroic mirror and focused onto the single-photon detector by a convex optical lens. On its way, the fluorescence light passes an optical filter, which serves as a barrier for the scattered excitation light. The individual components of a two-photon microscope are explained in more detail in the following section.

Diagram of a two-photon laser-scanning microscope
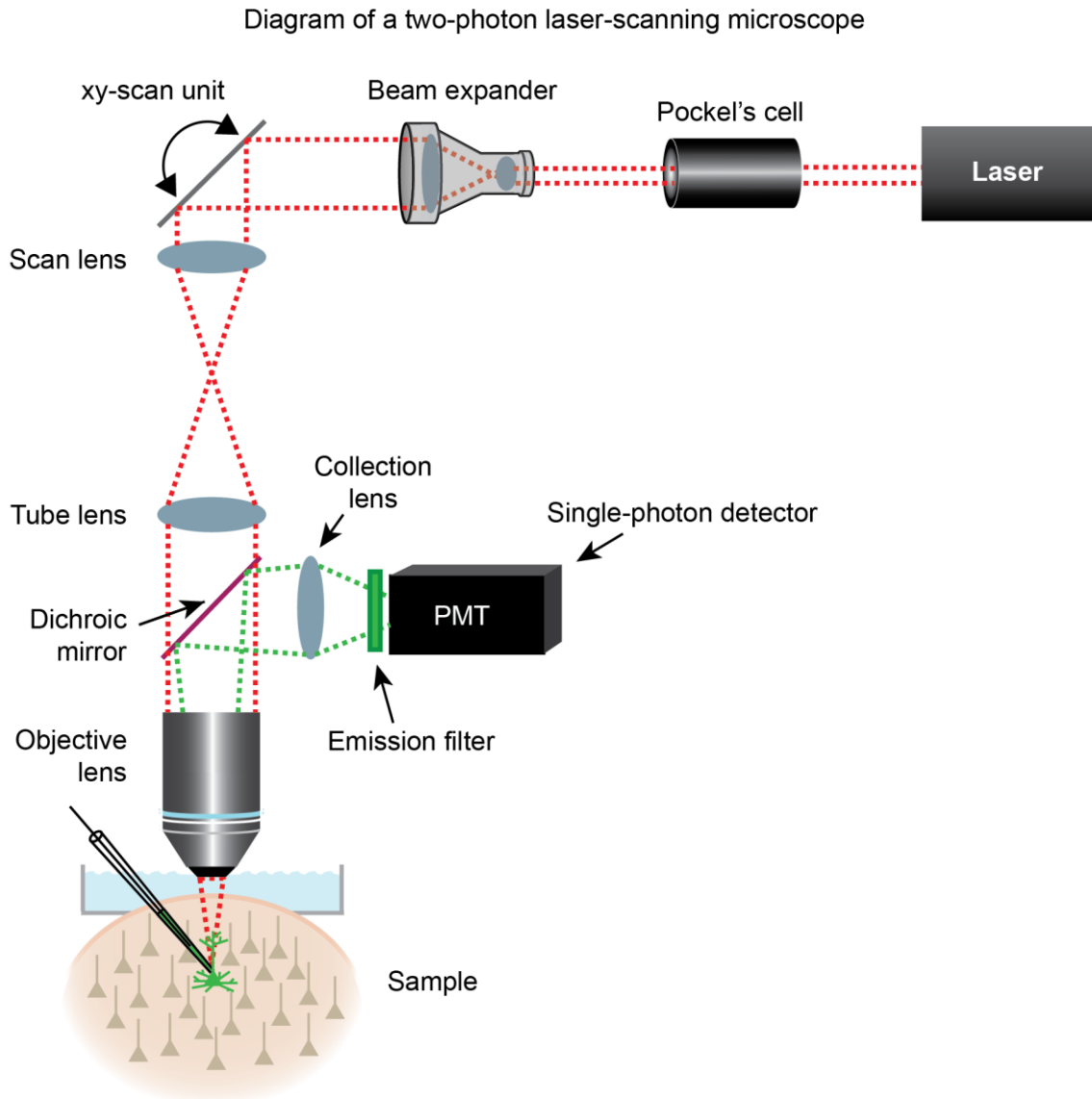
Fig. 1 *Scheme of a generic two-photon microsope. The laser light source emits near-infrared laser pulses in the femtosecond range and with a repetition rate in the megahertz range. A Pockel's cell varies the laser light power to adjust the amount of laser light entering the sample surface and to set the laser light power to a minimum at the turning points of the resonance scanner, to lower the risk of photodamage. A beam expander adjusts the diameter of the laser beam. The scanner unit, consisting of a resonance and a standard galvanometric mirror, deflects the laser light in x- and y-direction. The scan and tube lens form a collimated beam entering the back aperture of the objective lens. The objective lens focuses the laser light onto a small focal spot, which is scanned across the sample. The excited fluorescence light travels back through the objective lens and is focused onto the single-photon detector with a collection lens. In front of the detector, an emission filter is placed to block backscattered laser light.*

1.2.2.1 Laser and prechirper

The standard and most widely used two-photon excitation laser light source is a Titanium:Sapphire (Ti:Sa) laser, emitting laser pulses of a temporal width in the range of ~100 fs, with a repetition rate of ~80 MHz, with an average laser power between 1 W and 3 W and a spectral tuning range covering approximately 680 nm to 1100 nm. The standard wavelength range for classical two-photon calcium imaging is roughly between 800 nm and 950 nm, for the excitation of OGB-1 or GCaMPs for example (Mutze *et al.*, 2012). The

emission peak of Ti:Sa lasers is at 800 nm, which matches well the optimal two-photon excitation wavelengths of standard calcium indicators. Towards the red-wavelength end of the emission spectrum of Ti:Sa lasers the output laser power decreases steeply, as indicated in fig. 2. Towards the long-wavelength end of the spectrum the laser power is too low to be used for two- or three-photon excitation *in vivo*. To figure out the longest wavelength emitted by a Ti:Sa laser which can still be used for two- or three-photon microscopy *in vivo*, the maximum laser power under the objective lens needs to be considered. Most of the laser power is consumed by the optics of the microscope. The microscope used here, which includes a Pockel's cell, a beam expander, silver mirrors and an objective lens, has a laser power throughput of 25% - 30%. To guarantee enough laser power for deep imaging *in vivo* the maximum laser power under the objective lens should reach 200 mW and thus the minimal output laser power should be ~700 mW (as indicated with a grey dashed line in fig. 2). The wavelength range that can be used effectively here is 700 - 1000 nm.
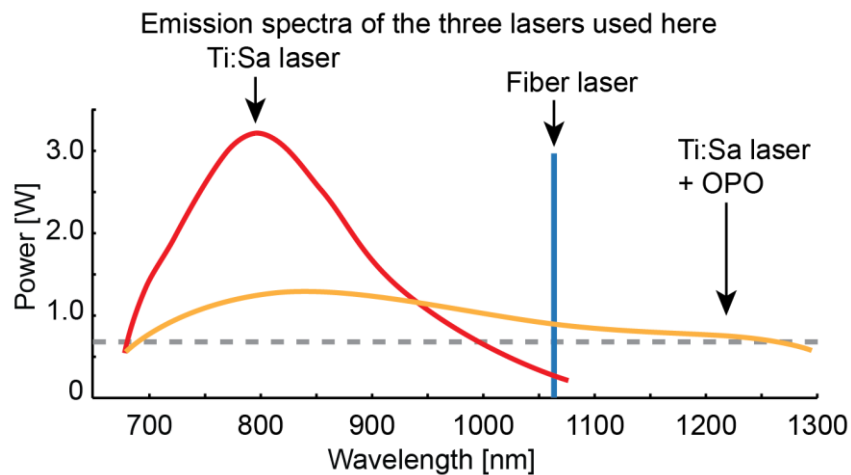
Fig. 2 *Emission spectra of the three laser light sources used here. The spectrum of a Ti:Sa laser is displayed in red (Mai Tai DeepSee eHP, Spectra-Physics), that one of a one-box-solution including an optical parametric oscillator is indicated in orange (Insight; Spectra-Physics) and the single-wavelength emitting fiber laser is marked in blue (Fidelity-2; Coherent). Note that the fiber laser does not emit a single wavelength, like a continuous-wave (CW) laser. It emits laser pulses in the femtosecond range, which causes a broadening of its spectrum (here with a full-width-at-half-maximum of 70 nm ± 10 nm (Fidelity-2; Coherent)). The spectra were adapted from online information about commercially available lasers.*

For the use of excitation wavelengths beyond 1000 nm, alternative laser light sources were used in this study: A one-box system of a Ti:Sa laser and an optical parametric oscillator (OPO), which covers a wavelength range between 680 nm and 1300 nm and a Ytterbium doped fiber laser with a fixed wavelength at 1070 nm (fig. 2 and methods). Fiber lasers have multiple advantages, including robustness, low cost and no need of water cooling (Xu & Wise, 2013).

The temporally extremely short laser pulses of the two-photon laser light sources cannot have a narrow spectral bandwidth following Heisenberg's uncertainty principle:

$$\Delta\tau\Delta\upsilon \geq K \qquad (2)$$

$\Delta\tau$ is the temporal width, $\Delta\upsilon$ is the spectral width and K is a constant that equals 0.441 in the case of Gaussian shaped pulses. By rewriting this formula, the minimal spectral width in nanometers can be calculated: $\Delta\tau\Delta\lambda\left(c/{\lambda_0}^2\right) \geq K => \Delta\lambda \geq \frac{K}{\Delta\tau\left(c/{\lambda_0}^2\right)}$, with the central wavelength λ_0 and the speed of light c. For a central wavelength of 920 nm and a temporal width of 100 fs, the laser pulses cover a wavelength range of 12 nm. Whenever these laser pulses propagate through dispersive material, such as glass, the longer wavelengths travel faster than the shorter ones, leading to a pulse broadening called group velocity dispersion (fig. 3 A) (Zipfel *et al.*, 2003; Helmchen & Denk, 2005). For high two-photon absorption efficiency, this pulse broadening effect has to be compensated by a so-called prechirper. In most cases, prechirpers consist of prism pairs or gratings which introduce a negative chirp to the laser pulses (Muller *et al.*, 1998; Zipfel *et al.*, 2003; Helmchen & Denk, 2005). Hence, short wavelengths of the pulses get a head start compared to the longer wavelengths and after passing through the dispersive parts of the microscope the different wavelengths arrive at the sample simultaneously, as illustrated in fig. 3 B.

A   Effect of group velocity dispersion on the propagation of
femtosecond laser pulses in glass

Laser

| Initial short | Dispersive optical | Broadened |
| pulse | element | pulse |

B   Basic principle of a prechirper

| Initial short | Prechirper | Prechirped | Short pulse |
| pulse | | pulse | at the sample |
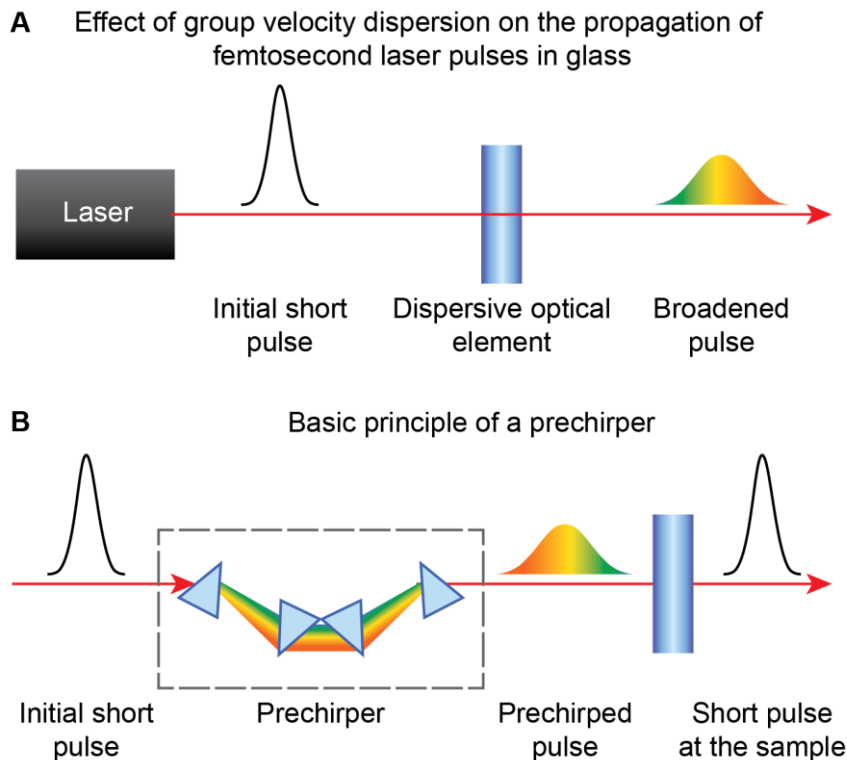
Fig. 3 Compensation of group velocity dispersion with a prechirper. *(A)* Schematic display of group velocity dispersion in a two-photon microscope. The initial laser pulse is spectrally broadened by dispersive optical components of the microscope. *(B)* Compensation of group velocity dispersion. A set of prisms (or gratings) spreads the laser light pulse into its spectral components, which travel different distances within the prechirper. The 'head start' of the short wavelength components (indicated in blue) leads to a pre-compensation of the group velocity dispersion induced by the microscope's optics.

The advantage of using prism pairs in a prechirper compared to gratings is that the group velocity dispersion compensation can be flexibly adjusted by rotating the prisms with stepper motors. Whenever optics of the microscope are replaced or the excitation wavelength is changed, a readjustment of the prechirper setting is required and thus prism pairs are in preference over gratings. In many Ti:Sa laser systems the prechirper is preinstalled and the amount of prechirp can be adjusted easily with a remote control or a software. By changing the value of dispersion compensation the brightness of the generated two-photon image varies according to the pulse width at the location of the sample. The optimal compensation value is achieved when the image brightness is maximal.

1.2.2.2 Objective lens

The objective lens in a two-photon microscope needs to fulfill many requirements to be suitable for two-photon imaging. For example, a high transparency for the excitation laser light is essential, but also for the fluorescence emission, which is spectrally far from the excitation light. Usually, a compromise on the excitation side is favored because the laser power of the excitation light can usually be increased easily whereas the fluorescence signal is limited to few photons. Thus, the objective lens has to collect as many fluorescence photons as possible. For this purpose, an objective lens with comparably low magnification,

large clear apertures and high numerical aperture would be ideal (Oheim *et al.*, 2001). In addition, a water immersion objective lens should be used to reduce the refractive index mismatch between objective lens and specimen. Moreover, a long working distance is required to be able to image deep inside the biological tissue and to guarantee enough space between objective lens and specimen for introducing a glass pipette if necessary. Here, glass pipettes are inserted into the tissue under visual guidance to target single-cells for electrophysiological recordings, pharmacological manipulations or single-cell electroporation, for example. Therefore, the patch-pipette has to enter the brain tissue under a quite steep angle, to ensure that the traveling distance for the pipette into deep cortical layers won't be impractically long. Thus, the housing geometry of the objective lens needs to be taken into account as well.

1.2.2.3 Scanner

To generate a two-dimensional image with a laser light beam focused onto a single point, it needs to be scanned across the sample. Consequently, the beam is deflected from left to right (x-axis) with high speed and from top to bottom at slower speed, as illustrated in fig. 4. The easiest configuration of the scanner unit is the combination of two galvanometric mirrors moving linearly at variable frequencies. The maximum scan speed is limited by the maximum amount of power that the actuator can dissipate. A scan mirror vibrating at its resonant frequency requires much less power and can thus oscillate at much higher frequencies or larger scan angles (Leybaert *et al.*, 2005). But compared to the linear moving galvanometric mirrors a resonant mirror changes its angle in a sinusoidal manner. Thus, in the center of the field-of-view, the speed of the sweeping beam is much faster than at the turning points leading to different pixel dwell times depending on the beam position (Leybaert *et al.*, 2005). To generate a non-distorted image, the pixels need to be reconstructed accordingly. This only applies for the x-axis, because the slower y-axis is usually scanned with a galvanometric mirror.
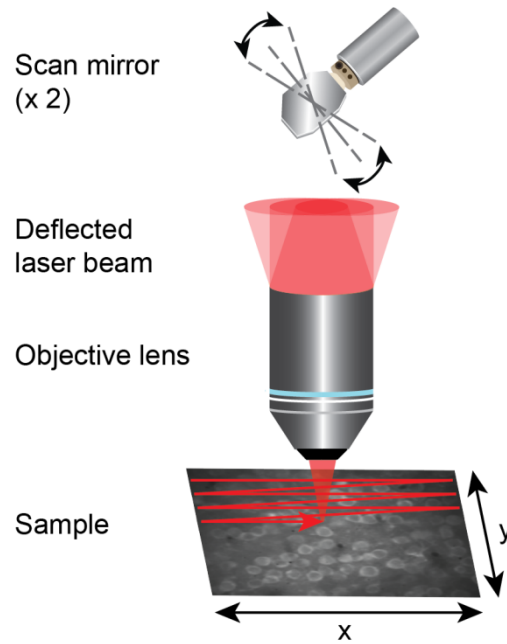
Fig. 4 *Principle of two-dimensional scanning of a focused laser beam. The two scan mirrors rotate around their axis and change the angle of entrance of the collimated beam. One of the mirrors scans the x-axis, while the second one moves the beam along the y-axis.*

Even higher scan frequencies than with resonance scanners can be achieved by deflecting the excitation beam with an acousto-optical deflector (AOD), usually consisting of a TeO_2 crystal and a piezo-transducer creating acoustic waves inside the crystal (Xu & Stroud). These pressure waves change the refractive index inside the crystal periodically and thus act as an optical grating which diffracts the incoming laser. If the incoming beam enters the AOD under the Bragg angle θ_B only the first order of diffraction is observed because higher orders undergo destructive interference (Xu & Stroud). The angle of deflection is then twice the Bragg angle $2\theta_B$ and depends on the frequency of the acoustic wave f_a (Xu & Stroud):

$$\theta_B \approx \lambda/2\Lambda = \lambda f_a/2v_a \tag{3}$$

λ Wavelength of the laser light

Λ acoustic wavelength

f_a is the acoustic frequency

v_a is the acoustical velocity of the crystal material

When changing the frequency of the sound wave inside the crystal the angle of deflection changes as well which enables fast scanning of the incoming beam. In combination with a galvanometric mirror to scan the slow y-axis, images with 250 x 80 pixels were acquired at a frame rate of 1000 Hz (Chen *et al.*, 2011; Chen *et al.*, 2012a). This setup was applied

successfully to *in vivo* imaging of single-cell and even of single spine activity (Chen *et al.*, 2011; Chen *et al.*, 2012a). More recently, a combination of several AODs was used to access random points in a three-dimensional space and applied to *in vivo* calcium imaging even in the awake behaving mouse (Duemani Reddy *et al.*, 2008; Nadella *et al.*, 2016).

Despite these advantages, AODs are not used here, because the drawback of this light scanning method is its wavelength-dependency (equation (3)). Each time the excitation wavelength is changed, the laser beam path needs to be adjusted. For the development of a new deep imaging approach here, the excitation wavelength has to be flexibly changed. Thus, a resonance scanner, consisting of silver-coated mirrors seems to be the best choice, taking into account that current resonance scanners perform well for high-speed scanning. The maximum imaging speed of the system used here is a frame rate of 500 Hz to record images with 240 x 48 pixels.

1.2.2.4 Pockel's cell

The resonance scanner moves the laser beam in a sinusoidal manner across the sample leading to long pixel dwell times at the turning points. To avoid tissue damage at the image borders the laser power must be reduced to a minimum each time reaching the image edges. Therefore, either an acousto-optical modulator (AOM) or a Pockel's cell is fast enough to turn the laser power down twice a line of an image (Pawley, 2006; Masters & So, 2008). An AOM is in principle the same as an AOD but instead of the frequency of the acoustic wave, the amplitude is the variable parameter that, to change the laser power. The disadvantage of an AOM compared to a Pockel's cell is the wavelength dependency of its laser light deflection angle and hence a Pockel's cell is more flexible in use. A Pockel's cell is an electro-optical element based on a birefringent crystal with an electrical field applied. By changing the electrical field, the birefringence and thus the polarization of the beam changes proportionally (Pawley, 2006; Masters & So, 2008). Combined with polarizers the Pockel's cell can be used to vary the laser power rapidly for edge protection. Moreover, the laser power can be changed instantaneously by the experimenter during the experiment which is necessary because only little laser power is needed at the surface of the sample compared to imaging deep inside the tissue.

1.2.2.5 Single-photon detector

The generated fluorescence enters the objective lens under various angles because they are scattered on their way back through the sample. Consequently, the fluorescence light cannot be focused onto a small focal spot which necessitates a single-photon detector with large detection surface. Moreover, the fluorescence signal from *in vivo* experiments is very low being in the single photon range when imaging single dendritic spines. Therefore, the photon detector should have a high internal gain to convert the single photons into a measurable

signal and a high quantum efficiency to detect as many photons as possible. A photomultiplier tube fulfills these criteria quite well by having a large sensitive area of 5 - 8 mm in diameter, a high gain of $> 10^6$ and a reasonable quantum efficiency that can reach 40% (Kapusta *et al.*, 2015). A PMT consists basically of a photocathode, an anode and dynodes housed in a vacuum tube. When a photon hits the detector surface it is converted into an electron by the external photoelectric effect. The electron enters the vacuum tube and is accelerated by the electric field towards the first dynode, where further electrons are released. At each of the successive dynodes, the multiplication process is repeated leading to a multiplication factor of 10^6 - 10^7 (Kapusta *et al.*, 2015). The electrons are finally collected by the anode and the PMT output signal is large enough to be directly measured without any further amplification.

Only recently, hybrid photodetectors (HPDs) were alternatively used for two-photon imaging (Cheng *et al.*, 2011), consisting of a silicon avalanche photodiode inside a vacuum tube (Fukasawa *et al.*, 2008; Kapusta *et al.*, 2015). Fluorescence photons are converted into electrons by the same photocathode material as used for PMTs, here gallium arsenide phosphide (GaAsP), and thus both detector types have the same detection efficiency. The resulting electrons are accelerated by a strong electric field of several kilovolts (for the HPD used here: -8 kV) towards the photodiode where their energy is converted into electron-hole pairs. These secondary electrons are further amplified by the gain of the avalanche photodiode, which depends on the applied bias voltage. Thus, the initial photon energy is amplified in two steps, instead of about 10 steps in case of 10 dynodes inside standard PMTs. At each amplification stage, charge fluctuations lead to loss and additional noise, so-called excess noise. For this reason, the final photon counting efficiency can be higher for the HPD compared to the PMT, even though the photocathode material and its surface area are the same for both. However, the total gain of a HPD is only in the range of 10^5 and needs to be amplified with a low-noise amplifier to generate a measurable signal (Fukasawa *et al.*, 2008; Kapusta *et al.*, 2015). Another major difference compared to PMTs is that HPDs do not show afterpulsing (Fukasawa *et al.*, 2008; Kapusta *et al.*, 2015). In a standard PMT additional electrons are created by ionization of residual gas molecules by the electrons passing through the photomultiplier tube. Some of these electrons arrive at the photoanode after the initially registered signal and prolong the output signal in time. In the HPD only a single electron travels from the photocathode towards the photodiode and the resulting signal is thus free of afterpulsing and much shorter in time. This advantage is especially useful for example for FLIM measurements (Becker *et al.*, 2011), or for multiplexed two-photon imaging (Cheng *et al.*, 2011). In case of deep two-photon calcium imaging, the fluorescence signals are extremely low and HPDs are of particular interest because of their lower excess noise.

1.2.3 Calcium imaging

For review about calcium signaling and calcium imaging please refer to (Grienberger & Konnerth, 2012).

The major application of two-photon laser scanning microscopy is real-time imaging of neuronal activity on a cellular and subcellular level. This is the only method so far which is capable of measuring dense cell populations functionally with single-cell resolution *in vivo*. Even subcellular compartments can be recorded functionally, such as dendrites and spines. To capture cellular and subcellular activity the cells are filled with fluorescent indicators that bind to specific ions. An increase in ion concentration corresponds to an increase or decrease in fluorescence (depending on the indicator) that can be visualized with a two-photon microscope. The most prominent ion to measure is calcium which acts as second messenger and enters the neurons from the extracellular space through ionotropic glutamate receptors, voltage-gated calcium channels or transient receptor potential type C channels (Grienberger & Konnerth, 2012). The reason to rather choose calcium as measurement parameter, instead of voltage or sodium, is the large concentration difference between intracellular calcium concentrations at rest and during electrical activation. The depolarization that underlies an action-potential opens voltage-gated calcium channels leading to an intracellular calcium concentration increase from 50 - 100 nM at rest to about 1000 nM (Berridge *et al.*, 2000; Grienberger & Konnerth, 2012). This change in calcium concentration can be clearly detected as a change in fluorescence with a fluorescent calcium indicator inside the cells, even under *in vivo* conditions. When measuring voltage with fluorescent indicators instead, the signal-to-noise ratios of the recordings underscore calcium recordings by at least an order of magnitude (Storace *et al.*, 2015; Sepehri Rad *et al.*, 2017). Even though the changes of the electrical field are large during action-potential firing, lying between 10^7 and 10^8 V/m, its spatial extent is in the range of ten angstroms and drops off exponentially with distance from the membrane (Peterka *et al.*, 2011). That means instead of filling the entire intracellular volume with a dye, the fluorescent molecules must sit within the cells' membrane. The number of fluorophores is thus limited by the cells' surface. Additionally, most of the cells' membrane lies within the cells, surrounding organelles. Fluorophores within these membranes do not contribute to the signal evoked by cellular activity and only contribute to background fluorescence (Peterka *et al.*, 2011). The overall signal-to-noise ratio of voltage-changes reported by fluorescent voltage indicators is hence quite low. Despite these disadvantages, ongoing improvements in the design of these indicators make them more and more applicable to single cell and subcellular imaging *in vivo* (Akemann *et al.*, 2013; Gong *et al.*, 2015; Yang *et al.*, 2016b). However, the poor fluorescence signals obtained in these experiments show that voltage indicators are still far from a broad application to functional *in vivo* recordings. Intuitively, sodium would be the

second choice for reporting neuronal activity, instead of voltage, because sodium is the major charge carrier for action-potentials as well as for excitatory postsynaptic currents. But the intracellular concentration changes during these processes are too low to be detected *in vivo* with fluorescence imaging. Only for *in vitro* experiments sodium indicators are successfully used (see for example (Rose *et al.*, 1999)). Instead, by measuring calcium concentration changes with fluorescent indicators, action-potentials can be clearly resolved in single cells *in vivo* and even subthreshold local calcium influx into single spines can be detected. For common synthetic calcium indicators, the fluorescence amplitude depends linearly on the underlying change of ion concentration. However, the calcium-binding and unbinding kinetics of calcium indicators are in the range of hundreds of milliseconds, which is slow compared to the millisecond range of action-potential firing. The precise time course of the underlying calcium concentration changes and high-frequency trains of action-potential can hardly be resolved. The benefit of the comparably slow kinetics is that the data acquisition speed does not need to be in the millisecond range and the reported neuronal signals can be recorded with video-rate scanners. In summary, the comparably large calcium concentration changes during cell activity are the major reason for the choice of calcium as a reporter for cellular and subcellular activity in *in vivo* experiments. The recorded fluorescence changes allow for the analysis of the time course, magnitude and location of neuronal activity *in vitro*, *in vivo* and even in awake behaving mice.

1.2.3.1 Fluorescent calcium indicators

The two main groups of fluorescent calcium indicators are protein-based genetically encoded calcium indicators (GECIs) and small-molecule chemical calcium indicators. Both of them are widely used for *in vivo* experiments and have their strengths and weaknesses. For example, GECIs can be used to stain specific cell types or subcellular compartments and they are suitable for chronic imaging experiments. On the other hand, synthetic calcium dyes can be applied in acute experiments making this approach highly versatile. Furthermore, synthetic dyes report linearly about calcium changes and show high sensitivity and fast kinetics. Thus, the choice of the best-suited calcium indicator depends on the individual experimental needs. (Grienberger & Konnerth, 2012)

In this thesis synthetic calcium indicators are used exclusively. These have to fulfill a number of specific properties to allow for high-quality recordings of neuronal activity *in vivo*. First of all, a good calcium dye has to exclusively bind to calcium and needs to have a calcium dissociation constant ($K_d(Ca^{2+})$) in the range of the calcium concentrations that are measured, i.e. roughly between 100 nM and 1000 nM. A dye with a high $K_d(Ca^{2+})$ value and thus a low calcium affinity adds only little calcium buffer capacity to the cells and reports calcium concentration changes with comparably rapid kinetics (Grienberger & Konnerth,

19

2012; Oheim *et al.*, 2014). However, the fluorescence of low calcium affinity dyes is low under baseline conditions and the identification of cells or subcellular structures might be difficult in a period without cellular activity. By comparison, cells filled with a high calcium affinity dye are bright even at rest and can be displayed easily. However, the fluorescence changes induced by cell activity are small. (Grienberger & Konnerth, 2012; Oheim *et al.*, 2014). Thus, the $K_d(Ca^{2+})$ value of a calcium dye should be in between these two extremes. An example for a widely used standard synthetic calcium indicator is Oregon Green BAPTA-1 (OGB-1) with a $K_d(Ca^{2+})$ value of 170 nM. Neurons filled with OGB-1 have a quite bright baseline fluorescence and calcium concentration changes are reported with comparably large fluorescence transients. Moreover, it reports linearly on changes in calcium concentrations, which is another requirement for a good calcium indicator (Oheim *et al.*, 2014). In addition, good calcium dyes should have a high molar extinction (ε) and a high fluorescence quantum yield (Φ_F), as well as a large dynamic range (F_{min}/F_{max}) to allow for fluorescence signals with high SNRs (Oheim *et al.*, 2014). Also, there should not be any bleaching of fluorescence, when illuminating the dye with pulsed laser light at laser power values required for *in vivo* recordings (Oheim *et al.*, 2014). Moreover, for the application to living cells the dye needs to be water-soluble and non-toxic. To easily stain dense cell populations with a synthetic calcium dye, it has to be available as membrane permeable acetoxymethyl (AM) ester, but for single-cell staining a membrane impermanent salt version is needed. (Grienberger & Konnerth, 2012; Oheim *et al.*, 2014). Considering all the properties listed above, it becomes clear that it is not trivial to synthesize a good calcium indicator, neither to identify the optimal one for a specific scientific purpose among those which are currently available.

1.2.3.2 Red-shifted calcium indicators

In the present study, red-shifted calcium indicators were used with single-photon excitation wavelengths longer than 550 nm. Table 1 gives an overview of commercially available red-shifted calcium dyes in comparison to the widely used green-emitting indicator OGB-1. These include Rhod-2, Calcium Orange, Calcium Crimson and Fura-Red. Fura-Red can be excluded from further considerations a priori because the excitation wavelength of Fura-Red is even shorter than that of OGB-1. The performance of Calcium Orange under *in vitro* conditions is poor because it does not stain the cells uniformly but compartmentalizes subcellularly and the fluorescence signals related to calcium concentration changes are of bad quality ((Thomas *et al.*, 2000) and own data). Furthermore, its loading efficiency is quite low, as well as for Calcium Crimson (Yuste *et al.*, 2011). Following the literature neither Calcium Orange nor Calcium Crimson were used for neuronal population calcium imaging *in vitro* or *in vivo* in the past 25 years indicating their inapplicability for this purpose.

Calcium indicator	λ_{ex} [nm]	λ_{em} [nm]	ε [M^{-1}cm^{-1}]	Φ_F	F_{min}/F_{max}	K_d (Ca^{2+}) [nM]
OGB-1	494	523	19000	0.7	~14	170
Rhod-2	552	581	82000	0.03	~3.4	570
CaOrange	549	576	80000		~3	185
CaCrimson	590	615	113000		~2.5	185
Fura Red	458	488	43000	0.013	~3.8	140

Table 1 *Commercially available red-shifted calcium dyes. The parameters were mainly collected from information provided by the distributor (Thermofisher & AAT Bioquest) and complemented by (Minta et al., 1989; Paredes et al., 2008; Oheim et al., 2014).*

Fortunately, two new red-shifted calcium indicators appeared on the market, Cal-590 and Cal-630, which were found online by my colleague Carsten Tischbirek. Only one year before, the green version of these dyes, Cal-520, was developed and its calcium reporting properties were characterized under *in vivo* conditions (Tada *et al.*, 2014). Cal-520 outperforms OGB-1 by reporting calcium concentration changes with larger signal amplitudes, higher SNR and faster kinetics (Tada *et al.*, 2014). These results raise hope for its red-shifted versions.

The information about Cal-590 and Cal-630 available online are listed in table 2 including the excitation and emission wavelengths of the dyes as well as the calcium affinities. The K_d(Ca^{2+}) value of Cal-520 is almost doubled compared to OGB-1, explaining its fast kinetics shown by (Tada *et al.*, 2014). The red-shifted versions of Cal-520 have even higher K_d(Ca^{2+}) values, indicating lower baseline fluorescence levels and even faster kinetics. The K_d(Ca^{2+}) value of Cal-590 is comparable to those of Rhod-2, Fluo-3 or Fluo-4, whereas Cal-630 exceeds this range with a K_d(Ca^{2+}) value of 792 nM. The calcium affinity of both dyes, Cal-590 and Cal-630, is within the acceptable range for detecting action-potential-evoked activity, corresponding to K_d(Ca^{2+}) values between 100 and 1000 nM. Thus, it is worth it to test both versions in *in vivo* experiments. Cal-590 as well as Cal-630 are available as salt and as AM version, allowing for labeling populations of cells but also single cells with electroporation or whole-cell patching.

Calcium indicator	Excitation wavelength [nm]	Emission wavelength [nm]	$K_d(Ca^{2+})$ [nM]
OGB-1	494	523	170
Cal-520	492	514	320
Cal-590	**558**	**584**	**561**
Cal-630	**607**	**623**	**792**

Table 2 Parameters of the fluorescent calcium dyes OGB-1, Cal-520, Cal-590 and Cal-630, provided by the distributor (Thermofisher and AAT Bioquest).

1.2.3.3 Cell labeling techniques

Small-molecule chemical calcium indicators can be loaded into single cells or into large cell populations with various techniques. The two techniques used in this thesis are multi-cell bolus loading with the AM ester version of a calcium dye and single-cell electroporation with the salt version. For review of other techniques please refer to (Grienberger & Konnerth, 2012).

For multi-cell bolus loading, the AM fluorescent calcium dye is injected with a pressure of maximum 700 mbar into the tissue via a glass pipette so that an area of about 300 µm in diameter is stained, as schematically shown in fig. 5 A (Stosiek *et al.*, 2003; Garaschuk *et al.*, 2006). Once inside the cell, the hydrophobic ester residue is removed by intracellular esterases (Tsien, 1981). One hour after dye injection most of the dye molecules are hydrolyzed and trapped inside the cells. Action-potential activity can then be recorded from a large population of neural cell bodies. The dendrites and axons are filled with the dye as well but cannot be resolved individually. They contribute to an average neuropil signal recorded from the tissue volume surrounding the cell bodies. To resolve dendrites and spines, single cells can be filled with a fluorescent marker, as indicated in fig. 5 B. This can be achieved by whole-cell patching a cell (Margrie *et al.*, 2002; Eilers & Konnerth, 2009), or via electroporation of a fluorescent calcium indicator, the method of choice in this thesis (Nevian & Helmchen, 2007; Kitamura *et al.*, 2008). Therefore, the salt version of the dye is filled into a glass pipette and visually guided through the brain tissue by the shadow-patching approach (Kitamura *et al.*, 2008). Once a single cell is chosen for electroporation, the pipette is positioned in close proximity of the cell and electrical pulses are applied to eject the charged dye molecules out of the pipette. At the same time, the current pulse disrupts the cell membrane and pores are created which promote the dye delivery into the cell. After a short recovery time and after diffusion of the dye into the dendrites, calcium changes can be detected in the soma, the dendrites and the spines. (Nevian & Helmchen, 2007; Kitamura *et al.*, 2008)
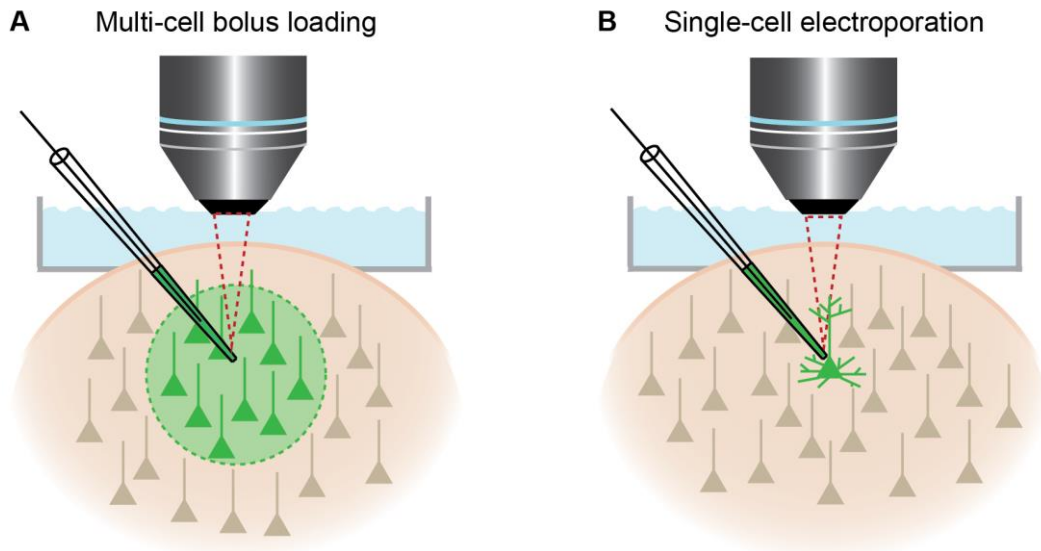
Fig. 5 *Dye-loading techniques. **(A)** Scheme of multi-cell bolus loading of an acetoxymethyl (AM) ester dye. A patch-pipette is filled with the calcium indicator and pressure-injected into the tissue. **(B)** Scheme of single-cell electroporation. A patch-pipette is filled with the salt version of the fluorescent calcium dye and guided through the tissue with the shadow-patching approach. The dye is delivered into the cell with few current pulses.*

1.2.4 Penetration depth limit

The long wavelength excitation light, used for two-photon imaging, can penetrate two to three times deeper into biological tissue compared to the blue or UV light for single-photon excitation. This is due to the longer attenuation lengths in biological tissue of light with longer wavelengths, within a wavelength range between 350 nm and 1300 nm (Kobat *et al.*, 2011). Nevertheless, the imaging depth is limited because the ballistic excitation light attenuates exponentially with traveling distance, mainly due to scattering effects caused by refractive index inhomogeneities in biological tissue (Helmchen & Denk, 2005). High-quality images with good contrast and good sensitivity to single-cell signals can only be acquired within several hundred microns inside the tissue with standard two-photon techniques. This corresponds to the upper three out of six cortical layers of the mouse brain. To understand the theoretical background of this limit and to explain the approaches to break this limit in this work, some background information will be provided about tissue-light interaction and fluorescence generation with a two-photon microscope.

In the wavelength range between 650 nm and 1300 nm, the dominating light-tissue interaction is scattering, which is strongly wavelength dependent. For objects much smaller than the wavelength the light scattering is nearly isotropic and scales as $\sim 1/\lambda^4$ (Rayleigh scattering). In contrast, objects with a size comparable to the wavelength scatter the incoming light mainly in forward direction and the wavelength dependence $\sim 1/\lambda^n$ with $n > 1$ depending on the particle size (Mie scattering) (Helmchen & Denk, 2005). In biological tissue, the size of the particles is diverse leading to a combination of both scattering phenomena. The strength of scattering can be described with the scattering length l_s which

23

is the average distance between two scattering events. The overall attenuation length of the excitation light in the tissue is defined by $l_e = (1/l_s + 1/l_a)^{-1}$, with l_a being the absorption length, which is negligible in the NIR range compared to l_s (Helmchen & Denk, 2005). For two-photon imaging brain tissue the number of ballistic photons decreases exponentially with depth and so does the two-photon excitation efficiency (Helmchen & Denk, 2005). To maintain the ballistic fraction of photons arriving at the focus, the laser power needs to be increased exponentially with distance from the surface accordingly (Helmchen & Denk, 2005). But there is obviously a limit because the risk of tissue damage increases with the amount of laser power applied. Additionally, strong excitation laser light does not only increase the fluorescence excitation efficiency in the focal spot but also outside the focal volume, leading to a decrease in the signal-to-noise ratio (Theer & Denk, 2006; Leray *et al.*, 2008; Chen *et al.*, 2012b). Moreover, the spatial resolution declines with imaging depth, because the laser focus is not confined to a small volume, but is enlarged by scattering and optical aberrations (Chaigneau *et al.*, 2011; Ji, 2017). The enlarged focal spot is also responsible for an increase in neuropil contamination, because the fluorescence signal is integrated over a larger volume, which might not be restricted to a single cell, but can also contain surrounding dendrites and axons. At some point in depth, the recorded fluorescence transients can be dominated by the neuropil signal (Ji, 2014; Wang *et al.*, 2015). In summary, light scattering, optical aberrations and fluorescence background limit the imaging depth of two-photon fluorescence microscopy. The underlying basic concepts of this limit were shortly described here. To identify critical parameters which determine the depth limit, the fluorescence generation of a two-photon microscope and the theoretical depth limit are considered mathematically in the following.

The average number of photon pairs n_a absorbed by a fluorophore at the center of the focus, during a single laser pulse, under the paraxial approximation is given by (Denk *et al.*, 1990; Denk, 2006):

$$n_a = \sigma_2 \langle P \rangle^2 \tau^{-1} f^{-2} g_2 \left(\frac{\pi (NA)^2}{2\pi \hbar c \lambda} \right)^2 \qquad (4)$$

With the following parameters:

σ_2 Two-photon cross-section

$\langle P \rangle$ Incident average laser power

f Pulse repetition rate

τ Temporal pulse width

NA Numerical aperture

c Speed of light in vacuum

λ Wavelength

$g^{(2)}$ Time zero 2nd order temporal coherence (0.59 for hyperbolic-secant-squared shaped pulse and 0.66 for Gaussian shaped pulses)

The laser power declines exponentially with travelling distance inside the tissue, following the Lambert-Beer law:

$$\langle P \rangle = \langle P_0 \rangle exp \left(-z/l_s^{(ex)} \right) \qquad (5)$$

P_0 power incident on the sample surface

$l_s^{(ex)}$ scattering length for excitation light in tissue

z imaging depth

The maximum imaging depth can be defined by the minimum number of fluorescence photons that need to be emitted to get a well detectable signal. That means a minimal number of photon pairs n_{min} needs to be absorbed by a fluorophore within one laser pulse. Therefore, a minimal laser power $\langle P_{min} \rangle$ is needed which correlates with imaging depth as $\langle P_{min} \rangle = \langle P \rangle \exp(-z_{max}/l_s^{(ex)})$. Inserting this relation into equation (4) gives us the following theoretical two-photon imaging depth limit:

$$z_{max} = l_s^{(ex)} ln \left[\sqrt{\frac{\sigma_2 g^{(2)}}{n_{min} \tau f}} \frac{\pi (NA)^2}{2\pi \hbar c \lambda} \langle P \rangle \right] \qquad (6)$$

The maximum imaging depth z_{max} thus depends linearly on the scattering length of the excitation light and logarithmically on the incident laser power, the laser duty cyle and the

25

two-photon cross-section as well as the numerical aperture. Although this equation gives the impression to be complete, many parameters influencing the imaging depth limit are still missing, such as optical aberrations, pixel dwell time, signal collection efficiency, background fluorescence, shot noise, dark noise, setup and sample specific properties such as size of the craniotomy, vascularization, etc. Hence, it makes more sense to generalize the equation to understand the basic relations without giving the impression of integrity (Oheim *et al.*, 2001):

$$z_{max} \sim l_s^{(ex)} \ln \left(\alpha P_0 \sqrt{\phi_{max}\left(\frac{1}{\tau f}\right)} \right) \tag{7}$$

Parameters related to setup properties such as detector noise and background fluorescence are combined to the parameter α and parameters influencing the detection efficiency are merged to the parameter ϕ_{max}. With this formula, we can now estimate which parameter is likely to have a great effect when tweaking it for deep imaging. The only variable which is directly proportional to the maximum imaging depth is the scattering length of the excitation light. For this reason, the first approach in this thesis to increase the imaging depth is the use of longer excitation wavelengths, compared to the standard wavelength range from about 800 - 950 nm. The second important parameter is α which depends logarithmically on the imaging depth. Thus, the second promising strategy for enhancing the two-photon imaging depth is the reduction of fluorescence background for an increased signal-to-noise ratio.

The combination of these two ideas, the use of long excitation wavelengths and the reduction of the fluorescence background, plus some hardware optimizations of the microscope, allowed for functional imaging of dense cell populations with single-cell resolution within all cortical layers in the mouse *in vivo*. This work was inspired by previous approaches to overcome the depth limit of two-photon microscopy. However, none of them was immediately applicable to reach the goal of *in vivo* calcium imaging of dense cell populations in deep cortical layers with single-cell resolution at high imaging speed. In the next section, these methods will be quickly reviewed, with short explanations of their strengths and weaknesses.

1.2.5 Approaches of deep two-photon imaging

The most straight-forward approach to reach deep brain structures with one- or two-photon excitation is to remove the tissue on top of the target region surgically and implant a gradient refractive index (GRIN) lens to the animal's skull. The light focusing characteristic of the lens is achieved by continuous changes in the density of the material resulting in a spatially varying refractive index that follows $n(r) = n_0(1 - g^2 r^2 /2)$, with r as radius from the lens axis, n_0 as refractive index on the axis and g as a constant parameter (Flusberg *et al.*, 2005). Usually, a doublet of these lenses is used, one of them acting as objective lens by focusing

the excitation light into the tissue and collecting the emission light and one as relay lens. In this configuration deep nuclei of the mouse brain such as the striatum, substantia nigra and lateral hypothalamus, were functionally imaged with micron-scale resolution (Bocarsly *et al.*, 2015). A similar approach is the implantation of a micro-prism that reflects the light by 90° providing optical access to a field-of-view perpendicular to the brain surface (Chia & Levene, 2009; Andermann *et al.*, 2013; Low *et al.*, 2014). These invasive approaches cannot be used here to image layer 5 neurons in the visual or barrel cortex, because the structures of interest would undergo severe damage. A GRIN lens with a diameter of 350 - 1000 μm implanted on top of the cell bodies in layer 5 destroys their dendrites and axons running vertically towards the brain surface. A prism with a side length of 1 mm implanted perpendicular to these cells disrupts connections to the surrounding cortical areas.

Less invasive methods for deep two-photon calcium imaging were developed in the past. For example, a regenerative amplifier was used to generate high peak-intensity laser pulses at low repetition rates (Theer *et al.*, 2003). Following equation (4) this led to an increase in the two-photon excitation efficiency and according to equation (7) increase the maximum imaging depth. This idea was applied successfully to *in vivo* calcium imaging of cortical layer 5 neurons of the mouse (Mittmann *et al.*, 2011). Unfortunately, this approach requires a reduction of imaging speed because the low laser pulse repetition rate needs to be synchronized with the image acquisition to provide at least one laser pulse per pixel. Here we use high-speed resonance scanners or AODs to be able to record high-speed calcium transients which in addition allows for single spines with low photodamage (Chen *et al.*, 2011; Chen *et al.*, 2012a; Jia *et al.*, 2014). To give up this speed advantage would be very painful, especially for imaging single-cell activity in layer 5 of the cortex. These cells have a quite high spontaneous average firing rate of more than 1.5 Hz (Niell & Stryker, 2008) and even higher evoked ones of up to 20 Hz (Sakata & Harris, 2009). Following the Nyquist-Shannon sampling theorem, a frame rate of 40 Hz would be required at least to resolve these signals (assuming the use of a calcium indicator with fast kinetics). At a comparable small field of view of 64 x 64 pixels Mittmann et al., 2011 imaged layer 5 neurons in the mouse *in vivo* at a frame rate of 15.6 Hz. Here, the aim is to image these neurons with frame rates between 40 and 500 Hz.

Another way of increasing the two-photon efficiency in the focal spot is the use of adaptive optics, to correct for sample induced aberrations. Functional imaging of the cortical layer 5 was achieved with this technique (Wang *et al.*, 2014; Wang *et al.*, 2015) and even calcium transients of axonal boutons in layer 4 could be recorded due to the improved spatial resolution and the increased signal-to-noise ratio (Sun *et al.*, 2016). This elegant approach

requires however quite complex implementation for a comparably small improvement in depth penetration.

The idea to increase the maximum penetration depth applied in the present work, is the use of long two-photon excitation wavelengths, beyond the standard wavelengths of 800 to 950 µm. Up to 1300 nm, the major light-tissue interaction is scattering, which decreases towards longer wavelengths und thus the longer the wavelengths the higher the depth penetration (Balu *et al.*, 2009; Kobat *et al.*, 2009; Shi *et al.*, 2016). Standard two-photon excitation lasers are Ti:Sa lasers, emitting wavelengths only up to maximum 1100 nm and with very low output power towards the long wavelengths range. Longer wavelengths can be achieved with an optical parametric oscillator (OPO), consisting of a birefringent crystal that is pumped with a frequency ω_3 and generates two frequencies ω_1 (named signal) and ω_2 (named idler), with $\omega_1 + \omega_2 = \omega_3$ These frequencies resonate in a cavity around the crystal to increase the conversion efficiency. By use of an OPO Kobat et al. used an excitation wavelength of 1280 nm and extended the maximum imaging depth inside the mouse cortex in vivo to 1.6 mm (Kobat *et al.*, 2011). However, the imaged structures are vasculature, stained with a bright fluorescent Alexa dye. In contrast, the goal of this work is functional imaging of neuronal activities in deep cortical layers, but calcium indicators are usually not as bright as Alexa dyes and the standard indicators are excited with excitation wavelengths between 800 nm and 950 nm. Red-shifted indicators are rarer and do usually not perform as good as the green-emitting ones (Oheim *et al.*, 2014).

One way to still use standard calcium indicators but to extend the excitation wavelength to the further red regime is three-photon excitation of the fluorophores. The excitation wavelength is then roughly tripled compared to single-photon excitation. Moreover, the probability of three-photon excitation depends on the cube of the laser light intensity which leads to a highly localized excitation spot and even better optical sectioning compared to two-photon microscopy. The out-of-focus fluorescence is also strongly reduced because the three-photon fluorescence decreases as $\sim 1/d^4$ with the distance from the focus 'd' compared to $\sim 1/d^2$ for two-photon excitation (Horton *et al.*, 2013b). Recently, three-photon calcium imaging was successfully applied to functional *in vivo* imaging, extending the imaging depth to 1 mm (Ouzounov *et al.*, 2017). However, three-photon imaging is not trivial, because of low cross-sections for three-photon absorption of the fluorophores. To induce measurable fluorescence with three-photon microscopy, laser sources with low repetition rates and high peak intensities can be necessary, as used in (Horton *et al.*, 2013b) and (Ouzounov *et al.*, 2017). Moreover, if the three-photon excitation wavelengths extend 1300 nm, water absorption peaks can lead to a temperature increase of the tissue. To reduce this effect,

heavy water (D_2O) was used as immersion liquid which is highly impractical because D_2O is hygroscopic and has to be sealed from the air (Horton *et al.*, 2013b).

1.3 The mouse whisker system

The human cortex seems to be the part of the brain, giving us unique cognitive abilities, compared to other mammalian species. Nevertheless, there are many common properties between the cortices of human, monkey, cat, rat and mouse. The laminar organization of the cells, the arrangement into specified areas and even cellular classes can be widely generalized (Douglas & Martin, 2004; Thomson & Lamy, 2007; Harris & Shepherd, 2015). Because of this generalizability, the underlying computational strategies seem to be very similar between species and are core object of study for many brain researchers. The neocortex is characterized by a horizontal cellular organization of at least six cellular laminae (Brodmann, 1909) and by vertical cell formations belonging to so-called columns. Cells clustered in a cortical column show similar function (Hubel & Wiesel, 1959, 1968, 1969; Mountcastle, 1997). For example, in the visual cortex, neurons within a cortical column hold the same orientation preference to visual stimuli (Hubel and Wiesel 1959, Hubel and Wiesel 1968, Hubel and Wiesel 1969). To study cortical columns on a single-cell level *in vivo*, the mouse is a widely used model system, because of its small brain size and thus its accessibility and the ease of genetic manipulations. However, functional columns, clustering neurons with similar orientation preference, are absent in the mouse visual cortex (Andermann *et al.*, 2013). Therefore, the most popular target region to study the anatomy-function relationship of cortical columns in the mouse is the vibrissal area of the somatosensory cortex. Here, cytoarchitectonic equivalents to cortical columnar structures can be found (for review see (Petersen, 2007)). Sensory inputs from distinct facial whiskers (or vibrissae) project to barrel fields in layer 4 of the mouse barrel cortex, forming a structural and functional elementary module. Whenever the mouse touches an object with one or more whiskers, the cells in the cortex which are activated first, are located in layer 4 of the corresponding barrel field of the primary somatosensory cortex. To better understand the functional roles of the vibrissal system of the mouse, we need to understand how a mouse perceives its world. The mouse is a nocturnal animal which lives in dark holes where it gets hardly any visual information. Instead of seeing its environment, the mouse is rather hearing and feeling it. The mouse explores its direct environment with rhythmic back and forth movements of its facial whiskers with a frequency of around 15 Hz (Sofroniew *et al.*, 2014; Hires *et al.*, 2015). This whisking behavior serves to map the environment, recognize and locate objects and discriminate fine-scale textures. Therefore, the mouse is extremely sensitive to whisker touch, which can be simulated in experiments on anesthetized or awake behaving mice (for example (Varga *et al.*, 2011; Sachidhanandam *et al.*, 2013)).

In summary, the mouse barrel cortex is well-structured, easily accessible from the top of the mouse brain and can be activated by defined and well-reproducible sensory stimulation of individual whiskers. Therefore, the mouse vibrissal somatosensory system became one of the most popular model systems to study cortical processing of sensory inputs from the periphery on a cell population as well as on a single-cell level *in vivo* (for review see (Petersen, 2007; Feldmeyer, 2012; Feldmeyer *et al.*, 2013)). One of the main goals of these studies is to understand the link between anatomical structures, synaptic connections, molecular mechanisms and behavior, but much is still unknown, especially regarding the deep and hardly accessible cortical layers. To contribute to this exciting field of research, the aim here is to investigate responses of layer 5 neurons in the mouse barrel cortex to defined sensory signals and to analyze the morphology of cells with specific response patterns.

1.3.1   Anatomy and signaling pathways of the barrel cortex

In the following, a short description of the anatomy of the mouse vibrissal somatosensory system and the pathway of the sensory signals from the periphery to the cortex is provided. For more detailed information, please refer to, for example (Petersen, 2007; Fox, 2009; Feldmeyer, 2012; Feldmeyer *et al.*, 2013; Meyer *et al.*, 2013). The whiskers are located on both sides of the mouse snout and arranged in rows and arcs. The mouse has 30 - 40 macrovibrissae and 70 - 100 microvibrissae on each facial side, with the macrovibrissae being long and strictly organized, while the microvibrisae are shorter, more densely packed and not particularly ordered (Brecht *et al.*, 1997). The macrovibrissae can be mapped as seen in fig. 6 A, enabling a reproducible stimulation of specific whiskers across mice. When one of the whiskers is deflected, mechanoreceptors in the follicle, at the base of each whisker, are activated and depolarize sensory neurons (Ebara *et al.*, 2002). Those form glutamatergic synapses with neurons in the brain stem, which themselves project to the thalamus and thalamic neurons relay the signals to the cortex (fig. 6 C). This circuit can be categorized into three pathways: the lemniscal, the extralemnsical and the paralemniscal pathway. The lemniscal pathway forms the main signal flow from the periphery to the cortex. Here, sensory signals enter the principal trigeminal nucleus of the brainstem, which is arranged in barrelettes and each barrelette receives inputs from one specific whisker (Veinante & Deschenes, 1999). Neurons in these barrelettes project to the dorsal medial region of ventral posterior medial (VPM) nucleus of the thalamus, which is again clustered into so-called 'barreloids'. From here the sensory signals are transferred to layer 4 of the vibrissal area of the primary somatosensory cortex. This cortical area is also called barrel cortex, because of its barrel structure found in the cortical layer 4, similar to the structures seen in the brain stem and thalamus. The barrel arrangement of layer 4 in the barrel cortex resembles the arrangement of the whiskers at the snout of the mouse, as shown in fig. 6 A and B (Woolsey & Van der Loos, 1970; Petersen & Sakmann, 2000). Besides the projections

to layer 4, the VPM also innervates much weaker the upper part of layer 6. Within the paralemniscal pathway, sensory whisker signals are transmitted to the rostral section of the interpolar spinal trigeminal nucleus of the brain stem, which lacks a barrelette organization. Neurons in this part of the brain stem respond to the deflection of multiple whiskers, whereas neurons in the principal trigeminal nucleus mainly respond to single whisker deflection. Neurons in the interpolar spinal trigeminal nucleus innervate the posterior medial (POm) nucleus of the thalamus. Here, neurons have a broader receptive field compared to neurons VPM and are modulated by brain state (Lavallee *et al.*, 2005; Trageser *et al.*, 2006). Neurons in the POm innervate mainly layer 1 and the upper part of layer 5, layer 5A, of the barrel cortex, the secondary somatosensory cortex and the motor cortex. A more recently discovered pathway is the extralemniscal pathway consisting of the caudal part of the trigeminal spinal interpolaris nucleus, which is organized into barrelettes (Pierret *et al.*, 2000). Neurons from this nucleus innervate the ventral-lateral region of the VPM, which does not show a barreloid-organization. From here, strong projections are found to the secondary somatosensory cortex and very weak ones to layers 3, 4 and six of the barrel cortex. In this case the projections to the barrel cortex do not innervate the barrel fields, as for the lemniscal pathway, but the regions in between the barrels, which are called 'septa' (Pierret *et al.*, 2000).

It was suggested that the extralemniscal pathway is mostly responsible for encoding touch signals, whereas the paralemniscal pathways transmits motion information and the lemniscal pathway is a combination of the two (Yu *et al.*, 2006). However, to draw final conclusions about the specific functional role of these pathways, a detailed analysis of the functions of their cellular components would be necessary and is still part of ongoing research. Furthermore, the pathways do not act independently of each other and are heavily interconnected by feedforward and feedback signaling pathways. In addition, the barrel cortex does not only receive thalamic inputs but is also intracortically well connected with, for example, the primary motor cortex, the secondary somatosensory cortex and the contralateral barrel cortex (fig. 6 D). The major connections between cells from different cortical layers within the barrel cortex are summarized in the next section.
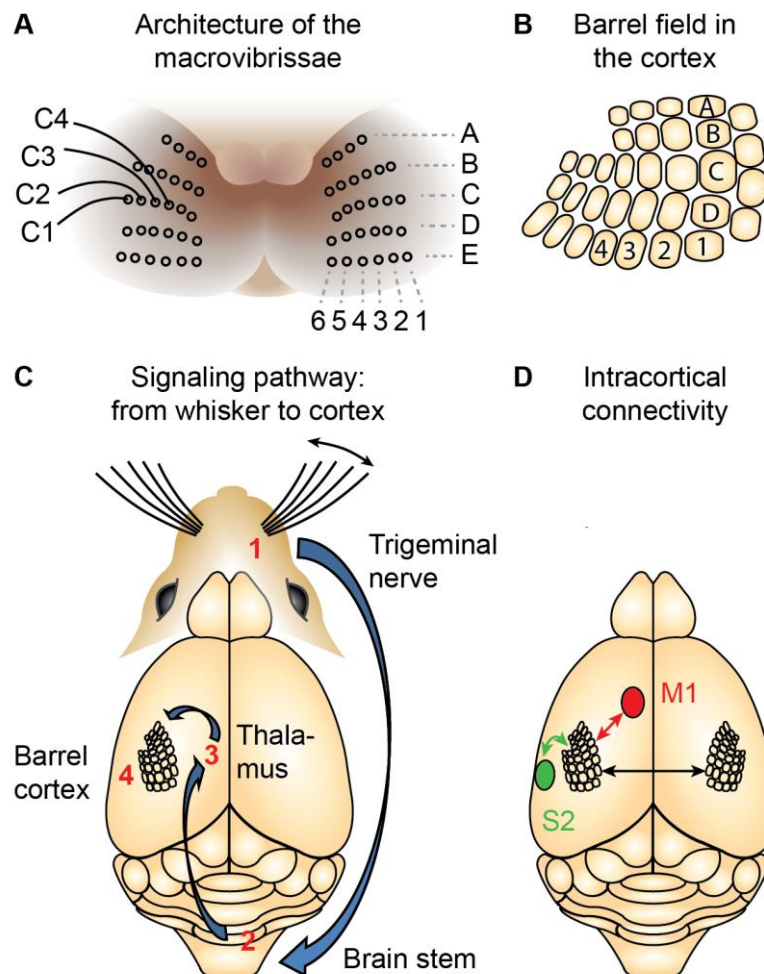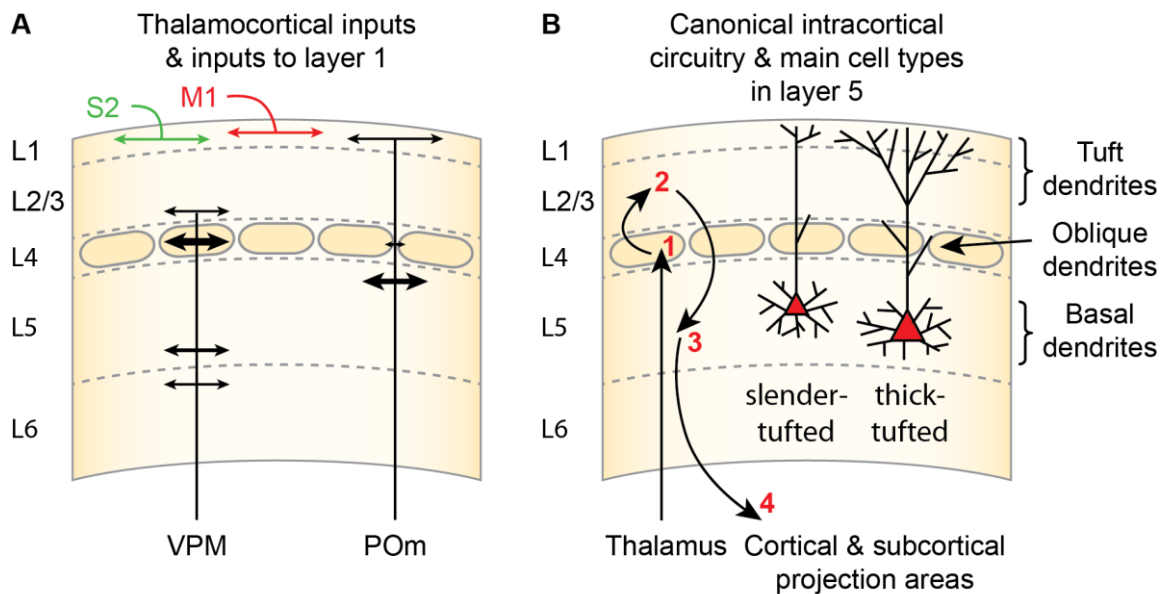
Fig. 6 *The rodent whisker system: Anatomical structure and synaptic pathways* **(A)** *Arrangement of the macrovibrissae at the mouse snout.* **(B)** *Barrel field structure in layer 4 of the barrel cortex of the mouse. Each barrel receives inputs from one specific whisker, indicated with numbers and letters.* **(C)** *Synaptic pathway of sensory information about whisker-touch. Whisker deflections activate sensory neurons in the trigeminal nerve (1) which form glutamatergic contacts with the brain stem (2). Signals from the brain stem project to the thalamus (3), which relays information to layer 4 of the barrel cortex (4).* **(D)** *Main intracortical reciprocal connections of the mouse barrel cortex. M1 is the primary motor cortex and S2 is the secondary somatosensory cortex.*

1.3.2 Intracortical connectivity and excitatory cell classes

The 'canonical microcircuit' in the neocortex can be described as following (fig. 7 B): Afferent fibers from the thalamus activate cells in the cortical layer 4, which project to supragranular layers 2 and 3. Layer 2/3 cells innervate cortical layers 5 and 6, the main output layers of the cortex (Gilbert & Wiesel, 1979; Callaway, 2004; Douglas & Martin, 2004). Layer 5 projects to other cortical areas, contralateral cortex, thalamus, superior colliculus, pons and spinal cord whereas layer 6 neurons project back to the thalamus, serving as a feedback signal for sensory inputs (for review see for example (Feldmeyer, 2012)). This simplified view describes the main signal flow of sensory inputs. However, it does not reflect a complete picture of intracortical signal processing: the cortex receives inputs from many different brain regions and onto different cell layers, not only into layer 4. Layer 1, for example, is a major projection area for feedback signals from higher cortical areas (fig. 7 A) (Gilbert & Sigman,

2007; Manita *et al.*, 2015). Thalamic input from the VMP does not only innervate layer 4, but innervates the cortex at multiple cortical depths (Wimmer *et al.*, 2010) and POm input to the cortex, which mainly targets the upper layer 5 and 1 (Wimmer *et al.*, 2010), is excluded from the simplified description of the canonical microcircuit of the cortex. A schematic overview of the major thalamic and cortical inputs to the barrel cortex is illustrated in fig. 7 A. Moreover, cortical cells do usually not only have one target region but span their axons across cortical layers or outside the barrel cortex. Layer 2/3 pyramidal neurons, for example, have an axonal arbor spanning across the entire barrel field, plus axonal branches outreaching other cortical areas, such as primary motor cortex (Feldmeyer *et al.*, 2006; Larsen & Callaway, 2006; Bruno *et al.*, 2009). In addition to the excitatory pathways, there are also numerous classes of inhibitory interneurons, suppressing the activity of their target neurons and thereby modulating the activity of the excitatory neurons heavily. It is thus not surprising that the full cortical circuitry is still only partially understood. One of the main goals for a deeper insight into cortical functions is to create anatomy-function maps and thus to reveal its functional micro-architecture. Therefore, researchers try to link recordings of single-cell activity *in vivo* evoked by sensory stimulation with the underlying morphology and connectivity (for example (Velez-Fort *et al.*, 2014; Kim *et al.*, 2015; Wertz *et al.*, 2015)). To group cells by their morphology, their axonal target regions can serve as primary criterion. Excitatory pyramidal neurons in the cortex, making up 70% - 80% of the cortical neurons (Markram *et al.*, 2004), can thereby be categorized into three large groups. Those are intratelencephalic neurons, pyramidal tract neurons and corticothalamic neurons (Harris & Shepherd, 2015). Intratelencephalic neurons project to the neocortex, the striatum, amygdala and claustrum, among others, and they are distributed in the layers 2 - 6. Moreover, they connect the two hemispheres via axons passing through the corpus callosum. Pyramidal tract neurons are found in the lower part of layer 5, called layer 5B, and project subcerebrally, including the brainstem, spinal cord and midbrain, but their axons also innervate the cortex, striatum and thalamus on the ipsilateral side. Third of all, layer 6 excitatory neurons are corticothalamic neurons, projecting to the ipsilateral thalamus, as mentioned above. For a more detailed description of neocortical circuitry, please refer to reviews, like for example (Thomson & Lamy, 2007; Harris & Shepherd, 2015). The next section focuses on the role of cortical layer 5 cells because the goal of this thesis is to elucidate sensory processing of layer 5 cells in the cortex.

A Thalamocortical inputs & inputs to layer 1

S2
M1

L1
L2/3
L4
L5
L6

VPM   POm

B Canonical intracortical circuitry & main cell types in layer 5

L1
L2/3
L4
L5
L6

Tuft dendrites
Oblique dendrites
Basal dendrites

slender-tufted   thick-tufted

Thalamus   Cortical & subcortical projection areas

Fig. 7 Thalamocortical and intracortical synpatic pathways of the mouse barrel cortex and main cell types in layer 5 (A) Thalamocortical inputs to the barrel cortex and intracortical inputs to layer 1 of the barrel cortex. VPM corresponds to the ventral posterior medial nucleus of the thalamus, POm to the posterior medial nucleus of the thalamus, M1 is the primary motor cortex and S2 is the secondary somatosensory cortex. (B) Left side: canonical intracortical pathway in the barrel cortex. Inputs from the thalamus arrive in layer 4 of the cortex (1), which projects to layer 2/3 (2). Cells in layer 2/3 send fibers to layer 5 (3), which is the main output layer of the cortex (4). Right side: Two main cell types in layer 5 of the mouse barrel cortex. The left one of the two cells represents a slender-tufted layer 5 pyramidal neuron with comparably small dendritic tuft and the cell at the right side is a thick-tufted pyramidal neuron with extensive dendritic branching in layer 1 and 2/3.

1.3.3   Cortical layer 5

Pyramidal neurons in layer 5 of the cortex are of special interest, because they are responsible for the major output signals from the cortex and ,moreover, their dendrites span across almost all cortical layers (for review see, for example, (Thomson & Lamy, 2007)). Based on this unique morphology, layer 5 pyramidal neurons are likely to have unique electrophysiological properties to integrate diverse inputs from different brain areas, which are discussed in part in section 1.4. For these reasons, layer 5 pyramidal neurons were often object of *in vitro* studies (for example (Larkum *et al.*, 2009)). However, to study these cells *in vivo* is quite challenging because they are located deep inside the cortex and cannot be accessed with standard two-photon imaging approaches. The aim of the work presented here is to overcome the depth limit of two-photon calcium imaging to study cellular and subcellular activity of layer 5 neurons in the mouse cortex *in vivo*. Therefore, some background information about layer 5 pyramidal neurons is provided in the following.

1.3.3.1   Single-cell morphology of layer 5 neurons

Pyramidal neurons in layer 5 of the cortex are characterized by a large dendritic tree extending through 5 of 6 cell layers. They show numerous basal dendrites, emerging from the soma and staying within layer 5, a single apical dendrite, crossing all cortical layers up to layers 1 and 2, where it ramifies into a dendritic tree, consisting of so-called tuft dendrites (fig. 7 B). Based on the tuft morphology, these neurons can be classified into at least two

categories: Slender-tufted pyramidal neurons with a thin apical dendrite and modest ramification in layer 1 and thick-tufted pyramidal neurons with a thick apical dendrite and extensive dendritic branching in layer 1 (fig. 7 B). Also, their intrinsic action-potential firing pattern differs: Slender-tufted neurons are regular spiking, whereas most of the thick-tufted neurons are intrinsically bursting (Chagnac-Amitai et al., 1990; Hattox & Nelson, 2007; Groh et al., 2010). A study, using retrograde tracers and single-cell reconstructions, found that in the mouse barrel cortex around 39% of the neurons in layer 5 of the mouse barrel cortex are slender-tufted and 15% are thick-tufted (Hattox & Nelson, 2007). They also showed that thick-tufted neurons in the mouse barrel cortex project to the thalamus, brain stem and spinal cord. Few of them project to the striatum. Slender-tufted cells, in contrast, project to the neocortex and the striatum. Groh et al. used genetic markers to characterize the morphology and intrinsic electrophysiological properties of slender- and thick-tufted neurons of the mouse cortex (Groh et al., 2010). With Etv1 BAC-EGFP transgenic mice 41% of all slender-tufted neurons in layer 5 were labeled (16% of all layer 5 neurons) (Groh et al., 2010). Glt25d2 bacterial artificial chromosome (BAC)-EGFP transgenic mice were used to label thick-tufted neurons, resulting in a labeling of 60% of the thick-tufted layer 5 neurons (9% of all layer 5 neurons) (Groh et al., 2010). They quantified the dendritic morphology (among other parameters) of these two cell classes, with results in agreement with Hattox et al., 2007. The most striking difference between the two cell types is the total apical tuft length, with 944 μm ± 366 μm for slender-tufted cells and 2323 μm ± 757 μm for thick-tufted cells. The branching of the tuft dendrites was quantified by the number of nodes of the apical dendrites, defined as bifurcation or trifurcation points of the apical dendrite, excluding oblique dendrites. Slender-tufted neurons have 12 ± 7 nodes in the apical dendrite, whereas thick-tufted ones have 19 ± 6. Also, the area covered parallel to the brain surface by the tuft dendrites is larger for thick-tufted, than for slender-tufted cell (Hattox et al., 2007). The tuft width of slender-tufted neurons is 157 μm ± 54 μm and for thick-tufted ones it is 356 μm ± 84. The density of thick-tufted neurons is highest in the lower part of layer 5, whereas the slender-tufted cells are located a slightly more superficial (Groh et al., 2010). However, there is no strict borderline and both subgroups of cells are mostly overlapping (Guan et al., 2015). Slender-tufted neurons can be found throughout layer 5 (Hattox & Nelson, 2007; Guan et al., 2015). It is therefore sometimes confusing to strictly separate layer 5 into two sublayers, layer 5A and 5B.

1.3.3.2 Connectivity of the cortical layer 5

The major difference between these two sublayers, layer 5A and 5B in barrel cortex, is not the distribution of slender- and thick-tufted neurons, but the axonal input pattern from the thalamus: POm projects heavily to layer 5A (and layer 1), but layer 5B is spared (fig. 7 A). By displaying the projection density of the POm to the barrel cortex, a clear border between

layer 4, layer 5A and layer 5B appears. Conversely, the VPM mainly innervates layer 4 of the barrel cortex but also sends afferents to layer 5B and 6A (fig. 7 A). These thalamic inputs to deep layers of the cortex were thought to be only modulatory (Callaway, 2004; Viaene *et al.*, 2011) and the major signals flow follows the cortical 'canonical microcircuit' described above (fig. 7 B). However, by measuring signal latencies of sensory inputs to deep cortical neurons *in vivo* with whole-cell patching single cells, it was shown previously that also deep cortical layers can be activated directly by the thalamus (Constantinople & Bruno, 2013). Monosynaptic thalamocortical connections were found mostly onto thick-tufted layer 5 neurons, but also onto slender-tufted layer 5 neurons, layer 6 neurons and smooth interneurons.

Coming back to intracortical inputs, it should be noted that not only layer 2/3 cells provide inputs to layer 5 pyramidal neurons, but also layers 4 and 5 and much weaker layer 6 (Lefort *et al.*, 2009). One cortical layer was not mentioned so far, which is layer 1. It consists of only few somata of interneurons expressing the ionotropic serotonin receptor 5HT3a (Rudy *et al.*, 2011). However, layer 1 is densely innervated by axons and dendrites and is the major input side for top-down inputs from higher cortical areas, carrying information about attention, expectation and perceptual motion commands (Gilbert & Sigman, 2007; Manita *et al.*, 2015). This is extremely interesting, keeping in mind the dendritic morphology of pyramidal layer 5 neurons, with extensive dendritic branching in layer 5 (basal dendrites) and in layer 1 (tuft dendrites). In principle, this morphology allows the cells to integrate information from two different input sides in layer 1 and 5. In the mouse barrel cortex there are three major sources of information input onto layer 1: The thalamic POm, the primary motor cortex and the secondary somatosensory cortex (fig. 7 A) (Cauller *et al.*, 1998; Petreanu *et al.*, 2009; Aronoff *et al.*, 2010; Bosman *et al.*, 2011; Sreenivasan *et al.*, 2016; Yang *et al.*, 2016a; Khateb *et al.*, 2017). Which kind of input each cell type in layer 5 receives is unknown. Moreover, the subcellular mechanisms of signal integration from the two input sides are not entirely clear. If signal inputs at the tuft are only passively transmitted along the apical dendrite, its impact on the soma vanishes due to signal attenuation along the long distance. When looking for alternative mechanisms, many *in vitro* studies found that tuft dendrites of pyramidal layer 5 neurons are capable to generate regenerative electric events and thus depolarize the soma. Whether any of the suggested active events occurs under physiological conditions *in vivo* is one of the major questions in ongoing dendrite research.

1.4 Synaptic integration in passive and active dendrites

(Here, only a short overview of dendritic integration and dendritic spikes is provided. For more information, please refer to the following review papers: (Magee, 2000; London & Hausser, 2005; Holthoff *et al.*, 2006; Major *et al.*, 2013). For more recent work see (Stuart & Spruston, 2015).)

Layer 5 pyramidal neurons receive a myriad of excitatory and inhibitory postsynaptic inputs simultaneously with their huge dendritic tree, spanning almost the whole cortex vertically. But how are these inputs transformed into a single change in membrane potential at the cell body? Researchers were working on this question for already sixty years, and the research is still ongoing. Key factors for the impact of excitatory postsynaptic potentials (EPSPs) on the membrane potential are their amplitude, their precise timing and their spatial distribution. Looking at pyramidal layer 5 neurons, it becomes clear that an input at a distal tuft dendrite will reach the soma differently than an input signal at a proximal basal dendrite. In the beginning of dendritic research, dendrites were considered as passive cables, first described by Wilfrid Rall (Rall, 1967; Rall *et al.*, 1967; Rall & Rinzel, 1973). He predicted a strong dependence between the location of synaptic input and its influence on the soma. Following his description, the axial resistance of the dendrites will lead to a voltage drop between the input side and cell body. Thus, the driving force for the current flow decreases with distance from the soma. Additionally, the capacity of the dendritic membrane slows down the kinetics of signal measured at the soma. Together, distal inputs onto a large dendritic tree with a large surface area will undergo strong loss along its way towards the soma. Plus, the more distal the input side, the higher the loss. In case of pyramidal layer 5 neurons, EPSPs at the distal tuft would thus not change the membrane potential much if any. Another interesting consequence of the filtering property of dendrites is the temporal smearing of distal input signals towards the soma leading to a prolongation of the time window, within which inputs can be summed up. Hence, there is more time for distal inputs to influence each other, than for inputs close to the soma, which have to be closer in time to result in a single change of membrane potential.

1.4.1 Dendritic spikes *in vitro*

Only when the patch-clamp technique was developed (Sakmann & Neher, 1984) and patching of dendrites became feasible, these theoretical predictions about dendritic integration could be tested experimentally. Therefore, dendritic and somatic whole-cell patches were performed simultaneously. Additionally, new imaging techniques allowed for recordings of changes in sodium and calcium concentrations in fine dendritic structures at high spatial resolution, which could be combined with patching the soma. In 2000, Williams and Stuart (Williams & Stuart, 2000) showed, for example, that the time course of somatic

membrane potentials induced by distal EPSPs did not follow the time course predicted by Wilfrid Rall (for review see (Magee, 2000)). Active conductances are responsible for this discrepancy and the first well-described active transmission along dendrites were back-propagating action-potentials (Stuart & Sakmann, 1994; Spruston *et al.*, 1995). Voltage-gated sodium channels lead to an active propagation of action-potentials, elicited at the axonal hillock, into the dendrites of the cells. Later on, the discovery of all-or-none action-potential-like signals in dendrites changed the general view about dendritic integration completely. Three different types of dendritic spikes were discovered, which are characterized by their underlying main conductance (for review see for example (Stuart & Spruston, 2015)). Fast dendritic spikes with a temporal width smaller than 5 ms are so-called sodium spikes, caused by regenerative activation of voltage-gated sodium channels (Turner *et al.*, 1991; Golding & Spruston, 1998; Helmchen *et al.*, 1999; Larkum & Zhu, 2002). These are usually initiated in small-diameter dendrites and fail to propagate into larger dendrites with higher input-impedance. Long-lasting or complex dendritic spikes are either calcium spikes, mediated by voltage-dependent calcium channels (Schiller *et al.*, 1997; Golding *et al.*, 1999) or NMDA spikes, mediated primarily by N-methyl-D-aspartate receptor (NMDA-R) channels. As calcium spikes are of larger amplitude and broader in time than sodium spikes, they can propagate more easily towards the soma and are able to initiate high-frequency burst firing of the cell (Helmchen *et al.*, 1999; Larkum *et al.*, 1999b; de Kock & Sakmann, 2008). NMDA spikes require depolarization for the relief from the magnesium block plus the release of glutamate. They are thus restricted in space to the site of glutamate release during their generation. They can still affect the action-potential firing of the cell, as shown for example by Palmer et al., 2014 *in vivo* (Palmer *et al.*, 2014).

1.4.2   Dendritic spikes *in vivo*

To explore whether dendritic spikes occur under physiological conditions and whether they are important for brain function, *in vivo* experiments were required. Two-photon imaging of cells filled with a fluorescent calcium indicator allows for recording single-cell and subcellular activity with good temporal resolution *in vivo*. Activation of single or multiple dendrites can thus be displayed in real-time. In state-of-the-art experiments, these imaging experiments are combined with whole-cell patching the cell, to acquire a simultaneous read-out of dendritic and somatic cell activity. With these techniques, dendritic spikes were indeed experimentally verified in anesthetized and awake animals and seem to play an important role in amplification and integration of synaptic inputs during sensory processing (Lavzin *et al.*, 2012; Xu *et al.*, 2012; Smith *et al.*, 2013; Grienberger *et al.*, 2014; Palmer *et al.*, 2014). NMDA spikes, for example, recorded from tuft dendrites of layer 2/3 pyramidal neurons in the mouse somatosensory cortex, preferentially during short electric shocks or airpuffs to the contralateral hindpaw (Palmer *et al.*, 2014). In the primary visual cortex of the mouse, NMDA

spikes occurred primarily when the preferred orientation of the visual stimuli was presented. Blocking these dendritic spikes decreased the selectivity of subthreshold responses of the soma, indicating that dendritic spikes could contribute to the tuning of the cell (Smith *et al.*, 2013). Also in the barrel cortex, NMDA spikes were verified *in vivo* in layer 4 pyramidal cells and seem to be important for the tuning of the responses to whisker deflection to various directions (Lavzin *et al.*, 2012).

1.4.3 Dendritic spikes in layer 5 pyramidal neurons

In vitro studies on brain slices of mice or rats demonstrated that pyramidal layer 5 cells are capable to fire small sodium and NMDA spikes in basal dendrites, NMDA spikes in fine tuft dendrites and calcium spikes, initiated at the main bifurcation of the apical dendrite (Larkum *et al.*, 1999b; Larkum & Zhu, 2002; Larkum *et al.*, 2009). The computational role of these dendritic spikes could be manifold (Stuart & Spruston, 2015). They can act as AND operators by setting a threshold on the number of inputs required for dendritic spiking. If this amount of inputs can be made of different groups of inputs, the cell acts like an OR operator. It was also suggested that inputs to proximal dendrites could enhance the propagation of dendritic spikes elicited at distal sites towards the cell body and subsequently increase action-potential firing (Larkum *et al.*, 2001). Interestingly, these cells can also act as coincidence detectors. When the cell is firing action-potentials, while distal synaptic inputs activate tuft dendrites, dendritic calcium spikes are facilitated and lead to burst firing of the cell (Larkum *et al.*, 1999b). The verification of this hypothesis *in vivo* is quite challenging, because visually guided patch-clamping down to deep cortical layer 5 is not feasible with standard two-photon microscopy. To circumvent this problem Helmchen et al. performed blind whole-cell patch recordings of the soma or the main apical dendrite of thick-tufted layer 5 pyramidal neurons in the barrel cortex of an intact rat brain (Helmchen *et al.*, 1999). The patch-pipette was filled with a fluorescent calcium indicator to visualize the superficial tuft dendrites under a two-photon microscope and to record changes in calcium concentrations to detect dendritic activity. The combination of electrical recordings of the apical dendrite and imaging calcium changes in the tuft dendrites allowed for the *in vivo* verification of small dendritic sodium spikes and complex calcium spikes, which were largest close to the main bifurcation of the apical dendrite. Both types occurred during sensory stimulation of the whiskers. By patching the soma of a layer 5 neuron and simultaneously imaging the tuft dendrites, somatic action-potential burst firing was associated with large dendritic calcium spikes. Other *in vivo* studies on dendritic spiking of layer 5 pyramidal neurons omit electrophysiological recordings and solely imaged changes in calcium concentration in tuft dendrites with two-photon microscopy. Those studies verified the existence of local and global calcium spikes in tuft dendrites of pyramidal layer 5 neurons, also in the awake behaving animal (Xu *et al.*, 2012; Cichon & Gan, 2015; Takahashi *et al.*, 2016). The individual recorded neurons in these studies were

39

chosen randomly, but it was known that the single-cell responses to specific stimuli are highly diverse across cortical cell populations (Hromadka *et al.*, 2008; O'Connor *et al.*, 2010). The link between the specific functional role of single cells within large cell populations and dendritic activity or especially dendritic spiking is missing so far. Moreover, in regard to layer 5, mostly thick-tufted pyramidal neurons were studied or slender- and thick-tufted neurons were not differentiated (Xu *et al.*, 2012; Harnett *et al.*, 2013; Cichon & Gan, 2015). Thus, the existence and the functional role of dendritic spiking of slender-tufted layer 5 neurons are largely unknown. These open questions were targeted in this work, by developing a new deep calcium imaging method to directly access cortical layer 5 in the mouse brain *in vivo*.

2 Materials & methods

Surgery

All experimental procedures were performed in accordance with institutional animal welfare guidelines and were approved by the state government of Bavaria, Germany. C57BL/6 mice (postnatal days 29 - 39) of both sexes were used for *in vivo* imaging and electrophysiological recordings. The animals were anesthetized with isoflurane (2% (vol/vol) in O_2) and kept at 37.5° C with a heating pad. Local anesthesia (2% xylocaine) and analgesia (metamizole, 200 mg/kg) were applied, before exposing the skull. After attaching a custom-made chamber to the skull, a craniotomy was performed above the corresponding cortical area. After the surgery, the mouse was transferred to the two-photon microscope and again placed onto a heating pad. The breathing rate, as well as the animal's temperature, were monitored throughout the experiment. The craniotomy was continuously perfused with Normal Ringer solution, warmed up to 37.5° C. The solution contained, in mM, 125 NaCl, 4.5 KCl, 1.25 NaH_2PO_4, 26 $NaHCO_3$, 2 CaCl2, 1 $MgCl_2$, 20 glucose at pH 7.4. During the experiment, the isoflurane anesthesia was set to 0.9% in O_2, except for those experiments including the sedative Chlorprothixene. 4.5 mg/kg were injected after the surgical procedure and the isoflurane was slowly reduced to 0.25% - 0.5% in O_2.

Transcranial flavoprotein imaging

Flavoprotein imaging is based on the changes in autofluorescence of flavoproteins involved in glucose metabolism in mitochondria, which is closely related to neuronal activity (Takahashi *et al.*, 2006; Husson, 2009). In case of recording the barrel cortex, single barrels were mapped with flavoprotein imaging after exposing the skull and before performing the craniotomy (Takahashi *et al.*, 2006). Therefore, the anesthetized mouse was transferred to a widefield microscope (MVX10, Olympus Corporation) and placed on a heating pad. A small drop of 0.9% NaCl covered the skull to increase its transparency. The whiskers at the contralateral side of the cortical recording site were trimmed, leaving only six whiskers intact (C1 - C3 and D1 - D3). During the recordings the whiskers were deflected one by one by inserting them into a borosilicate glass capillary attached to a piezoelectric actuator (fig. 31). Each whisker stimulation consisted of 1 s deflections at 10 Hz. Flavoprotein fluorescence was excited with an LED of a wavelength of 470 nm (M470L2-C1, Thorlabs). The LED light was focused on the skull surface with an objective lens (0.63 x, 0.15 NA objective MV PLAPO, Olympus) where a light power of 3.0 mW was measured. An optical filter cube (Olympus U-M49002XL, excitation filter: 470/40 nm, dichroic mirror: 495 nm high pass, emission filter: 525/50 nm) separated excitation from emission light. The fluorescence was detected with a CMOS camera (Zyla 4.2 Plus, Andor) and images (128 x 128 pixels) were acquired at 10 Hz. The baseline fluorescence was calculated as the mean fluorescence pixel

by pixel 10 frames before the stimulation onset. 5 frames after the stimulation onset, the mean fluorescence of the following 10 frames was calculated and divided by the fluorescence baseline to derive the change in fluorescence for each trial of whisker stimulation. The resulting color-coded images of 20 trials were averaged and filtered with a Gaussian filter (7 pixel diameter). To generate a barrel field map, these recordings were repeated for six the whiskers (C1 - C3 and D1 - D3). The resulting color-coded images were overlaid with a widefield image of the skull to visualize the activated cortical regions in spatial relation to the superficial vasculature. The barrel field map served as landmark for the labeling of layer 5 cells under the two-photon microscope. The animal's breathing rate and temperature were monitored continuously during the mapping procedure.

Calcium dye loading

For single-cell electroporation of a calcium indicator, the salt version of the corresponding dye (Oregon Green 488 BAPTA-1 (OGB-1), hexapotassium salt (ThermoFisher) or Cal-590, potassium salt (AAT Bioquest)) was dissolved in a solution containing in mM, 135 K-Gluconate, 4 KCl, 10 Hepes, 10 Na_2Phosphocreatine, 4 Mg-ATP, 0.3 Na-GTP at pH 7.4. The resulting dye concentration was 4.5-9 mM. Borosilicate glass capillaries were pulled on a vertical puller (PC-10; Narishige), resulting in patch-pipettes with a resistance of 5-7 MΩ. Those were filled with the dye. A single cell was targeted under visual guidance with the shadow-patching approach (Kitamura *et al.*, 2008) and positioned close to the soma. The cell was filled with dye with 1 - 2 squared current pulses of 270 nA for 30 ms, using a NPI amplifier (ELC-01MX and TMR-02M; NPI Electronic GmbH). 50 min to 1 hour after electroporation, the dye diffused into all subcellular compartments and the two-photon recordings were started. In case of targeting a specific cell within a cell population labeled with Cal-590 in layer 5 of the mouse barrel cortex, it was necessary to visualize both, the cells and the pipette tip, simultaneously. However, the cells were supposed to be filled with OGB-1 (hexapotassium salt; ThermoFisher), which is invisible at a two-photon excitation wavelength of 1050 nm. To be able to see the pipette at that wavelength, 150 µM Alexa Fluor 680 was added to the solution.

Cell populations were filled with a calcium indicator by applying the multi-cell bolus loading technique (Stosiek *et al.*, 2003; Garaschuk *et al.*, 2006). The acetoxymethyl (AM) ester of the dye (Oregon Green BAPTA-1, Indo-1, Rhod-2, OGB-1, Cal-520, Cal-590 or Cal-630 (Thermo Fisher or AAT Bioquest)) was dissolved in DMSO containing 20% Pluronic F-127 acid. This solution was diluted to a final concentration of 500 - 1000 µM in extracellular buffer containing in mM, 150 NaCl, 2.5 KCl, 10 Hepes at pH 7.4. The dye solution was filled into a patch-pipette which was inserted into the brain tissue with a micromanipulator down to the cortical depth of choice. The dye was pressure-ejected with 400 - 600 mbar for 1 min, to stain a large area with a diameter of 400 - 800 µm. In case of imaging deep cortical layers,

the labeled area was restricted to a small volume, at the desired depth, to prevent out-of-focus fluorescence. Therefore, the pipette containing the dye solution was stained with BSA Alexa Fluor 594 (Sasaki *et al.*, 2012) (0.2% in PBS; Life Technologies) to guide it to the exact depth of choice with two-photon imaging. Alternatively, the dye solution contained 10 µM Alexa 680 enabling to visualize the spread of the dye online. The diameter of the final volume filled with fluorescent dye, in this case, was 150 - 200 µm. Around 1 h after dye-loading, the cells were imaged with the two-photon microscope.

Two-photon imaging setup

The experiments were performed with two custom-made two-photon microscopes. For the first part of the experiments a microscope was used with optics suitable for excitation wavelengths from 690 nm to 1050 nm. The excitation laser source was a Ti:Sa laser (Mai Tai DeepSee eHP, Spectra-Physics), emitting wavelengths from 690 nm to 1040 nm at a pulse repetition rate of 80 MHz and with a temporal pulse with below 70 fs and including a prechirper.

For the experiments with red-shifted two-photon excitation wavelengths, a new two-photon microscope was built which tolerates wavelengths up to 1300 nm. Laser light with these long wavelengths was provided by a one-box combination of a Ti:Sa laser and an optical parametric oscillator, tunable from 680 nm to 1300 nm (InSight DeepSee, Spectra-Physics). The laser pulse repetition rate was 80 MHz and the temporal pulse width 120 fs. For the Cal-590 based deep imaging experiments, a fiber laser was used with a center wavelength of 1070 nm, a repetition rate of 70 MHz and a single pulse width of 55 fs (Fidelity-2, Coherent). The group velocity dispersion was compensated with a prechirper built into each of the laser-systems. The laser power entering the two-photon microscope was controlled with a Pockel's cell (Polytec GmbH) and the beam diameter was adapted with a beam expander with one of two different coatings (BE02M-B (650 - 1050 nm) or BE02M-C (1050 - 1620 nm), Thorlabs, Inc.). The beam expander could be easily exchanged, depending on the wavelength range used. The same applies to the scan lens, which was used with one of two coatings (AC508150BML (650 - 1050 nm) or AC508150CML (1050 - 1620 nm), Thorlabs, Inc.). The mirrors used to guide the light through the microscope were coated with silver, as well as the scanning mirrors, which consist of a galvanometric mirror and a resonant mirror with a resonance frequency of 12 kHz (Cambridge Technology, Inc.). The scanned light passed through the scan lens and entered an upright microscope (BX51WI, Olympus Corporation), including a tube lens which is also optimized for the full wavelength range. A custom-designed adapter connected the trinocular tube with the objective lens and the single-photon detector. It was designed to keep the distance between the emitted fluorescence of the probe to the detection unit as small as possible. To separate the fluorescence excitation from the emission light, the adapter included a dichroic mirror (HC 775 LP; AHF) which reflected

43

wavelengths from 350 nm to 760 nm and transmitted 790 nm to 1600 nm. The objective lens (40 x, water immersion, working distance: 3.5 mm, numerical aperture: 0.8, Nikon Corporation) was slightly underfilled to still keep a small focal spot, but to reduce the amount of excitation photons entering the sample at high incidence angles and being highly scattered (Dunn *et al.*, 2000). The fluorescence light was detected with one or two photomultiplier tubes (H7422P-40MOD, Hamamatsu) or with a hybrid photo-detector (R7110U-40, Hamamatsu) in combination with a current amplifier (DHPCA-100, FEMTO Messtechnik GmbH).

For dual-color experiments, the fluorescence emitted from OGB-1 and Cal-590 were detected with two photomultiplier tubes and separated with a dichroic mirror, reflecting 425 - 555 nm and transmitting 570 - 650 nm (T 565 LPXR; AHF). Additionally, an optical filter in front of each PMT blocked the light outside the spectrum of each fluorophore (OGB-1: 550 nm short-pass filter, Edmund Optics; Cal-590: 620 nm bandpass filter 620/60 ET; AHF).

A custom-written LabView software was used for microscope control and for analyzing the recorded data. Videos were streamed with one of the following parameter sets: 240 x 48 pixels at a frame rate of 500 Hz, 360 x 120 pixels at 200 Hz, 450 x 300 pixels with a frame rate of 80 Hz, or 600 x 600 pixels at a frame rate of 40 Hz. Z-stacks were acquired with a step size of 0.5 µm, at 40 Hz or alternatively 80 Hz and with a single image integration time of 1 s or 0.5 s. The maximum laser power used for the deep-imaging experiments with Cal-590 was 130 mW. The maximum laser power used to excite OGB1-was 170 mW (for dendritic imaging at a cortical depth of 500 µm).

Electrophysiology

Targeted cell-attached patch-clamp recordings were performed with a HEKA EPC9 amplifier and under visual guidance with a two-photon microscope. Borosilicate glass pipettes were pulled, resulting in patch-pipettes with a resistance of 5 - 7 MΩ. They were filled with 12.5 µM or 25 µM Alexa Fluor 594 dissolved in a solution containing, in mM, 125 NaCl, 4.5 KCl, 1.25 NaH$_2$PO$_4$, 26 NaHCO$_3$, 2 CaCl$_2$, 1 MgCl$_2$, 20 glucose at pH 7.4. In case of targeting a super responding neuron within a stained cell population in layer 5 of the barrel cortex, 150 µM Alexa Fluor 680 were used, instead of Alexa Fluor 594. After approaching the target cell under visual guidance, a seal of 20 - 50 MΩ was formed.

Sensory stimulation

<u>Whisker stimulation:</u>

All the whiskers on the contralateral side of the recording side were trimmed, besides the whiskers C1 - C3 and D1 - D3. The spared whiskers were trimmed to about 1.5 cm. One of the spared whiskers was inserted into a glass capillary, glued to a piezoelectric actuator, which deflected the whisker by about 30° degree to the rostrocaudal direction. Therefore, a

pulse stimulator (Model 2100; A-M systems) applied a train of voltage pulses (50 ms, 10 Hz) to the piezoelectric actuator for 1 second.

In case of the experiments with awake behaving mice, all the whiskers were trimmed, besides the principal whisker of the barrel field that was imaged. A small particle of a ferromagnet of a diameter less than 0.5 mm was fixed to the principal whisker with super glue. A custom-made electromagnetic coil was used to deflect the ferromagnet and thereby the whisker, by applying voltage pulses of 50 ms at 10 Hz for 1 s to the coil. The coil was positioned right in front of the mouse and the distance was adapted until the deflection of the ferromagnet was approximately 30° degree. The whisker was only deflected when the mouse was sitting still without active whisking.

Visual stimulation:

Visual stimuli were presented on a LCD screen (7 inch touch monitor, Faytech) placed 10 cm in front of the contralateral mouse eye, covering 74° x 50° of the mouse visual field. A blue foil which blocks all but the blue components of the light (http://www.farbfiltershop.de) was attached to the front of the screen. An optical bandpass filter (590/104 BrightLine HC, AHF) in front of the photon-detector blocked the blue light of the screen to avoid bleed-through of the visual stimulation. Drifting gratings were presented with MATLAB R2014b (Mathworks) with the "Psychotoolbox" add-on package (http://psychtoolbox.org/). Each stimulation consisted of an intermediate blue screen presented for 30 s (mean luminance 2 cd/m^2). During these 30 s a grating moving from the left to the right side of the screen (0.05 cycles per degree, 1 Hz, mean luminance 2 cd/m^2) was presented for 3 s for two times (see figure 30 B).

Experiments with awake behaving mice

For two-photon imaging experiments on awake behaving mice, a small implant was attached to the skull of the mouse, which was fixed to the microscope, below the objective lens. The mice were thus head-fixed, but able to freely move the rest of the body. A custom-made spherical treadmill with a diameter of 15 cm, as illustrated in fig. 29, was placed under the mouse and the animal's movements were recorded with a magnetic incremental encoder (AEAT-601B,Avago Technologies) mounted to the treadmill's axis. Movements of the mouse, including active whisking, grooming and free running, were observed throughout the experiment with a small camera (fig. 29). The experiments were combined with sensory stimulation, consisting either of visual stimuli presented on a small screen or somatosensory stimulation by deflecting single whiskers.

Pharmacology

APV/CNQX:

A 'super-responding' cell was identified by imaging cell populations in layer 5 of the mouse barrel cortex, filled with Cal-590 AM. This target cell was electroporated with OGB-1 as described above. The dendrites were imaged with a two-photon microscope in cortical layer 1 while the principal whisker of the corresponding barrel field was stimulated. A glass pipette was filled with 100 μM of the α-amino-3-hydroxy-5-methyl-4-isoxazolepropionic acid (AMPA) receptor antagonist CNQX (6-cyano-7-nitroquinoxaline-2,3-dione) and 100 μM the N-methyl-D-aspartate (NMDA) receptor antagonist APV (D-2-amino-5-phosphonovaleric acid) and 10 μM Alexa Fluor 594, diluted in standard extracellular saline solution. The pipette was placed into layer 1, outside the FOV but close to the tuft dendrites. The solution was ejected with short pressure pulses of about 1 second. The same dendrites as before were recorded, while the principal whisker was stimulated. Significance was tested with Wilcoxon signed-rank test (cut-off $p < 0.05$).

Baclofen:

After identifying a 'super-responding' cell in layer 5 of the mouse barrel cortex, it was cell-attached as described before. Action-potentials were recorded, while the principal whisker of the recorded barrel field was deflected. A second pipette was inserted into the tissue and placed superficially to 100 - 150 μm below the cortical surface. The tip of the pipette was placed to the center of the tuft dendrites, filled with Cal-590 AM, which can be visualized under two-photon excitation. The pipette was filled with 100 μM baclofen and 20 μM Alexa Fluor 594, diluted in standard extracellular saline solution. The solution was gently pressure-ejected while imaging. When the solution filled a field-of-view with a diameter of 150 μm, the pressure-ejection was stopped and the action-potentials of the cell-attached cell were recorded, while deflecting the principal whisker. Significance was tested with Wilcoxon signed-rank test (cut-off $p < 0.05$).

Muscimol:

To block potential input sides to the mouse barrel cortex, a second craniotomy was performed above the primary motor cortex M1 (1.1 mm lateral to the midline and 0.9 mm anterior to bregma), or, in another set of experiments, to the secondary somatosensory area S2 (1 mm lateral of the barrel C2). To verify the position of S2, C2 and the primary auditory cortex and the barrel cortex were mapped by imaging flavoprotein fluorescence during whisker stimulation or white noise stimulation with an electrostatic loudspeaker driver and loudspeaker (60 dB; ED1, PA5, Tucker Davis Technologies) placed ~10 cm from the contralateral mouse ear. Under the two-photon microscope, layer 5 cells in one barrel were filled with Cal-520 AM and their dendrites were imaged in layer 1 while stimulating the

principal whisker. A patch-pipette was filled with 625 µM Muscimol and 12.5 µM Alexa Fluor 680, dissolved in standard extracellular saline solution. It was lowered into M1 to a cortical depth of 500 - 600 µm or into S2 to a depth of 650 - 750 µm and the solution was pressure injected for 1 min and with 500 - 700 mbar, while the distribution of the solution was observed with the two-photon microscope. When a large field-of-view of a diameter of 800 µm was filled with fluorescence from the Alexa Fluor 680, the imaging region was switched back to the barrel cortex. The muscimol application was repeated while recording the dendrites in the barrel cortex, combined with whisker stimulation.

Immunohistochemistry

'Super-responding' cells were identified with Cal-590 AM and targeted with single-cell electroporation, as described before. The solution inside the pipette contained 2% biocytin and 150 µM Alexa 680, dissolved in a solution containing in mM, 135 K-Gluconate, 4 KCl, 10 Hepes, 10 Na_2Phosphocreatine, 4 Mg-ATP, 0.3 Na-GTP at pH 7.4. 20 min after electroporation, the mouse was transcardially perfused with 0.1 M phosphate-buffered saline (PBS) and subsequently with 4% paraformaldehyde (PFA). The brain tissue was kept in PFA overnight, cut into 70 µm thick slices, and washed with 0.1 M PBS. The slices were incubated overnight at 4°C in a solution containing 1% Triton X-100 with 1 mg/100 ml streptavidin conjugated to Alexa Fluor 488 or 647 (S11223 or S21374 ThermoFisher) in PBS/NaN$_3$ (5 mM NaN$_3$) The slices were washed in PBS again and mounted with the mounting medium VectaShield onto coverslips. To verify the cortical depth of the recorded neurons, overview pictures of the cortex were taken with a confocal microscope (Olympus FluoView FV3000 cLSM), with the electroporated 'super-responding' neurons labeled with Alexa 488. The depths of the neurons were calculated as percent of the cortical structure, to obtain values independent of tissue shrinkage. Two cells stained with Alexa 647 were fully reconstructed by recording mosaic scans with a confocal microscope (Olympus FluoView FV3000 cLSM) and tracing dendrites and axons with Amira 6.0 (FEI, Thermo Fisher Scientific). The fluorescence signal of one of these cells was enhanced with the tyramide signal amplification (TSA) kit (NEL705A001KT, PerkinElmer Inc.).

Data Analysis

Flavoprotein Imaging:

The changes in fluorescence were calculated by dividing the average fluorescence recorded for 1 s and 0.5 s after the stimulation onset by the baseline fluorescence, which is the mean fluorescence recorded for 1 s before the stimulation onset. Images of 20 trials were averaged and filtered with a Gaussian filter (7 pixel diameter). The resulting images were displayed in pseudo-colors and overlaid onto a widefield image of the superficial cortical vasculature to identify the activated barrel fields.

47

<u>Extracting fluorescence changes during spontaneous activity and sensory stimulation:</u>

Two-photon images were analyzed with self-written codes with LabVIEW 2014 (National Instruments) and MATLAB R2014b (Mathworks). 30 s recordings were averaged and regions of interests (ROIs) were drawn manually. The pixels within the ROIs were averaged over time to extract changes of fluorescence of somata or dendrites. In case of imaging cell populations labeled with an AM dye, an additional ROI was drawn around regions without fluorescent staining and were subtracted from the cellular transients. Single-cell or single-dendrite fluorescence peaks were detected similarly as published before (Jia *et al.*, 2010). The fluorescence traces were split into segments of 2500 ms, starting from 500 ms before simulation onset until 2000 ms after stimulation. The median value of the trace 250 ms before stimulation onset was calculated and subtracted from the 2500 ms segments to correct for fluorescence decay of preceding calcium transients or baseline drifts. To calculate the noise band, the segments were filtered with a high-pass filter with a cutoff at 3.0 Hz and standard deviation was derived. Local maxima were searched in a time window from stimulation onset till 300 ms after stimulation. If the detected peak was larger than six times the standard deviation of the noise band, it was accepted as a response. The final response amplitude was calculated as the average of data points 50 ms after the peak, to correct for shot noise.

The response strength of a cell was defined by the averaged response amplitude. In case of dye loading with the AM version of a dye, the intracellular dye concentration is determined by the intracellular esterase and thus signal amplitudes are comparable across cells and experiments. In case of single-cell electroporation the amount of fluorescent dye inside the cell and thus the signal height depend on the position of the pipette tip in relation to the soma during electroporation and the tip resistance after travelling down to layer 5 of the mouse cortex. To compare 'super-responding' with 'weakly-responding' cells in fig. 37 the difference in brightness was compensated by normalizing the dendritic response amplitudes by the maximum dendritic signal measured throughout all recordings of the corresponding experiment.

The full-width at half maximum of dendritic responses to whisker stimulation was calculated as follows: The fluorescence signal was filtered with an exponentially weighted moving average with a time constant of 35 ms. The response transient was fitted with a linear increase and an exponential decay. The full-width at half maximum of the resulting fit functions was derived.

The kinetics of the calcium transients were calculated from the unfiltered fluorescence transients, recorded at 500 Hz and fitted with MATLAB. The relationship between the number of action-potentials and fluorescence amplitude was derived by choosing high-frequency (>

20 Hz) trains of up to six action-potentials, which were followed by a quiet period of at least 100 ms and comparing these events to the amplitudes of the associated calcium transients.

Reconstruction of tuft dendrites:

Tuft dendrites were reconstructed from z-stacks with the Plugin 'Simple Neurite Tracer' in ImageJ (National Institutes of Health; free online access at rsbweb.nih.gov/ij/) (Longair *et al.*, 2011).

Image processing:

For display purposes only, ImageJ was used to adapt contrast and brightness of average two-photon images. Single-cell reconstructions were performed with Amira 6.0 (FEI, Thermo Fisher Scientific). The figures were created with Adobe Illustrator CS5.

The image contrast was calculated as the fluorescence signal of a soma minus the signal of a dark blood vessel divided by the signal of the blood vessel. This was repeated for the brightest six or more neurons in one field-of-view.

Electrophysiology:

Data from cell-attached recordings were analyzed with self-written codes in MATLAB R2014b (Mathworks). The recordings, digitized at 12 kHz, were band-pass filtered with cutoff-frequencies at 0.2 kHz and 2 kHz. Action-potentials were detected automatically and accepted if their peaks were larger than at least 7 times the standard deviation of the recording. To analyze responses to whisker stimulation, action-potentials were counted within in a window of 1.1 s, starting from the onset of the whisker stimulation. Bursts were defined by high-frequency trains of action-potentials of at least 100 Hz.

3 Results

3.1 Imaging depth limit of standard two-photon microscopy

Before developing a new technique for deep two-photon calcium imaging, the actual limit in imaging depth was measured. Therefore, image qualities and cell activities were analyzed for two classical *in vivo* two-photon experiments, including cell population and single-cell imaging. The data set achieved can be used in direct comparison with future experiments to estimate the progress in breaking the depth limit.

A standard custom-made two-photon microscope was used, consisting of a Ti:Sa laser as excitation light source, a standard photomultiplier tube for fluorescence detection and a scanner unit consisting of a galvanometric mirror and a resonant scanner. The target mouse brain region here is the primary visual cortex because it is a popular model system for sensory processing of the cortex and it is easily accessible from the top of the mouse skull. After anesthetizing the mouse with isoflurane and performing a small craniotomy, a large population of cells was bolus loaded with the AM version of the widely used calcium dye Oregon Green BAPTA-1 (OGB-1 AM) (Tsien, 1981; Stosiek *et al.*, 2003). After one hour loading time, the cells were visualized under the two-photon microscope, with an excitation wavelength of 920 nm. To compare the image quality at different cortical depths, videos of 120 s duration were streamed and averaged at 100 µm, 200 µm, 300 µm and 400 µm below the cortical surface of the mouse (fig. 8 A). The upper two images in fig. 8 A, obtained from superficial cell populations, are of high image quality and contrast. Round and bright circular structures can be easily identified as neurons as well as the even brighter and irregular shaped astrocytes (fig. 8 A). When going deeper into the brain tissue the image quality drops apparently even though the average laser power was increased for a constant image brightness (fig 8 A). However, the strong laser power also enhances the background fluorescence and thus reduces the SNR of the images. Concurrently, the focal spot enlarges with increasing imaging depth because of scattering and aberrations, degrading the image contrast and spatial resolution. These effects explain the blurry images, recorded from 400 µm below the brain surface, as shown in fig. 8 A. This result was quantified in fig. 8 B, which shows the contrast of the images at each recording depth. Compared to the first picture, recorded at 100 µm below the pia, the contrast is reduced by a factor of more than 9 at a depth of 400 µm below the surface.
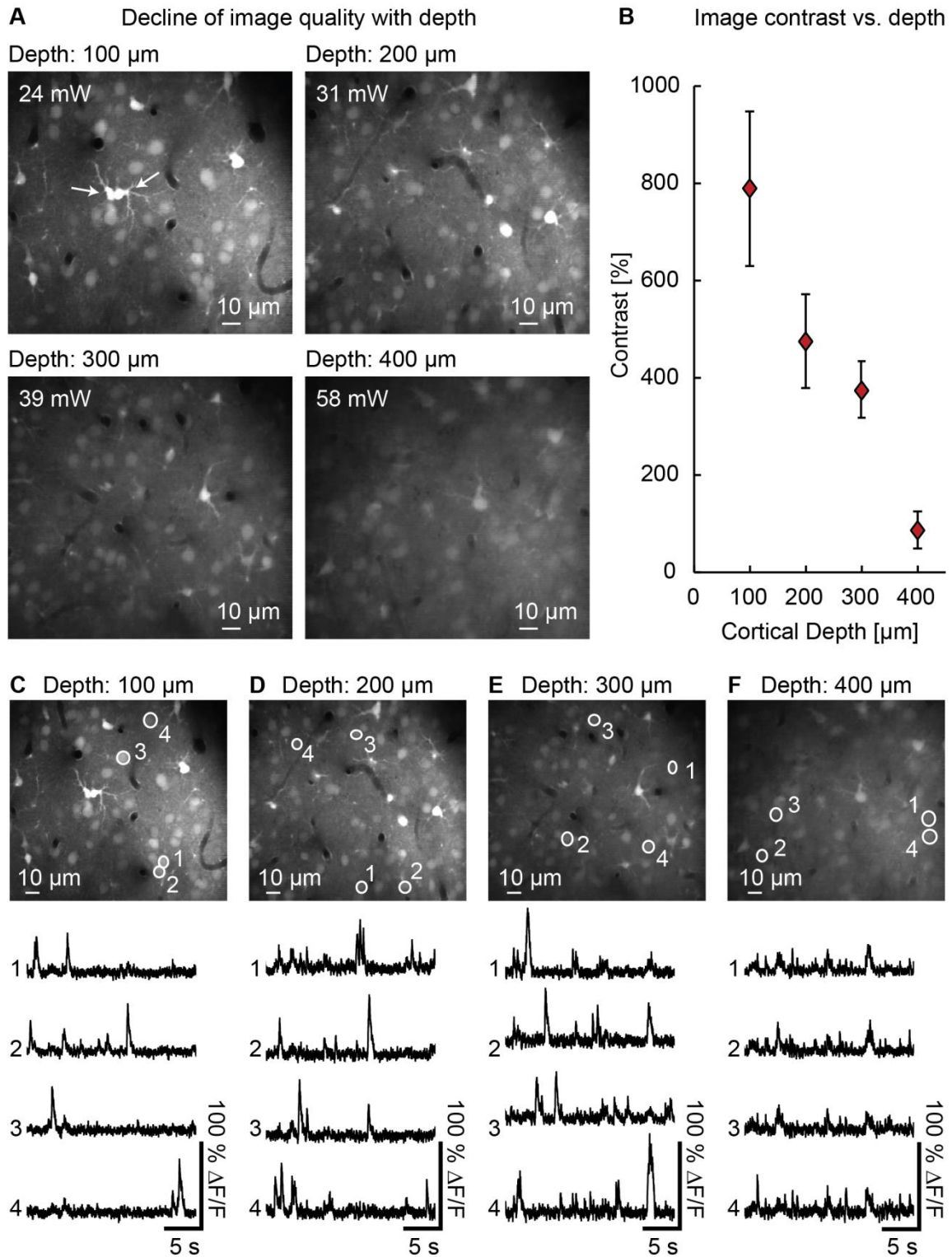
Fig. 8 *Depth limitation of two-photon calcium imaging of cell populations, loaded with OGB-1 AM. (A) Averaged two-photon image recorded for 120 s, with an image frame rate of 40 Hz, at different depths below the pial surface of the mouse. Two of the astrocytes in the field-of-view of the upper left image are marked with white arrows. The average laser power measured under the objective lens is indicated in white letters for each recording. Adjustments of brightness and contrast were the same for all images shown here. (B) Image contrast in each of the four images (mean ± SD), calculated as the fluorescence signal of a soma minus the signal of a dark blood vessel divided by the signal of the blood vessel (n = 6 of the brightest neurons in each image). (C - F) Same images as in (A) but with single-cell activity displayed below each image.*

Good image quality usually comes along with high SNR calcium transients obtained from single-cells within the recorded field-of-view. Single-cell calcium transients recorded from 100 µm to 300 µm below the pial surface have large signal amplitudes and SNR as shown in fig. 8 C - E. However, for the recording from 400 µm depth, the fluorescence amplitudes become smaller and even worse, most single-cell transients strongly resemble each other, because they are dominated by the neuropil signal (fig. 8 F). This effect can be explained by the enlarged volume over which the fluorescence is integrated at depth and which mostly contains dendrites and axons, responsible for the global neuropil signal. Thus, single-cell responses cannot be reliably resolved at 400 µm depth inside the brain tissue and thus these recordings are not accepted for further analysis, to keep a good quality standard without misinterpretations of the fluorescence transients. The resulting limit in imaging depth under these conditions is thus 300 µm, corresponding to layer 2/3 of the visual cortex of the mouse. In comparison, layer 5 is located around 600 µm in the mouse primary visual cortex and around 750 µm in the barrel cortex (for example (Lefort *et al.*, 2009; Groh *et al.*, 2010) or Allen Institute Atlas (Allen Institute for Brain Science)). Thus, the imaging depth needs to be at least doubled to access layer 5 of the mouse cortex.

Besides imaging dense cell populations, another classical *in vivo* two-photon experiment is single-cell imaging, to analyze local subcellular activity in neuronal dendrites. The single cells are therefore filled with a fluorescent calcium indicator by whole-cell patching or electroporation. To test the depth limit under this condition a single cell in the mouse visual cortex was electroporated as deep as possible with the salt version of OGB-1 (9 mM). Surprisingly, it was possible to follow the pipette tip filled with the dye down to 600 µm below the pial surface, corresponding to layer 5 of the primary visual cortex of the mouse. The surrounding cells clearly appeared as dark shadows when ejecting some dye into the extracellular space (Kitamura *et al.*, 2008). Below 600 µm the pipette tip became dim and the cells were not resolvable any more, preventing the electroporation of even deeper cells. For this reason, a cell was electroporated at 600 µm below the surface and after one hour waiting time, the dye diffused intracellularly and the cell could be imaged under two-photon excitation (fig. 9 A). The cell body was easily detectable and even basal dendrites could be recorded at a depth of 600 µm (fig. 9 B). Moreover, dendritic signals were recorded at that depth (fig. 9 C), which required a large amount of laser power of 147 mW at the brain surface.

A Reconstruction of a L5 pyramidal neuron

B Depth: 600 µm

C Basal dendrite
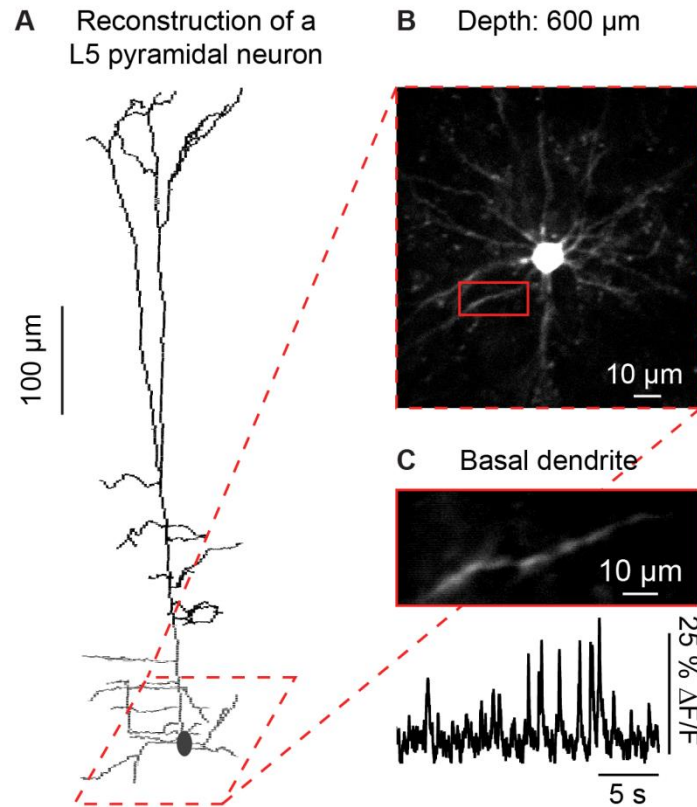
Fig. 9 Depth limitation of single-cell calcium imaging with a two-photon microscope. (A) Morphological reconstruction the recorded pyramidal neuron in layer 5 of the mouse primary visual cortex in vivo. (B) Average two-photon image of the soma and the basal dendrites of a pyramidal neuron, electroporated with 9 mM OGB-1 (30 s recording time, 40 Hz image frame rate). The imaging depth here is 600 µm below the cortical surface and the average laser power applied at the surface is 185 mW. (C) Two-photon image of a basal dendrite recorded at 600 µm below the cortical surface (30 s, 200 Hz frame rate, average laser power: 147 mW)

To be able to record subcellular activity at 600 um might be confusing since based on the previous cell population imaging experiments (fig. 8), the depth limit was around 300 um. This discrepancy can be easily explained by comparing the two imaging circumstances: In case of cell population imaging a large volume of tissue is filled with fluorescent dye, which is not only restricted to the cell bodies, but fills all surrounding dendrites and axons. When imaging structures deep inside the cortex the increased laser power will also excite out-of-focus fluorescence leading to a degraded SNR and contrast (Theer & Denk, 2006; Leray *et al.*, 2008; Chen *et al.*, 2012b). In contrast, in fig. 9 only one single cell is stained and the surrounding tissue is free of fluorescence, allowing for higher imaging depths. The comparison of these two experiments highlights the importance to avoid out-of-focus fluorescence when imaging deep structures of brain tissue *in vivo*. Unfortunately, here we want to image dense cell populations in layer 5 of the mouse cortex *in vivo*. Thus, the new deep imaging method developed here followed two strategies: To increase the penetration depth of the excitation light and to reduce out-of-focus fluorescence. To implement both ideas, three-photon excitation was considered as an option, as described in the next section.

3.2 Three-photon imaging with Indo-1

The aim here was to use the longest excitation wavelength possible, emitted by a Ti:Sa laser, for three-photon excitation of a standard calcium indicator. This corresponds to a wavelength of 1000 nm here, because beyond that the laser power of the Ti:Sa laser is too low to be used for *in vivo* experiments with our two-photon microscope. Thus, a calcium dye was required which is three-photon excitable around 1000 nm. Indo-1 is the most promising calcium indicator for this purpose because of its three-photon excitation peak at 985 nm (Xu *et al.*, 1996), a comparable high three-photon excitation cross-section (Xu *et al.*, 1996) and its comparably good performance under two-photon excitation (Brustein *et al.*, 2003).

After staining a population of cells in layer 2/3 of the mouse primary visual cortex with Indo-1 AM, calcium changes were measured *in vivo* at 750 nm for two-photon excitation and at 985 nm for three photon excitation (Xu *et al.*, 1996). Figure 10 shows the resulting fluorescence images for both cases.
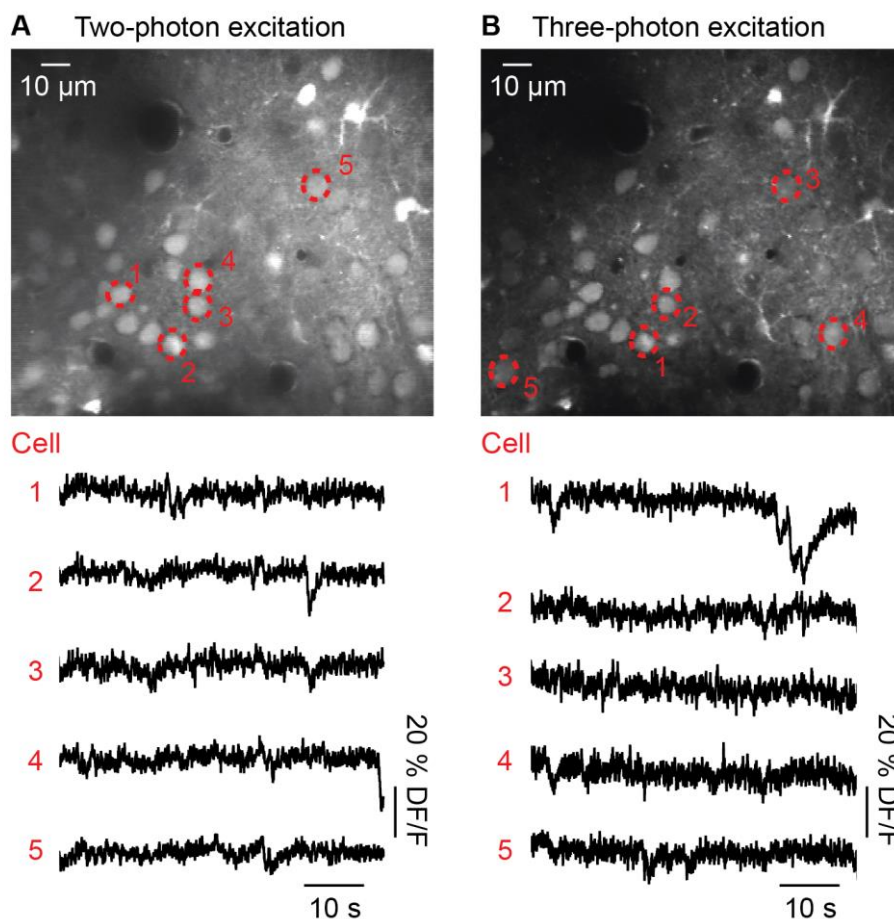
Fig. 10 Two- and three-photon excitation of Indo-1 AM. *(A)* Two-photon image (average of 30 s recorded at 40 Hz) of a cell population filled with Indo-1 AM at a cortical depth of 170 µm below the cortical surface. The wavelength for two-photon excitation was 750 nm and the average laser power at the cortical surface was 9 mW. Below the two-photon image: Spontaneous activity recorded from the cells indicated in red. Note that an increase in calcium concentration is reported as a decrease of fluorescence with Indo-1. *(B)* Same field-of-view as before, but three-photon excited with 985 nm with a laser power of 75 mW at the sample surface (again 30 s at 40 Hz). Fluorescence transients of spontaneous activity recorded from the cells marked in red are displayed below.

The most striking difference between the two pictures is the crisp appearance of cells recorded with three-photon compared to two-photon microscopy. Quantitatively, the contrast between somata and blood vessels is under two-photon excitation 246% ± 61% and 529% ± 47% in case of three-photon excitation. Single-cell calcium concentration changes were reported in both cases and with a comparable signal quality (fig. 10). Note that for this indicator a calcium increase is represented by a fluorescence decrease.

However, there was one drawback of three-photon excitation of Indo-1 compared to two-photon excitation: The maximum fluorescence signal of the somata in the three-photon excited image was 16% ± 6% lower than in the two-photon excited one, even though the average laser power applied at the brain surface was ~8 times higher. As the excitation laser light attenuates exponentially with imaging depth in the brain tissue, even stronger laser power values would be required for deep cortical imaging, which strongly increases the risk of potential tissue damage. Here, 75 mW were used for calcium imaging at a cortical depth of 170 μm below the cortical surface. Thus, three-photon imaging of a focal plane at 500 - 800 μm would require several hundred milliwatts of average laser power at the brain surface. The use of such strong laser light at the sample surface increases the risk of severe tissue damage and in addition the standard laser light source used here cannot provide such high laser power values at that wavelength range. Because of these concerns, the focus of the following sections will be on two-photon instead of three-photon microscopy, but still in combination with long-wavelength excitation. To not be limited in laser power at the wavelength range up to 1300 nm, a new two-photon microscope was setup, which will be described in the following.

3.3 Construction of a new two-photon microscope, optimized for deep imaging

The new two-photon microscope was aimed to fulfill multiple requirements for deep two-photon calcium imaging. First, the laser light source should emit wavelengths beyond the standard range between 800 nm and 950 nm. The ideal case is a tunable wavelength range to offer high flexibility in using different combinations of calcium dyes between and within experiments. Second, the optics need to be adapted to the long wavelengths to prevent damage of the single components and guarantee optimal laser light transmission. Third, two-photon excitation as well as fluorescence emission detection should be optimized to maximize the signal recorded from deep inside the brain tissue. The implementation of the new two-photon microscope, which fulfills all of these criteria, is described in the following sections. Figure 11 schematically shows the new two-photon microscope, which is optimized for deep imaging with long-wavelength excitation light and in table 3 all optical components are listed which were implemented in the microscope.

3.3.1 Two-photon excitation light sources

To offer the greatest flexibility the laser light source should emit light within a tunable wavelength spectrum between 800 and 1300 nm. Beyond 1300 nm water absorption is the dominant light-tissue interaction causing tissue heating (Jacques, 2013; Xu & Wise, 2013; Shi *et al.*, 2016). To avoid this problem, excitation wavelengths between 1000 nm and 1300 nm were favored.

Fortunately, a new laser system appeared on the market recently, providing about 1 W output power across a wavelength range from 680 nm to 1300 nm (fig. 11) (InSight DeepSee; Spectra-Physics). With a pulse repetition rate of 80 MHz and a temporal pulse width below 120 fs, it is well suitable for two-photon excitation. Additionally, a Ytterbium doped fiber laser was built into the system, with an output power of 2 W at a center wavelength of 1070 nm and short laser pulses of 55 fs emitted at a repetition rate of 70 MHz (Fidelity-2, Coherent). This results in a laser duty cycle of $3.9 \times 10^{-4}\%$ which is provides higher two-photon excitation efficiencies, compared to the tunable laser with a duty cycle of $9.6 \times 10^{-4}\%$ for 120 fs and 80 MHz, and reduced photodamage in superficial cortical layers (Birkner *et al.*, 2017). To be able to switch between the two laser systems during or in between experiments a silver mirror on a motorized translational stage was added to the light path (fig. 11). By switching the position of this mirror one or the other laser is coupled into the microscope.

3.3.2 Optics suitable for long excitation wavelengths

To be able to use the entire wavelength range up to 1300 nm all optical components of the microscope need to be coated accordingly to avoid damage of the optics and backreflections into the laser and to offer optimal laser light transmission. Unfortunately, none of our microscopes is suitable for this purpose because the maximal accepted wavelength of most of the optics is between 950 nm and 1100 nm. Even the detection side had to be adapted, because the fluorescence emission will be red-shifted as well in case of long-wavelength excitation. None of the fluorescence should be cut off by the dichroic mirror or the optical filter in front of the single-photon detector, because the fluorescence light levels are extremely low.

Thus, a completely new two-photon microscope was setup and each optical component was chosen carefully to match the long wavelength range of the new laser systems. All the mirrors used in the microscope, including the scan mirrors, are silver mirrors because they reflect on average more than 97% across a wide wavelength range between 450 nm and 2 µm (protected silver mirrors from Thorlabs and scan mirrors from Cambridge Technology, Inc.). The Pockel's cell consists of a LTA crystal, instead of a classical KD*P crystal, which accepts 700 nm - 2000 nm (M360-80, LTA, Polytec). To separate excitation from emission

light, a dichroic mirror was built in which reflects light up to 760 nm. The shortpass filter in front of the photodetector transmits wavelengths up to 760 nm accordingly (HC 775 LP, AHF and 760/SP BrightLine HC, AHF). The most problematic components are the optical lenses, because the focal length depends on the refractive index of the material which depends on the wavelength of the incoming light. It was not possible to choose lenses from standard optics catalogues which cover the entire wavelength range from ~700 nm to 1300 nm. For this reason, two versions of beam expanders and scan lenses were used, which can be easily exchanged during or between experiments without further laser beam alignment. The two sets of lenses covered the two wavelength ranges between 650 nm - 1050 nm and between 1050 nm - 1700/1620 nm (see table below). Each of the lenses consisted of an achromatic doublet, to minimize wavelength dependent shifts in focal length, called chromatic aberrations, induced by different wavelength components within single laser pulses. In case of the scan lens it is critical to minimize spherical and off-axis aberrations because the laser beam is not stationary when entering the scan lens, but is scanned across its surface. For this reason, a scan lens with a large clear aperture of ~5 cm was chosen. The objective lens consists of multiple optical lenses and is probably the most difficult to choose, because many parameters need to match the experimental needs. For most of the standard experiments performed here, a water immersion objective lens with a magnification of 40 x, a long working distance of 3.5 mm and numerical aperture of 0.8 was used. Its major advantages for our *in vivo* experiments are its high transparency for green light and its geometrical shape in combination with the large working distance. Its large access angle and long working distance allow for visualizing the pipette tip inside the brain tissue during an *in vivo* experiment, which is necessary for electroporation, localized bulk-loading and electrophysiology. Because of these advantages this 40 x objective lens was used for the deep imaging experiments as well.
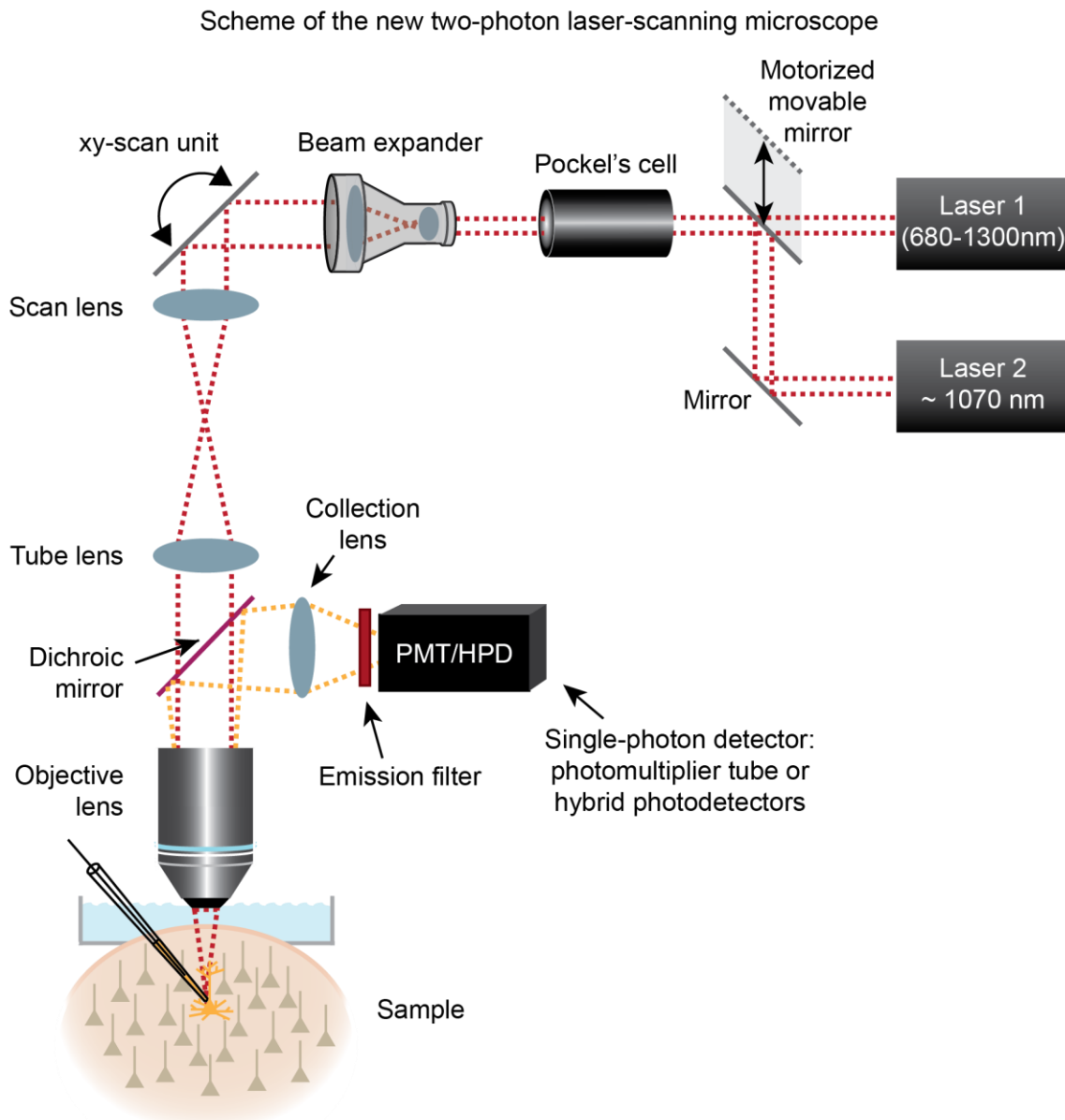
Fig. 11 *Scheme of the new two-photon microscope. The microscope includes two laser light sources. The second laser beam is coupled into the system with a motorized movable mirror. The optics including the Pockel's cell, beam expander, scan lens, tube lens dichroic mirror, collection lens emission filter and all optical mirrors were adapted for long-wavelength excitation laser light up to 1300 nm. The single-photon detector was a special selection of a photomultiplier tube (see main text) or alternatively a hybrid photodetector. The objective lens was slightly underfilled by the excitation laser light beam and the single-photon detector was positioned close to the objective lens with a customized adapter. The individual components are listed in table 3.*

#	Microscope component	Details
1	Microscope body, including tube lens and ocular	BX51WI; Olympus (Special coating for the long wavelength range)
2	Scanner	Resonant scanning mirror (12 kHz) & standard galvanometric mirror (1 kHz), Cambridge Technology, Inc., Operated with NI & LabView
3	Tunable Laser	InSight DeepSee; Spectra-Physics
4	Fiber laser	Fidelity-2, Coherent
5	Pockel's cell	M360-80, LTA, Polytec 700 - 2000 nm Treiber 302A (1MHz)
6	Beam expander	BE02M-B (650 nm - 1050 nm) or BE02M-C (1050 nm - 1700 nm); Thorlabs
7	Dichroic mirror	HC 775 LP; AHF Reflective for 350 nm - 760 nm Transmittive for 790 nm -1600 nm
8	Emission filter	760/SP BrightLine HC, AHF
9	Mirrors	Silver mirrors, Thorlabs
10	Scan lens	AC508150BML (650 nm - 1050 nm) or AC508150CML (1050 nm - 1620 nm); Thorlabs
11	Objective lens	CFI60 Apochromat 40x-W NIR, NA 0.8, WD 3.5 mm, Nikon
12	Photomultiplier tube	H7422P-40MOD, Hamamatsu
13	Hybrid photodetector + amplifier	R7110U-40, Hamamatsu DHPCA-100, FEMTO Messtechnik

Table 3 List of microscope components implemented in the two-photon microscope, optimized for deep two-photon calcium imaging.

3.3.3 Optimization of fluorescence excitation and detection

To optimize fluorescence excitation at deep cortical layer of the mouse brain *in vivo*, the beam diameter was adjusted to slightly underfill the back aperture of the objective lens. For imaging in superficial layers this is highly unfavorable because underfilling the objective lens leads to an enlarged focal spot and hence to a reduced spatial resolution and less excitation light intensity in the focus. In contrast, when the laser is focused deep inside scattering tissue mainly the central part of the beam contributes to signal generation whereas those within the outer cone of the beam generate background fluorescence if any. This effect can be simply

59

explained by the beam geometry: The photons propagating along the outer cone of the beam travel a longer distance inside the tissue, compared to photons in the beam's center, and thus have a higher chance to be scattered (Dunn *et al.*, 2000; Helmchen & Denk, 2005). A recent paper showed the effect of underfilling the objective lens on depth penetration *in vivo* (Kondo *et al.*, 2017).

To optimize the fluorescence detection side as well, the distance between fluorescence generation and detection should be short and the collection lens should have a large aperture to capture as many photons as possible (Zinter & Levene, 2011). Therefore, a custom-made adapter was designed to connect the objective lens and the photomultiplier tube close to each other. The adapter consists of a holder for the dichroic mirror that can be slid in and out of the laser beam path to switch between two-photon imaging and widefield imaging with a small LED. In addition, the adapter includes a biconvex lens and the shortpass filter in front of the photodetector, which is connected to the adapter as well.

The single-photon detector used for deep imaging was chosen carefully because the fluorescence signal recorded from deep inside the tissue is expected to be extremely low. To find the best PMT of those five available in the laboratory, they were directly compared with each other by measuring their output signals at nine distinct light levels (fig. 12). Therefore, a custom-designed light source was used, consisting of a small green LED, dimmed with optical density filters to simulate the low light levels during *in vivo* experiments. The light source was mounted to an adapter for the microscope holder, so that the focal spot of the objective lens can be positioned to the surface of this adapter. The bias voltage of the PMTs was fixed at 700 V and the LED brightness level was increased step by step, by increasing the applied LED voltage. The direct comparison of these five PMTs revealed striking differences in their sensitivity, even though they were of the same model number and from the same company. One of the PMTs, however, was ordered with special selection on high sensitivity and low dark noise (H10770PA-40 SEL). That PMT was by far the most sensitive one, with an output signal that was 21 times larger compared to the PMT with the lowest sensitivity and 11 times larger compared to the second best PMT (fig. 12). For deep imaging experiments with extremely low fluorescence signals this PMT is the best choice and will be used for the following two-photon experiments.

Comparison of PMT sensitivity
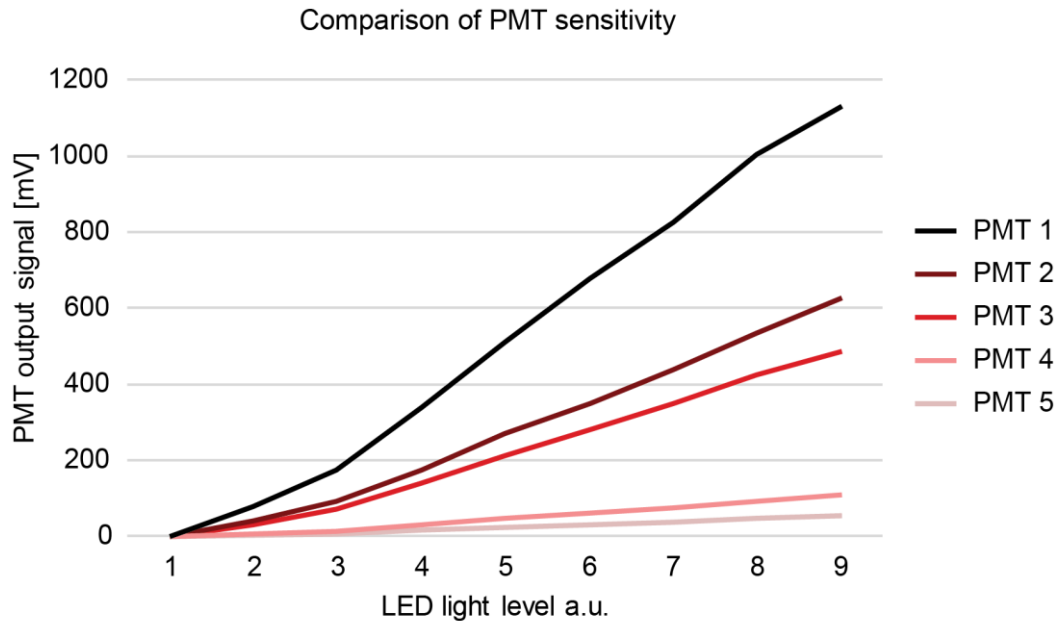
Fig. 12 Comparison of the detection sensitivity of five PMTs of the same model number. The plot shows the output signals of five PMTs (H7422P40MOD; Hamamatsu) in response to nine different low light levels. PMT 1 was a special selection on high sensitivity and low dark noise.

In the experiments of the late phase of my work this PMT was replaced by a hybrid photodetector (R7110U-40, Hamamatsu) for an increase in signal-to-noise of the detected fluorescence, due to reduced excess noise. The output signal of the HPD was amplified with a FEMTO current amplifier (DHPCA-100, FEMTO Messtechnik).

3.3.4   Non-optical components

The microscope consisting of the components listed in table 3 can be readily used for two-photon imaging. However, to perform *in vivo* experiments, certain parts are still missing. First, to keep a mouse under isoflurane anesthesia under the microscope, an isoflurane vaporizer, a heating plate as well as temperature and breathing rate sensors for animal monitoring are needed. To keep the superficial brain tissue at 37° and to supply it with fresh, oxygenated Ringer solution a perfusion system, consisting of a heating and a pump with inlet and outlet tubing is used. Further devices are needed, depending on the specific neural cell labeling procedure. For multi-cell bolus loading a micromanipulator is required to guide the glass pipette through the tissue with micrometer precision. Furthermore, a pressure sensor is used to control the pressure applied to the solution inside the pipette. For electroporation, an amplifier is used that can generate output pulses of (here) 270 nA for 30 ms. If imaging is combined with electrophysiological recordings, a patch-clamp amplifier is required and the system needs to be shielded with a Faraday cage to reduce the electric noise level.

3.3.5   New two-photon setup

The optical components, as well as the laser light sources are placed on an optical table to minimize mechanical vibrations, e.g. caused by traffic. All other devices are placed on a rack

around the microscope that is completely detached from the optical table. The new two-photon microscope, optimized for deep two-photon calcium imaging, is shown in figure 13. Its special features include excitation wavelengths up to 1300 nm, high-power excitation light at ~1050 nm and optimized fluorescence excitation and detection for an improved performance for deep two-photon calcium imaging. During an experiment, the laser light wavelength can be freely chosen between 700 nm and 1300 nm and the experimenter can easily switch from the tunable laser to the fiber laser. Thus, the system can be readily used for deep imaging experiments with long-wavelength excitation. However, there are some practical issues which need to be solved beforehand, which will be explained in the next sections.
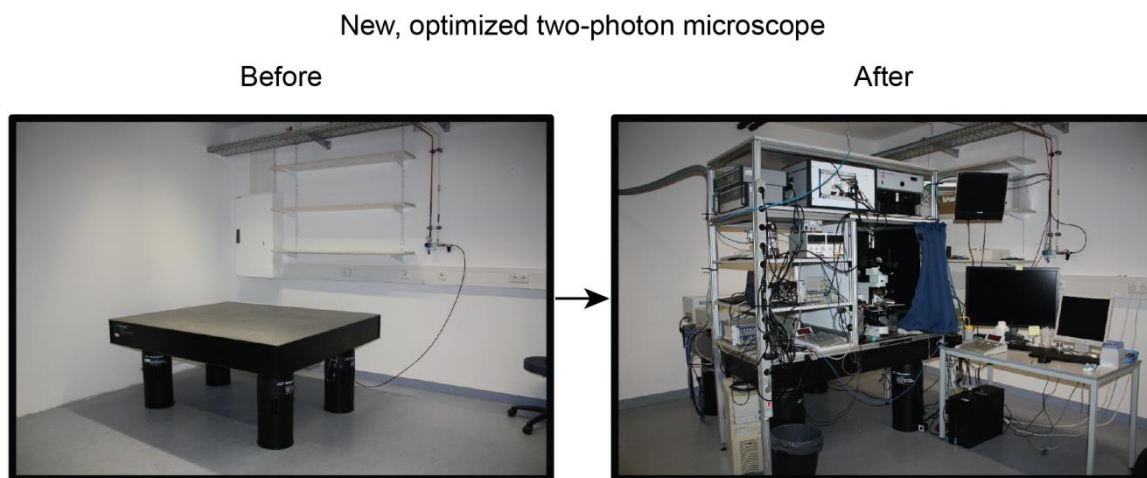
Fig. 13 *Photograph of the optimized two-photon microscope. The microscope includes all components listed in table 3.*

3.4 Optimization of current experimental procedures for deep imaging

To guarantee successful functional recordings from deep cortical layers 5 and 6, some practical difficulties and clues need to be considered. For example, the likelihood of blood vessels lying in between surface and focal plane increases with increasing imaging depth. As blood vessels strongly absorb light this becomes a serious problem for imaging deep cortical layers. Additionally, the emitted fluorescence photons travel a longer distance through the tissue back to the detector and most photons are never detected. Another problem is the increased tissue damage by the prolonged traveling distance of the glass pipette through the brain tissue. One of the most influencing parameter on the maximum imaging depth is the background fluorescence. The deeper the target area, the higher the excitation laser power and the higher is the background. To avoid or reduce these difficulties and to allow for functional imaging in deep cortical layers *in vivo*, several practical aspects need to be followed, which are explained in the following sections.

Avoidance of light-absorbing blood vessels

The light absorption of hemoglobin exceeds that of water or lipid within the fluorescence excitation and emission wavelengths used here (Nachabe *et al.*, 2011; Yao & Wang, 2013). Blood cells on the surface of the brain tissue thus strongly degrade image quality and brightness. For this reason, any bleeding caused during the craniotomy or dye loading should be strictly avoided. But even if there is no superficial bleeding, blood cells can cause dark images of bad quality in case of an imaging field-of-view which is located directly below vasculature. For imaging focal planes in superficial cortical layers this is less a problem because superficial blood vessels are visible at the cortical surface and can be avoided when staining the tissue. However, when imaging deep inside the tissue the likelihood of overlying vasculature increases plus these deeply located blood vessels cannot be identified from widefield images of the brain surface. At least, the probability of multiple blood vessels covering the target region can be reduced by choosing a region which is free of superficial vasculature and far from large blood vessels (fig. 14 B). To target that specific spot for dye loading, the entrance point of the pipette for dye loading has to be calculated beforehand. To increase the chance of a good imaging field-of-view, it is advisable to stain two or three regions and choose the best one for the functional recordings.

Maximization of fluorescence detection

The diameter of the craniotomy should be large enough to prevent that fluorescence photons are blocked by the skull on their way back to the detector. For the objective lens used here (CFI60 Apochromat 40x, Nikon), with a NA of 0.8, and a refractive index of water, of 1.33, the angle of the cone of fluorescence light that can enter the objective lens is about 74°. When imaging at a cortical depth of 800 µm, which corresponds to layer six of the mouse primary visual cortex, the minimum diameter of the craniotomy should be 1.2 mm, as illustrated in fig. 14 A. Because the side of labeled cells is not necessarily in the exact center of the opening, the actual diameter should be larger than that. In the following experiments the size of the craniotomy was chosen to be between 2 to 2.5 mm.

Minimization of tissue damage

Compared to superficial multi-cell-bolus loading, the glass pipette, used for dye loading, needs to travel a long distance through the tissue before reaching layer 5 or 6. To reduce the entailed tissue damage, this distance should be kept as short as possible. Furthermore, the maximum traveling distance of the pipette is limited by the size of the opening. If the incident angle is for example 35° and the target area is at a depth of 800 µm, the travelling distance parallel to the surface is ~1140 µm corresponding to at least half of the entire opening diameter. Thus the point of entrance of the pipette tip needs to be at the very border of the

opening, which is not always possible because of blood vessels covering the brain surface. Any contact between the pipette tip and these blood vessels has to be avoided, to prevent bleedings. In conclusion, the pipette access angle should be as steep as possible to reduce tissue damage and the traveling distance of the pipette (fig. 14 C). This way, the entrance point of the pipette tip can be flexibly chosen at a side free of superficial blood vessels. Here, the maximum access angle of the pipette tip is close to 40°, which is determined by the geometry of the objective lens (CFI60 Apochromat 40x, Nikon).

Correct estimation of the final imaging depth

To make sure that the cells are labeled at the correct cortical depth of choice, it is essential to note that the brain surface is not flat and the skull might not be parallel to the imaging field-of-view. Therefore, it is critical to double-check the position of the pial surface and measure the cortical depth before dye application and before the two-photon recordings. The curvature of the brain sample also determines the optimal imaging side within the craniotomy. Usually, the brain tissue is shallower at the borders of the opening, compared to the center. To minimize the traveling length of the loading pipette, an imaging field in the center of the opening is recommendable (fig. 14 D). In addition, a central imaging position prevents the partial blockage of the fluorescence light by the skull as described before (fig. 14 A)

Avoidance of background fluorescence

For imaging dense cell populations in deep cortical layers, one of the major problems is the background fluorescence from the surrounding labeled tissue (Theer & Denk, 2006; Leray *et al.*, 2008; Chen *et al.*, 2012b). This effect is demonstrated experimentally in section 3.6.1 of this work. Here, a minimized fluorescence background was achieved by restricting the fluorescent calcium dye to a small volume with a diameter of ~150 - 200 µm (fig. 14 E). This size is a good compromise between minimal amount of fluorescence inside the tissue and a reasonably large field-of-view containing up to ~30 cells. To control the size of the labeled volume, the dye loading is performed under visual guidance, by adding Alexa Fluor 680 to the solution inside the glass pipette. The AM version of a fluorescent calcium indicator itself is non-fluorescent as long as the ester is still bound to the dye molecules. The amount of Alexa dye should be as minimal as possible to prevent any contribution to background fluorescence (here 10 µM). Only the pipette tip should be roughly visible and the pressure-ejected solution. Whenever a field-of-view of 150 - 200 µm is filled with Alexa dye, the pressure application is stopped and the pipette is retracted from the tissue.
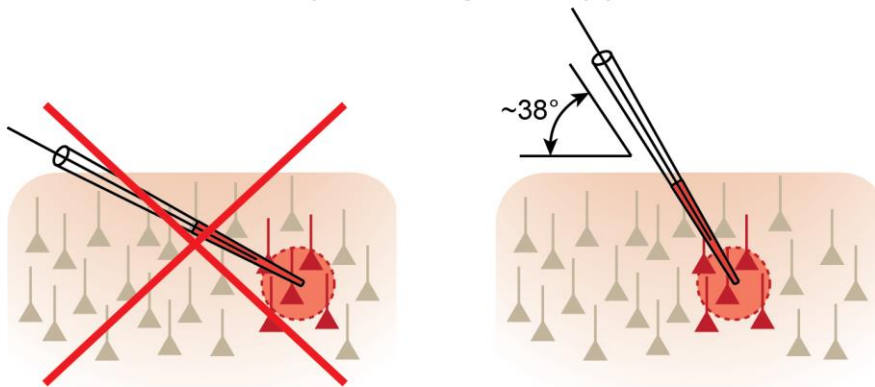
A Optimal diameter of the craniotomy

1.2 mm

0.8 mm

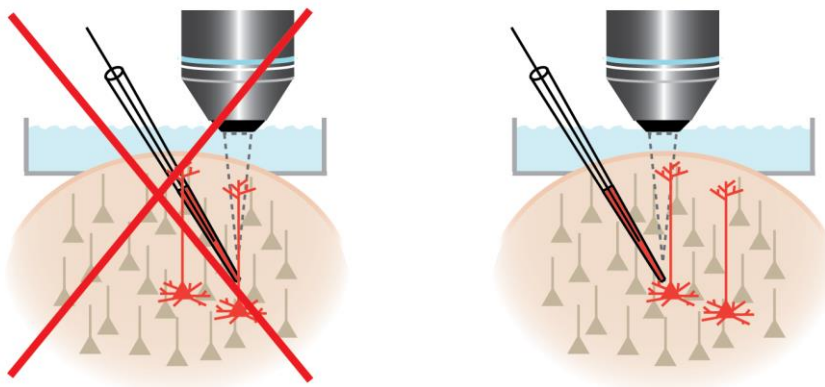3.5 mm
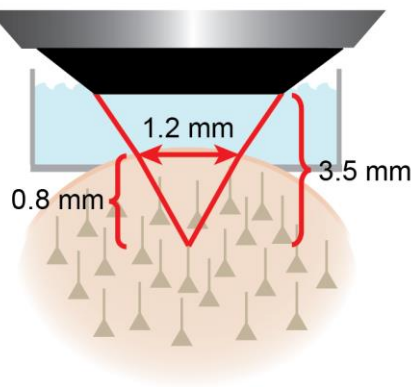
B Blood vessel free imaging side
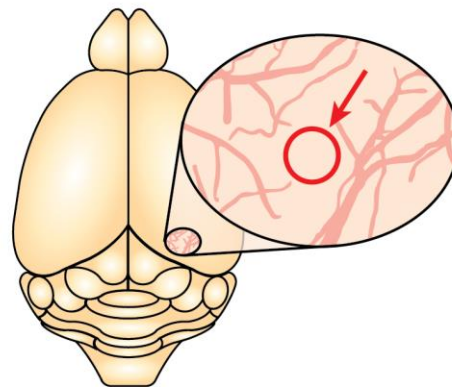
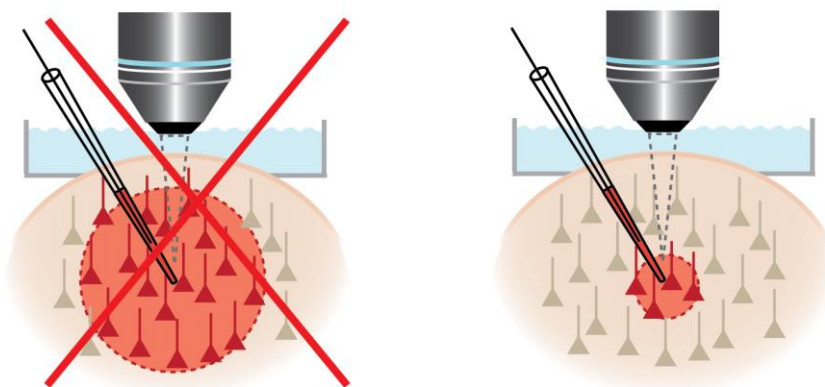**C** Steep access angle of the pipette

~38°

D Central imaging side

E Local dye application

Fig. 14 *Optimization of experimental procedures for deep two-photon calcium imaging.* ***(A)*** *The diameter of the craniotomy needs to be sufficiently large to maximize fluorescence collection. Here, an example is shown for a field-of-view at 800 µm below the cortical surface, recorded with an objective lens with a working distance of 3.5 mm and a front aperture of 6 mm (CFI60 Apochromat 40x, Nikon), leading to a required minimum diameter of about 1.2 mm for the craniotomy.* ***(B)*** *The position of the labeled cells should be in a vasculature-free area, to prevent strong absorption of fluorescence excitation and emission light by blood cells.* ***(C)*** *The access angle of the micropipette should be as steep as possible to minimize the traveling distance through the tissue. For the objective lens used here (CFI60 Apochromat 40x, Nikon), the maximum access angle is 38° degrees.* ***(D)*** *The imaging field-of-view ideally lies in the center of the craniotomy.* ***(E)*** *A spatial restriction of the dye application prevents out-of-focus fluorescence excited in upper cortical layers.*

3.5 *In vivo* application of red-shifted calcium indicators

3.5.1 Two-photon experiments with the red-shifted indicator Rhod-2 AM

To increase the maximum imaging depth, the idea was to combine the optimized experimental procedures described above with red-shifted excitation wavelengths. But to make use of wavelengths beyond 1000 nm, a calcium indicator needs to be identified which is two-photon excitable in the wavelength range between 1000 nm and 1300 nm and which is well suitable for imaging neurons *in vivo*. The most promising red-shifted calcium dye listed in table 1 is Rhod-2 because it was successfully applied to neuronal calcium imaging *in vitro* in zebrafish (Yaksi & Friedrich, 2006). Here, superficial layers of the mouse cortex *in vivo* were stained with Rhod-2 (500 µM) with the multi-cell bolus loading technique. Deep cortical structures were labeled under visual guidance, by adding 10 µM of Alexa Fluor 594 to the solution inside the pipette. In previous studies, Rhod-2 was mostly used *in vivo* to image astrocytes (Tian *et al.*, 2006) which can be readily identified by their bright appearance and their non-uniform shape (fig. 15 A). In contrast, neurons were hardly visible in superficial as well as deep cortical layers (fig. 15). Nevertheless, neuronal calcium transients were successfully recorded *in vivo* from an imaging depth of 800 µm below the cortical surface. To my knowledge this was the first time cell populations in layer 6 of the mouse cortex were recorded functionally *in vivo*. However, the imaging quality and the SNR of the calcium transients did not fulfill our expectations, so that we kept on looking for other red-shifted calcium indicators.
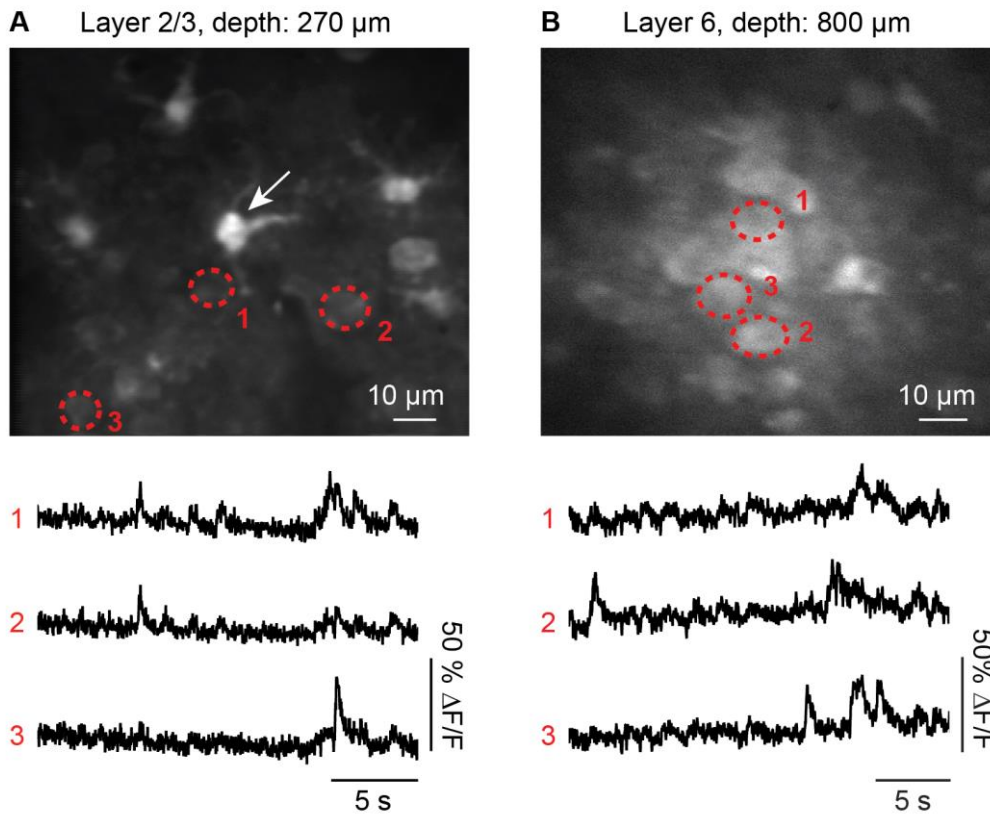
Fig. 15 *Example for in vivo neural population imaging with Rhod-2 AM, two-photon excited at 1050 nm.* ***(A)*** *Multi-cell bolus loading of Rhod-2 into layer 2/3 of the mouse primary visual cortex. The image shows an average of a 30 s recording, acquired at 40 Hz with an average laser power of 8 mW and at a cortical depth of 270 µm. The transients below reflect spontaneous activity from neurons marked in red. The white arrow depicts an astrocyte.* ***(B)*** *Same as in (A) but the recordings were obtained at a cortical depth of 800 µm. The average laser power at the sample surface was 141 mW.*

3.5.2   Characterization of the new red-shifted calcium dyes Cal-590 and Cal-630

3.5.2.1   Two-photon excitation of Cal-590 and Cal-630

The two promising candidates of red-shifted calcium indicators, Cal-590 and Cal-630, appeared on the market recently and were tested for *in vivo* applications here. The optimal two-photon excitation wavelength of a fluorophore is typically not exactly double the single-photon excitation wavelength (So *et al.*, 2000). It has to be determined experimentally by measuring the fluorescence of the fluorophore under excitation with different wavelengths. The average fluorescence detected is linearly proportional to the two-photon excitation action cross-section and the peak point of fluorescence thus corresponds to the optimal two-photon excitation wavelength (Albota *et al.*, 1998). 9 mM of Cal-590 or Cal-630 dissolved in a solution containing 2 mM calcium were filled into a glass pipette and dipped into the recording chamber filled with saline solution. The average fluorescence was measured between 850 and 1100 nm in steps of 50 nm and with an average laser power of 12 mW under the objective lens. The resulting two-photon excitation action cross-section curve is displayed in figure 16 Cal-590 shows a peak at 1050 nm and Cal-630 seems to have its two-photon excitation peak at a wavelength longer than 1100 nm. Cal-590 was thus measured in

67

smaller steps of 10 nm between 1010 nm and 1100 nm and Cal-630 was excited with steps of 25 nm between 1000 nm and 1225 nm. The resulting optimal two-photon excitation wavelength of Cal-630 is 1125 nm. For Cal-590 it lies between 1050 and 1060 nm, which fortunately matches the emission wavelength of ytterbium-doped fiber lasers.
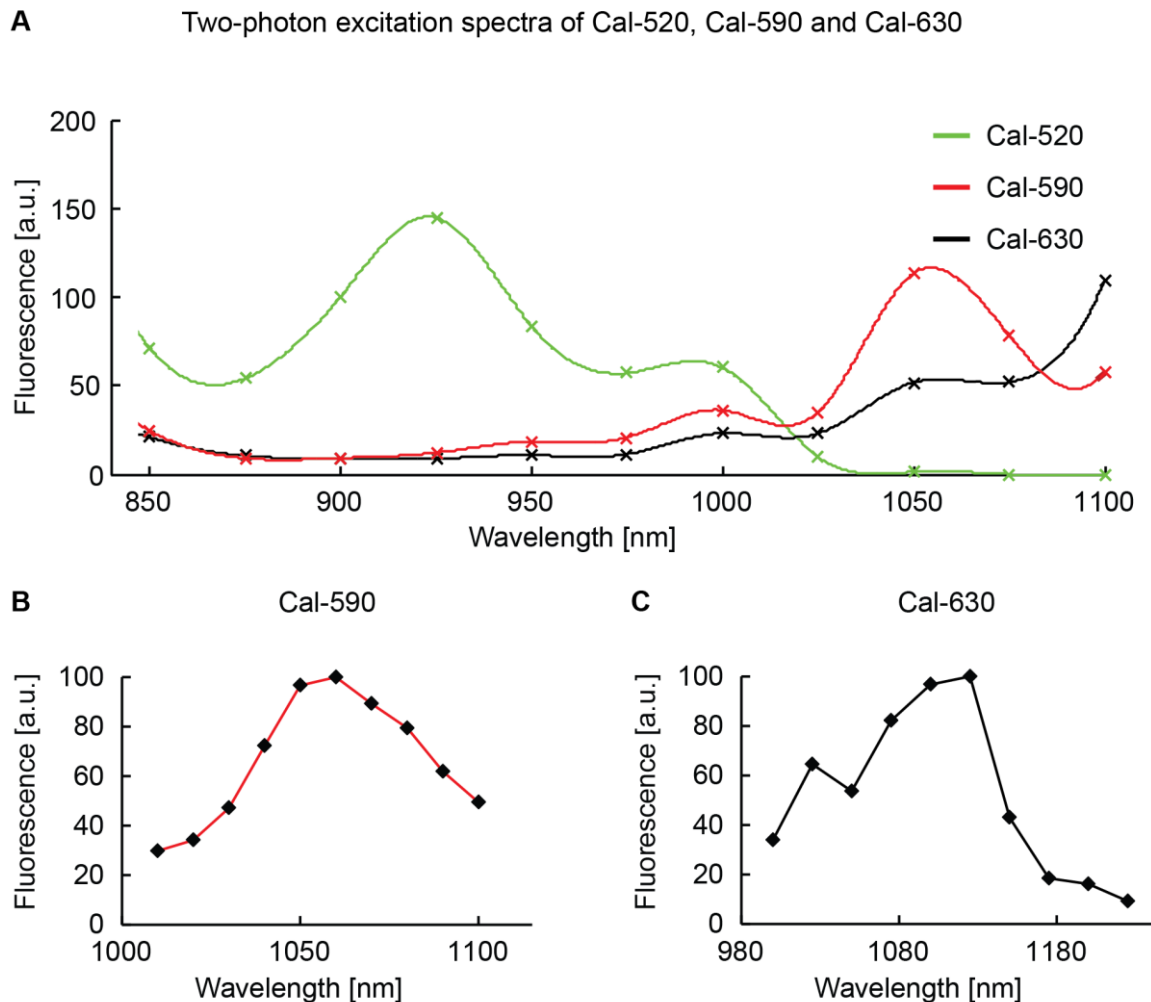

Fig. 16 *Two-photon excitation spectra of Cal-520, Cal-590 and Cal-630. **(A)** Two-photon excitation spectra of the three dyes, indicated in green (Cal-520), red (Cal-590) and black (Cal-630), measured for an excitation spectrum between 850 nm and 1100 nm in steps of 50 nm. The single data points are interpolated with a polynomial function for display. **(B)** Two-photon excitation spectrum of Cal-590 for wavelengths between 1010 nm and 1100 nm measured in steps of 10 nm. **(C)** Same as in (B) but for Cal-630 between 1000 nm and 1225 nm, measured in steps of 25 nm.*

### 3.5.2.2 *In vivo* application of Cal-590 AM and Cal-630 AM

The new red-shifted calcium indicators were injected into layer 2/3 of the mouse primary visual cortex to test their applicability to *in vivo* cell population imaging. After 60 min loading time Cal-520 was excited with 920 nm (27 mW), Cal-590 with 1050 nm (33 mW) and Cal-630 with 1125 nm (43 mW). In all three cases the cytosol of the cells was homogenously filled with fluorescent dye and the nuclei were spared out, resulting in a ring-shape appearance of the neurons. Spontaneous activity was recorded successfully with each of the dyes with comparable quality of the single-cell transients as shown in fig. 17. The most obvious

difference between the dyes were different baseline fluorescence levels. Cells filled with Cal-520 AM are brighter than those filled with Cal-590 AM under baseline conditions, and the staining with Cal-630 AM resulted in the lowest baseline fluorescence values. Also, the single-cell signal amplitudes seem to be smaller for Cal-630 AM which is quantified in the next section by combinations with electrophysiological recordings. Note that in fig. 17 different laser power values were used for the recordings and also the contrast and brightness of the images were adjusted for display purposes.
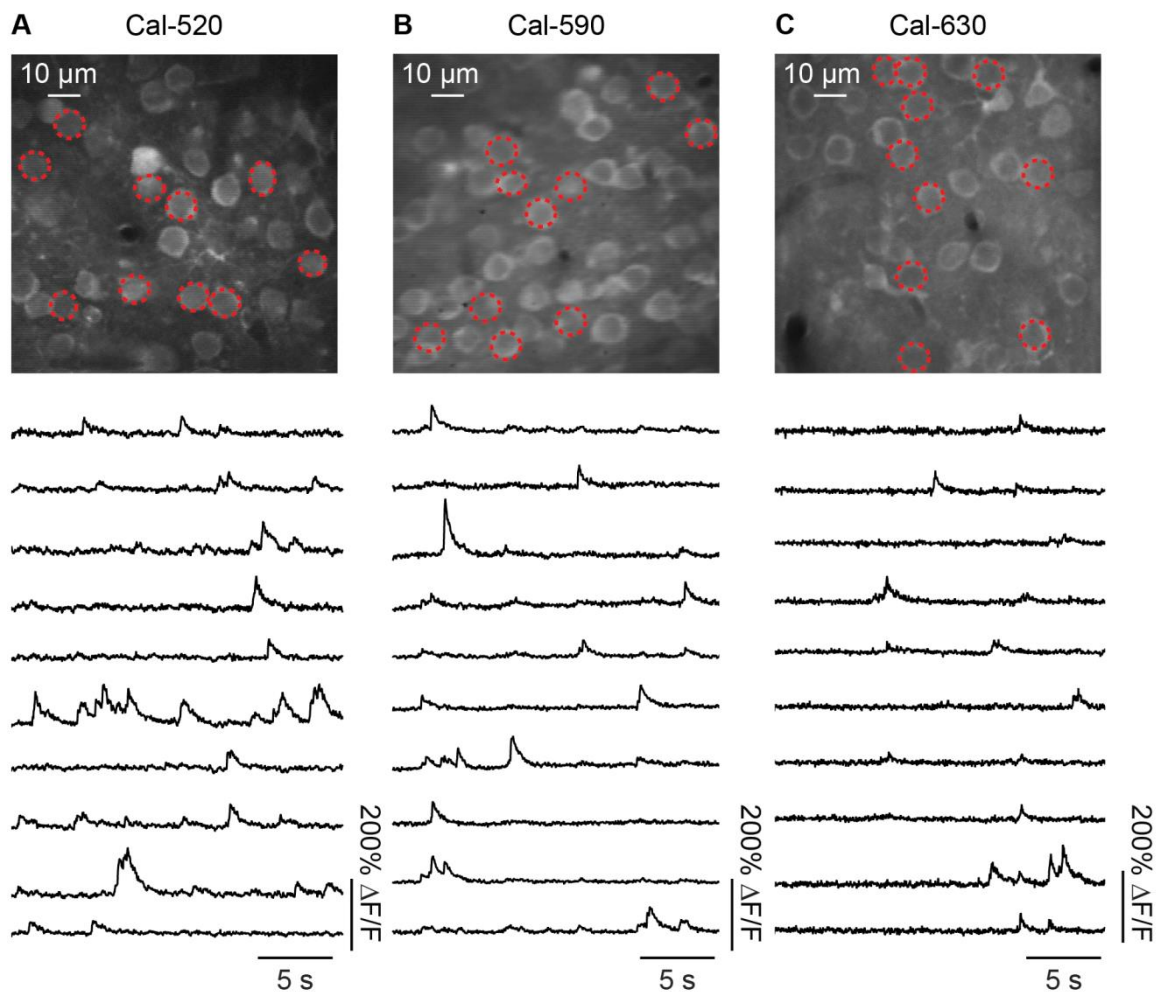
Fig. 17 *Examples for calcium imaging of cell populations stained with Cal-520 AM, Cal-590 AM or Cal-630 AM in vivo. (A) Two-photon image of a cell population filled with Cal-520 AM, two-photon excited at 920 nm. Cells at a cortical depth of 157 µm were recorded for 30 s at a frame rate of 80 Hz and with an average laser power of 27 mW measured under the objective lens. The fluorescence transients below show spontaneous activity recorded from the cells marked in red. (B) Same as in (A) but the cells were filled with Cal-590 AM which was excited at 1050 nm and with an average laser power of 33 mW. The focal plane here is 148 µm below the cortical surface. (C) Same recordings as in (A) and (B) but with cells filled with Cal-630 AM, excited with an average laser power of 43 mW at a wavelength of 1125 nm. The imaging field-of-view is located 154 µm below the pial surface. The brightness and contrast of the averaged images were adapted for display.*

It must be noted that besides the neurons, astrocytes are labeled as well with the Cal-dyes. Those can be easily identified by their non-uniform morphology demonstrated here by counterstaining astrocytes with sulforhodamine 101 shown fig. 18 (Nimmerjahn *et al.*, 2004).
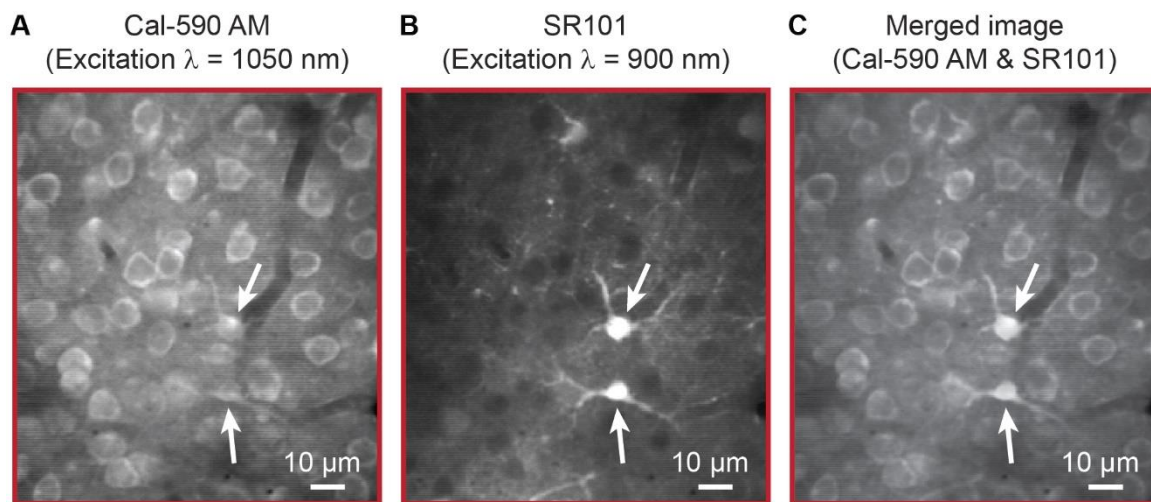
Fig. 18 *Imaging astrocytes with Cal-590 AM. **(A)** Cortical layer 2/3 cells filled with Cal-590, excited at 1050 nm (30 s, 80 Hz frame rate). White arrows point to two astrocytes. **(B)** Counterstaining of astrocytes with sulforhodamine 101, excited at 900 nm (30 s, 80 Hz frame rate). Astrocytes marked with white arrows. **(C)** Merged image of (A) and (B)*

Surprisingly, Cal-630 has a severe drawback compared to Cal-520 and Cal-590. The cells filled with Cal-630 were nicely stained after a waiting time of 60 min after dye application, however, the staining vanished over short time. The decrease in fluorescence was not observed within recordings of 30 s, which would indicate bleaching effects, but in between short recordings, acquired at different points in time. For quantification, a 30 s recording of a cell population filled with Cal-630 AM was acquired every 30 min after dye application. The average laser power, the zoom, the imaging speed and the photodetector settings were the same across the recordings. As shown in fig 19 the cell bodies darken with time and the surrounding extracellular space becomes brighter, probably because the dye is diffusing outside the cells and is enriched extracellularly. For direct comparison of the contrast of the time lapse images lineplots across a cell in focus are plotted for each image (fig 19). Note the two peaks of the plots which correspond to the cytosol of the cells filled with fluorescent dye. 30 min after dye injection the cytosol is 57% brighter compared to the neuropil around, but after 60 min it already decreased to 36%. After 90 min the overall brightness of the image is very high, indicating a high background fluorescence originating from fluorescence dye that diffused in the extracellular space. The difference between the cells' cytosol and the neuropil is only 14%. 150 min after dye application the cells appear as dark holes on a fluorescent background and the cytosol is as dark as the background. This temporal deterioration in image quality limits the recording time with Cal-630 to about only one hour. For *in vivo* experiments at least two hours recording time are usually necessary to acquire enough data for proper analysis. If two-photon imaging is combined with electrophysiology or with behavioral tasks of the mouse, the required recording time can be even longer. For this reason, the focus of the following sections will be on Cal-590 which did not show this drastic

decrease in intracellular fluorescence over time (fig. 20). Even 155 min after dye loading there is only a minor decrease in contrast and the cells are still clearly visible (fig. 20).
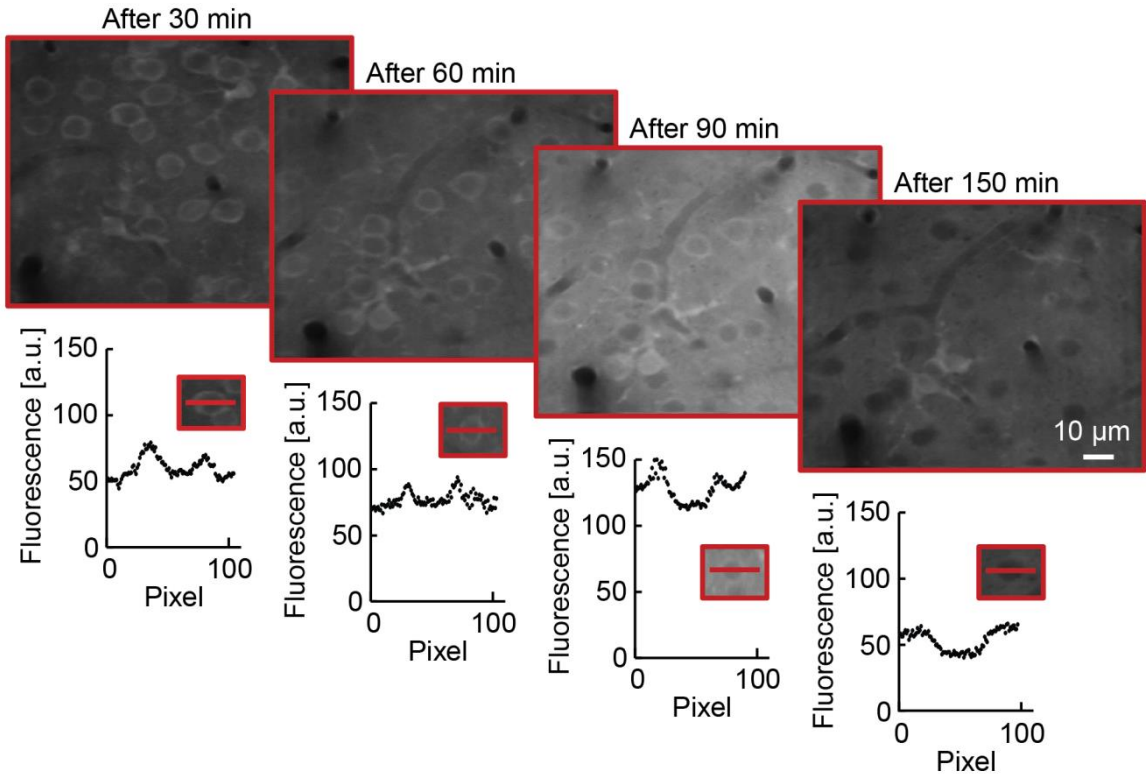
Fig. 19 *Time-lapse images of Cal-630 AM filled cells. Each two-photon image shows an average image of cells stained with Cal-630 AM, recorded at a cortical depth of 198 µm for 30 s at a frame rate of 80 Hz. The fluorescent dye was excited with 1125 nm and with an average laser power of 43 mW for each image shown. The contrast and brightness were equally adjusted in all images for display purposes. Lineplots across single cells are displayed below, to compare brightness and contrast.*
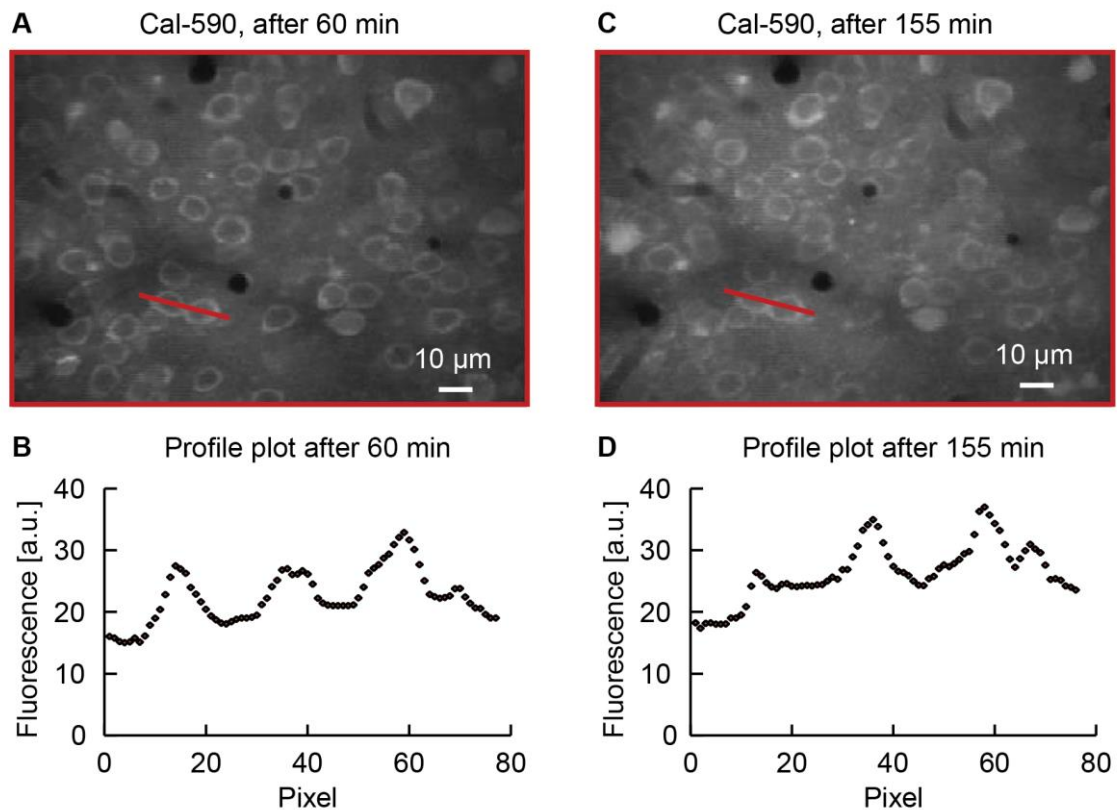
Fig. 20 *Time-lapse images of neural cells filled with Cal-590 AM.* **(A)** *Average image of layer 2/3 cells filled with Cal-590 AM 60 min before the recording (30 s, 80 Hz frame rate, 21 mW average laser power, recording depth: 201 µm)* **(B)** *Lineplot across two cells of the image above to visualize the image contrast.* **(C)** *Same as in (A) but 155 min after dye loading.* **(D)** *Lineplot across the same two cells shown in (A) and (B). The imaging paramters, including the laserpower were the same for the two recordings, as well as the adjustments in image brightness and contrast for image display.*

3.5.2.3 Calcium-reporting properties of Cal-590 and Cal-630

After demonstrating the general applicability of Cal-590 AM and Cal-630 AM to *in vivo* experiments, their calcium-reporting properties were analyzed in detail. For the following dye characterization I teamed up with my colleague Carsten Tischbirek, who became aware of the new red-shifted dyes online.

The AM version of Cal-590 and Cal-630 were pressure injected into layer 2/3 of the mouse visual cortex *in vivo*. For quantification of the fluorescence signals, single cells in the imaging field-of-view were recorded in the cell-attached mode. Spontaneous activity was recorded at a high imaging speed of 500 Hz, while action-potentials were recorded simultaneously (fig. 21 A & D). Action-potential firing was always associated with fluorescence changes and, despite the high $K_d(Ca^{2+})$ value of Cal-590, single action-potentials could be clearly resolved with high SNR (fig 21 E) (Tischbirek *et al.*, 2015). Cal-630 has an even lower calcium affinity, explaining the small amplitudes of single action-potential evoked fluorescence changes, which were close to baseline (fig. 21 B). The amplitudes of the fluorescence transients related linearly to the number of action-potentials for both dyes (fig. 21 C) (Tischbirek *et al.*, 2015). Single action-potential evoked calcium transients reported by Cal-590 showed rapid

kinetics with a rise time smaller than 2 ms and a decay time of 255 ms (mean of 55 events from three animals; fig. 21 F) (Tischbirek *et al.*, 2015). The single-action-potential-evoked signals reported by Cal-630 were too small in amplitude for this kind of analysis. In summary, Cal-590 is a promising candidate for deep two-photon calcium imaging because of the high SNR of reported single-cell activity, of the linearity between action-potentials and fluorescence changes and because of its rapid kinetics.
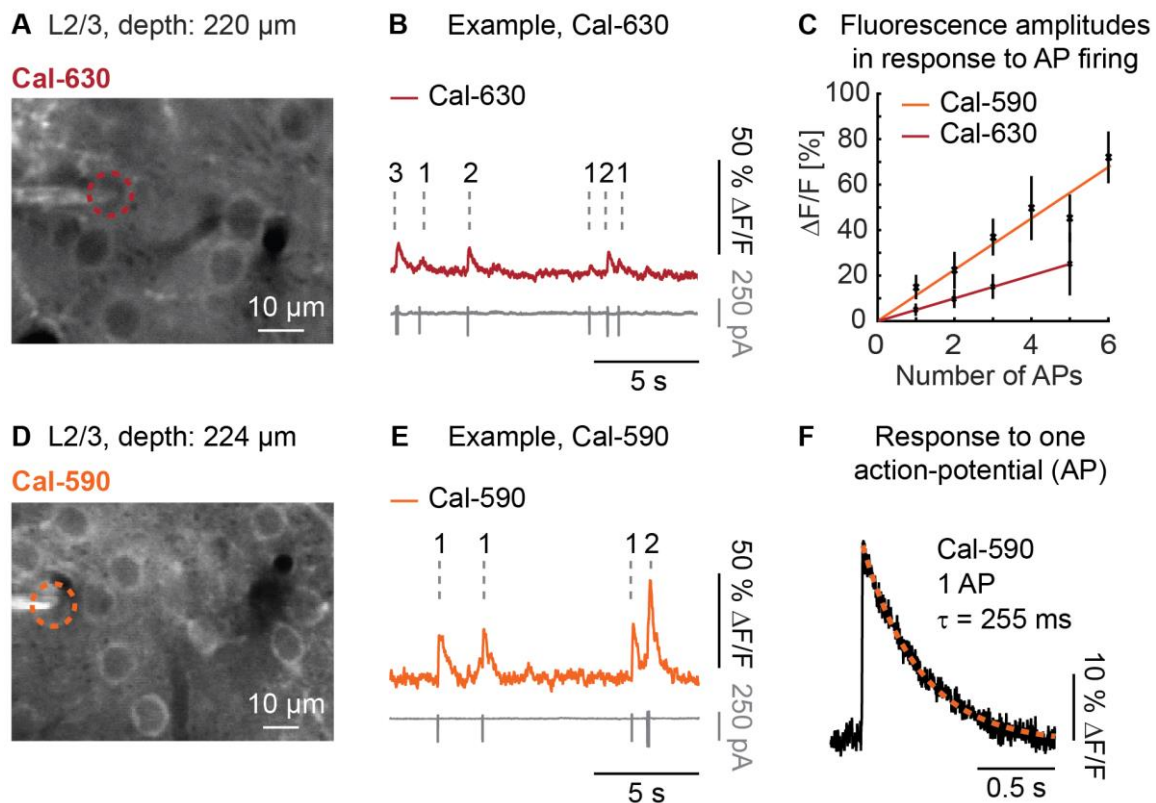
Fig. 21 *Calcium-reporting properties of Cal-590 AM and Cal-630 AM in vivo. (A) Two-photon average image (30 s, 80 Hz, 1125 nm excitation wavelength) of a cell population filled with Cal-590 AM, used for cell-attach recordings from the cell marked with the red-dotted circle. The recording was obtained from layer 2/3 (L2/3) of the mouse primary visual cortex, at a cortical depth of 220 µm below the pial surface. (B) Example for spontaneous activity, recorded from the cell marked in (A). The red trace shows the calcium concentration changes measured with Cal-630 AM at a frame rate of 500 Hz. The grey trace below shows the action-potential firing of the cell, recorded simultaneously. The numbers above the recording indicate the number of action-potentials measured in the cell-attached mode. (C) Graphical display of the number of action-potentials versus the somatic fluorescence amplitudes (mean ± SD). The red line represents the linear fit to the data recorded with Cal-630 AM and the orange line shows the linear fit to the data acquired with Cal-590 AM. (D) Same as in (A) but the cells are loaded with Cal-590 AM, which was excited at 1050 nm. The cell-attached cell is marked with an orange-dotted circle. (E) Example of spontaneous activity recorded from the cell filled with Cal-590 AM, illustrated similarly as in (B). (F) Average of fluorescence transients corresponding to single action-potentials (mean of 55 events, recorded in three animals). The orange dotted line represents the single-exponential fit used to derive the decay time-constant of 255 ms. (Figure was adapted from (Tischbirek et al., 2015))*

To characterize the fluorescence signal dynamics of single-cells labeled with Cal-590, layer 5 neurons in the visual cortex of the mouse were electroporated with the salt version of the dye (Tischbirek *et al.*, 2015). The electroporated cells were cell-attached to simultaneous record action-potential activity and calcium concentration changes reported by Cal-590. Two different cellular compartments were therefore imaged at a high speed of 500 Hz: The soma

and the dendritic trunk about 100 µm above the cell body (fig. 22 A). As expected from different surface-to-volume ratios of the dendrite and the soma, action-potential evoked calcium signals were much faster in the dendrite compared to the soma (fig. 22 B and D) (Tischbirek *et al.*, 2015). Dendritic single action-potential signals had a rise time smaller than 2 ms, which is the shortest time resolvable here, and a decay time of 20 - 30 ms (fig 22 C; n = 4) (Tischbirek *et al.*, 2015). In comparison, the somatic decay time is more than 10 times slower (fig 21 F). This rapid performance allowed for the recording of high frequency trains of action-potentials with distinguishable peaks for each action-potential, up to a frequency of 100 Hz (Tischbirek *et al.*, 2015).
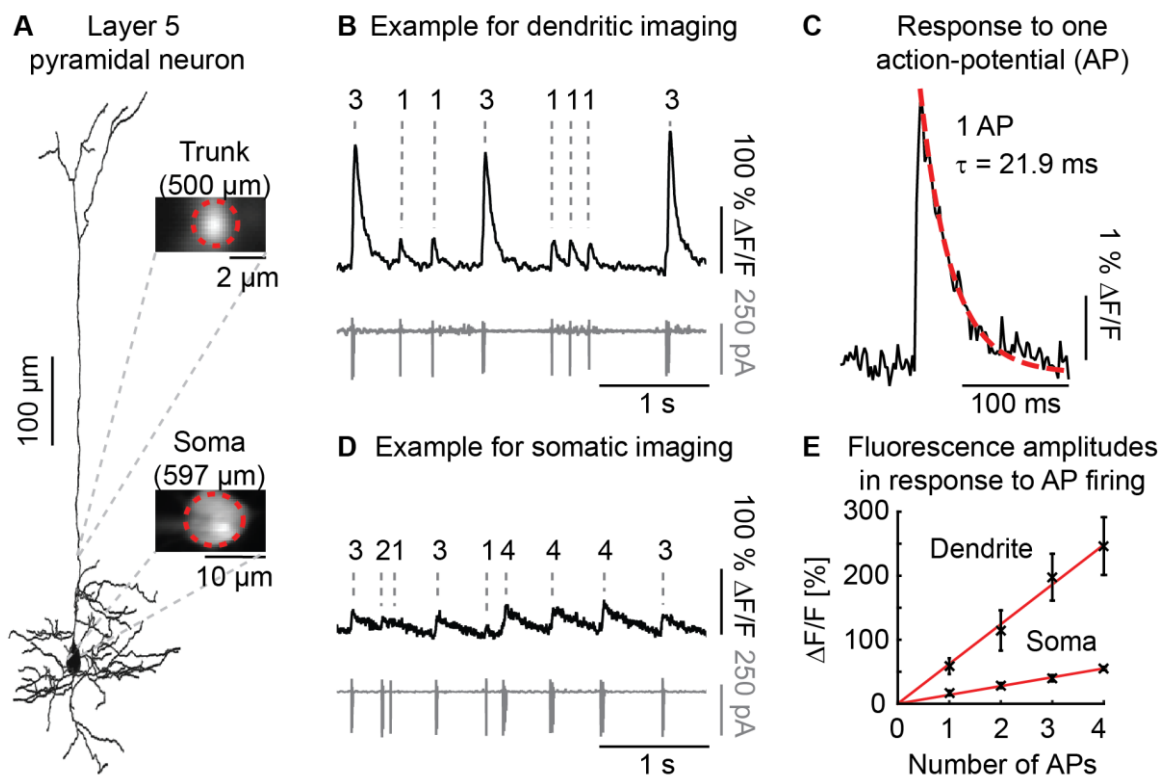

Fig. 22 *Calcium imaging of a single layer 5 pyramidal neuron, electroporated with Cal-590. (A) Morphological reconstruction from a z-stack of a layer 5 neuron electroporated with the salt version of Cal-590 in vivo. Two-photon images recorded from the soma and the proximal trunk are shown next to the single-cell reconstruction. Regions of interest used for the analysis are marked with red-dotted circles. (B) Example for a dendritic recording of spontaneous activity. The calcium transient is shown in black (500 Hz) and the action-potentials, recorded in the cell-attached mode, are displayed in grey. The numbers of action-potentials are indicated above the calcium transient. (C) Dendritic response to single action-potential events (average of 14 traces). The red-dotted line corresponds to the linear exponential fit used to derive the decay time. (D) Example for somatic spontaneous activity, arranged as the dendritic recording in (B). The black trace represents the two-photon recording (500 Hz frame rate) and the grey trace shows the action-potentials, recorded simultaneously. (E) Number of action-potentials plotted against the amplitudes of the fluorescence transients, recorded from the soma and the proximal dendritic trunk (as shown in (A); mean ± SD). Linear fits are displayed with red lines. (Figure was adapted from (Tischbirek et al., 2015))*
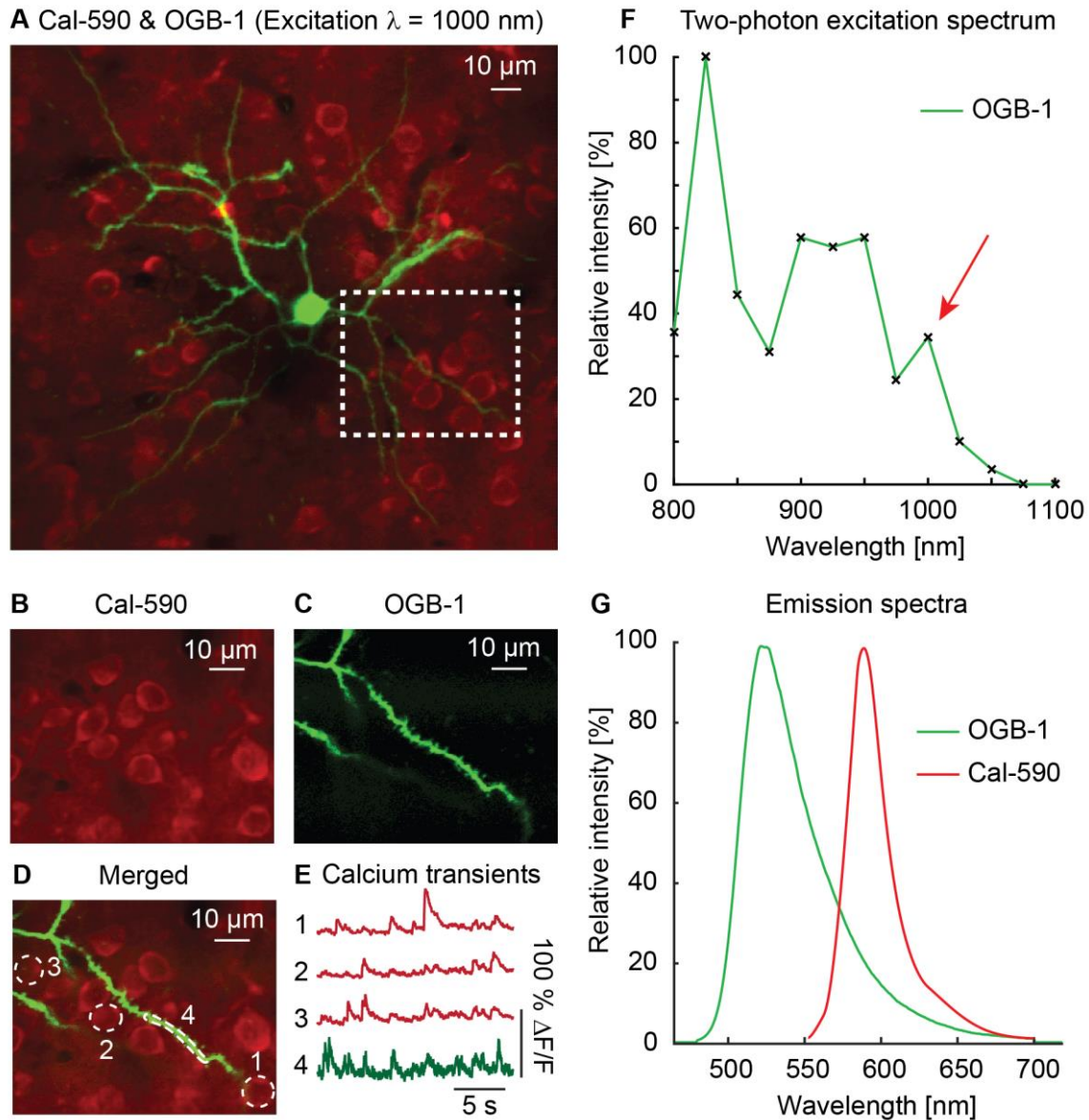
3.5.2.4 Dual-color imaging

The new red-shifted calcium indicator Cal-590 can in principle be combined with classical green-emitting calcium indicators, like OGB-1. Here, for example, cell populations were stained with Cal-590 AM and one of the cells in the field-of-view was counterstained with the

salt version of OGB-1 via electroporation. The cell population labeled with Cal-590 AM and the subcellular structures of the single-cell filled with OGB-1 were imaged sequentially by exciting both dyes at their optimal two-photon excitation wavelength (fig. 23) (Tischbirek *et al.*, 2015). The resulting fluorescence transients recorded from the cells filled with Cal-590 AM and the dendrites of a single-cell stained with OGB-1 were characterized by high SNR and no apparent cross-talk (Tischbirek *et al.*, 2015).
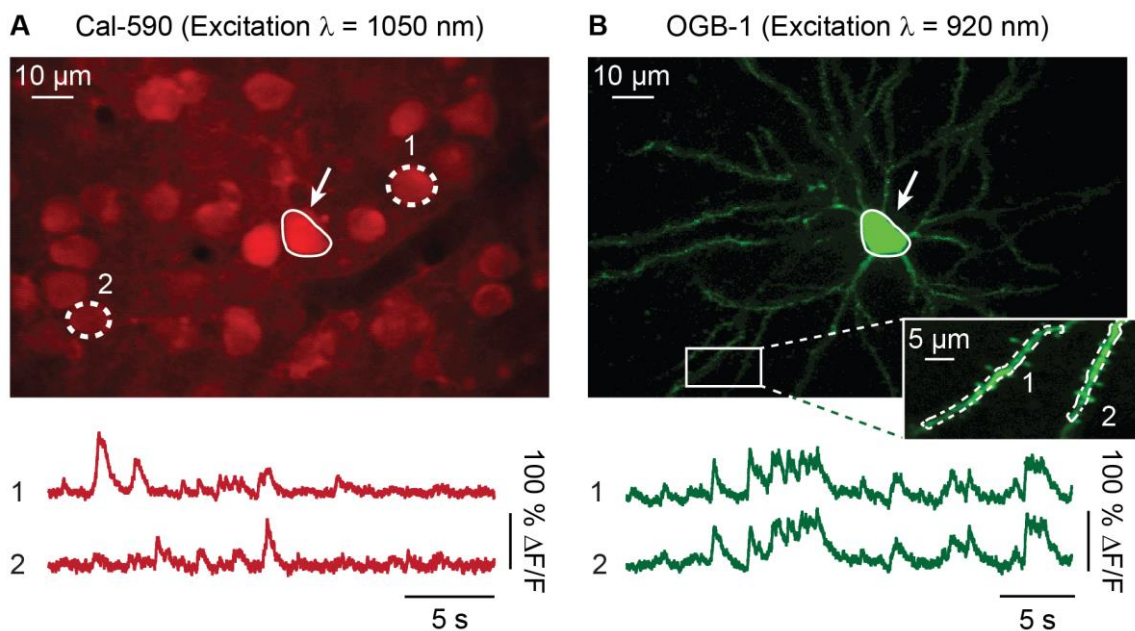
Fig. 23 *Dual-color calcium imaging with Cal-590 AM and OGB-1 in vivo.* **(A)** *Two-photon image of a cell population at a depth of 500 μm of the mouse visual cortex. The cells are filled with Cal-590 AM, which was excited at 1050 nm and recorded for 30 s at a frame rate of 80 Hz. Example transients of two cells, indicated with white-dotted lines, are shown below. The white arrow points to the neuron, chosen for single-cell electroporation with OGB-1.* **(B)** *Same field-of-view as in (A), but excited at 920 nm (30 s, 80 Hz frame rate). The cell here, electroporated with OGB-1, corresponds to the cell marked with a white arrow in (A). The inset image of the dendrites was obtained from an average projection of five focal planes, recorded in steps of 10 μm. The fluorescence transients correspond to spontaneous activity recorded from the two dendrites marked with white-dashed lines. They were recorded at a frame rate of 200 Hz. (Figure was adapted from (Tischbirek et al., 2015))*

When analyzing the two-photon excitation spectrum of OGB-1, an unexpected peak in fluorescence was found at 1000 nm (fig. 24 F). This peak offers the opportunity to excite both dyes at an intermediate excitation wavelength of 1000 nm simultaneously. The two spectra of emission light, shown in fig. 24 G, were separated at 565 nm with a dichroic mirror and recorded with two photodetectors. An example for simultaneous recording of Cal-590 AM and OGB-1 is displayed in fig. 24 A (Tischbirek *et al.*, 2015). Spontaneous activity was recorded from individual cells of the densely labeled cell population and from single dendrites of the single cell filled with OGB-1, both with good SNR (Tischbirek *et al.*, 2015). Optical filters were used to avoid bleed-through fluorescence (for Cal-590: bandpass 620/60 ET, AHF; for OGB-1: 550-nm short-pass filter, Edmund Optics). As a result there was no virtual overlap between the two channels (compare to fig. 24 B and C) (Tischbirek *et al.*, 2015).

A Cal-590 & OGB-1 (Excitation λ = 1000 nm)

10 µm

F Two-photon excitation spectrum

B Cal-590 — 10 µm

C OGB-1 — 10 µm

D Merged — 10 µm

E Calcium transients

100 % ΔF/F

5 s

G Emission spectra

Fig. 24 *Simultaneous recording of Cal-590 AM and OGB-1.* ***(A)*** *Overlay of two images excited at 1000 nm and recorded with two PMTs (green channel: fluorescence light collection between 425 nm and 650 nm; red channel: detection between 590 nm and 650 nm). The cells shown here were recorded in layer 2/3 of the mouse primary visual cortex in vivo.* ***(B)*** *and* ***(C)*** *Images of the area marked with white-dotted lines in (A). The two channels are displayed separately and merged in (D). Transients in (E) were obtained from the ROIs marked in (D). The red traces represent the recordings of the red channel (Cal-590 AM) and the green trace corresponds to a recording from the green channel (OGB-1).* ***(F)*** *Two-photon excitation spectrum, measured from 800 nm to 1100 nm. The red arrow depicts an excitation peak at 1000 nm.* ***(G)*** *Emission spectra of OGB-1 and Cal-590. Data was adapted from the information from the distributors of the calcium dyes provided online (ThermoFisher and AAT Bioquest). (Figure was adapted from (Tischbirek et al., 2015))*

3.6 Deep two-photon calcium imaging

So far, it was shown that the red-shifted calcium dye Cal-590 can be used for *in vivo* applications and that functional imaging with Cal-590 comes along with multiple advantages, such as rapid kinetics of the reported calcium transients. In combination with a local restriction of the dye application, it can be used for deep imaging experiments, as shown in the next sections.
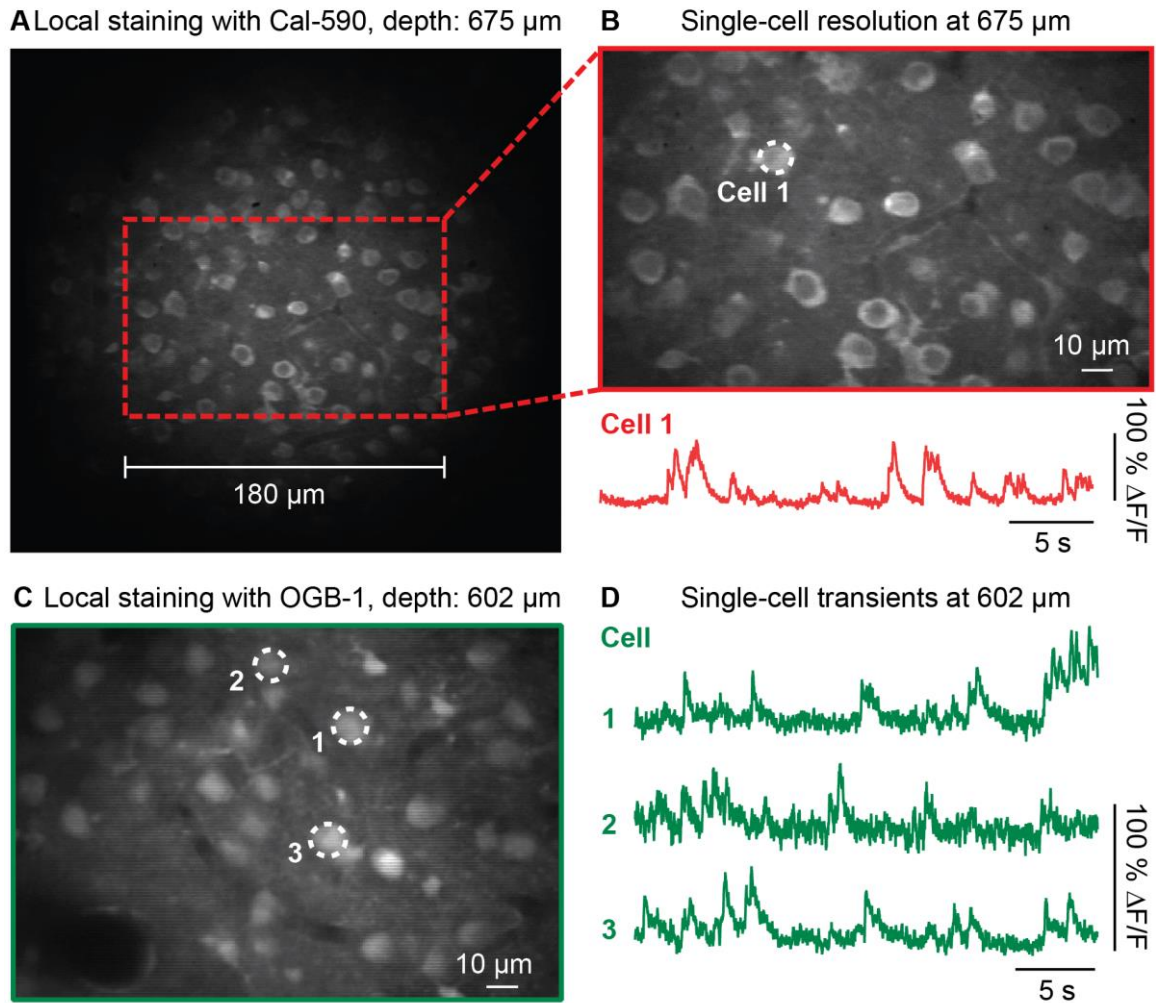
3.6.1 Minimization of fluorescent background by local dye application

To use the new red-shifted dye Cal-590 for deep two-photon imaging, the experiments need to follow the practical guide provided in section 3.4. Especially, the spatial restriction of the dye loading is of major importance for a successful experiment in deep cortical layers of the mouse brain *in vivo*. To demonstrate the effect of local versus global dye loading, a two-step experiment was performed. First, a small volume of cells at around 600 µm below the pial surface was loaded with Cal-590 AM under visual guidance. To visualize the pipette tip and the distribution of the dye during pressure-injection, Alexa Fluor 680 (10 µM) was added to the solution inside the loading pipette. The diameter of the staining was between 150 µm and 200 µm, resulting in field-of-view with about 30 cells, well-filled with dye (fig. 25 A) (Birkner *et al.*, 2017). As a result, an image of the labeled cells with high contrast was recorded at a depth of 610 µm below the cortical surface, whereas at a depth of 150 µm no fluorescence could be detected (fig. 25 B) (Birkner *et al.*, 2017). In the subsequent step Cal-590 AM was loaded into the tissue immediately above the recording site at 610 µm. The dye was applied with larger pressure to result in a more global staining, as it was usually done for multi-cell bolus loading (fig. 25 C). About 60 min after dye loading, the same location of the brain tissue was recorded again at 150 µm and 610 µm below the cortical surface with the same imaging parameters used before (fig. 25 D) (Birkner *et al.*, 2017). This time, high quality images were obtained from the superficial layer 2/3, but in the deep cell layer at 610 µm, the SNR was strongly deteriorated and single-cells are no longer distinguishable (fig. 25 D) (Birkner *et al.*, 2017). An increase in excitation laser power did not improve the SNR of the image at 610 µm, but only increased the overall brightness of the image. Thus, deep two-photon imaging is only feasible without or with minimal fluorescence background.
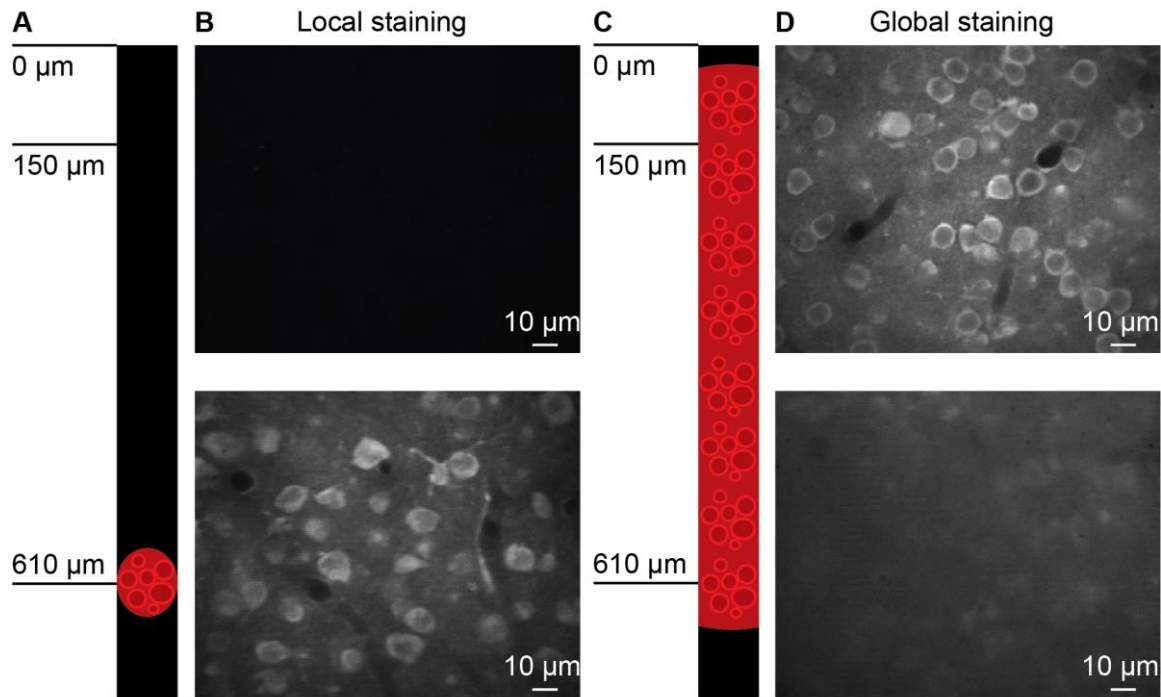
Fig. 25 *Comparison of local and global fluorescent calcium dye application. **(A)** Schematic side view of the mouse cortex, with cells labeled with Cal-590 AM indicated in red. **(B)** Two-photon images recorded at depths of 150 µm and 610 µm below the cortical surface (30 s, 80 Hz frame rate), in case of a local staining of cells around 610 µm. The average laser power measured under the objective lens was 8 mW for the superficial recording (upper image) and 38 mW for the recording from deep inside the mouse cortex (lower image). **(C)** Immediately after the recordings shown in (B) the upper cortical layers were globally stained with Cal-590 AM, as schematically shown here. **(D)** Same recording as in (B), but in case of a global staining with Cal-590 AM. The upper image was recorded at 150 µm below the mouse brain surface (30 s, 80 Hz frame rate, 8 mW average laser power) and the image below was obtained from a cortical depth of 610 µm (30 s, 80 Hz frame rate, 56 mW average laser power). (Figure was adapted from (Birkner et al., 2017))*

To further stress this point, a similar experiment was performed with the standard green-emitting dye OGB-1 AM. As demonstrated before, local staining of Cal-590, shown in fig. 26 A, allowed for recordings of spontaneous activity from single cells with high SNR at a depth of here 675 µm below the pial surface (fig. 26 C) (Birkner *et al.*, 2017). But even when using the classical green-emitting calcium dye OGB-1, the spatially restricted staining enabled imaging at depths around 600 µm with good quality and high SNR single-cell transients (fig. 26 C & D) (Birkner *et al.*, 2017).

A Local staining with Cal-590, depth: 675 µm

180 µm

B Single-cell resolution at 675 µm

Cell 1

10 µm

Cell 1

100 % ΔF/F

5 s

C Local staining with OGB-1, depth: 602 µm

10 µm

D Single-cell transients at 602 µm
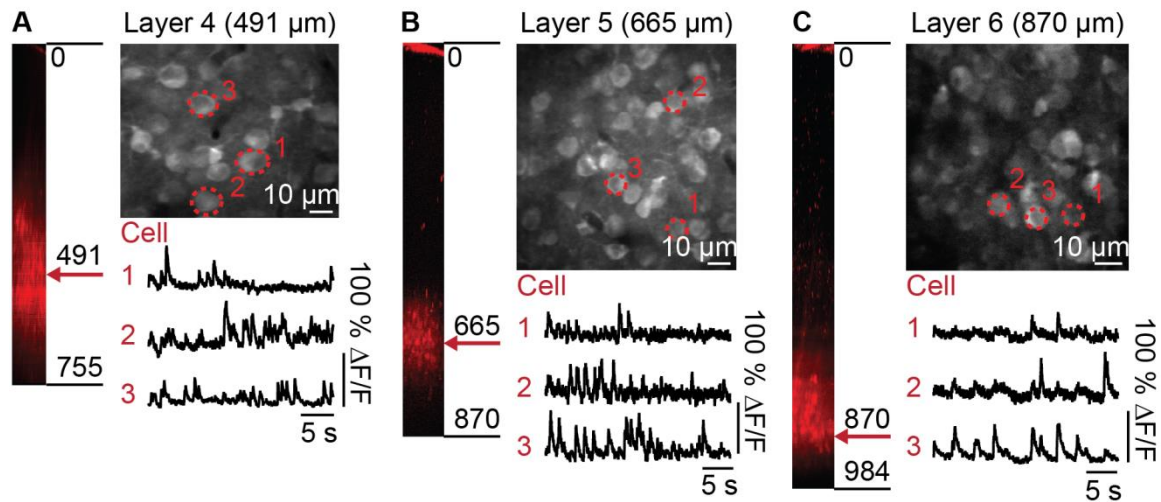
Cell

1

2

3

100 % ΔF/F

5 s

Fig. 26 *Spatially-restricted calcium dye application in vivo. **(A)** Overview of a cell population locally labeled with Cal-590 AM, at a depth of 675 µm below the pial surface of the mouse primary visual cortex in vivo (average of 30 s, 40 Hz framerate). **(B)** Average image of the field-of-view marked in (A) (30 s, 80 Hz framerate). The spontaneous activity shown below belongs to the cell marked with a white-dotted circle. **(C)** Average image of cells at a cortical depth of 620 µm in the mouse primary visual cortex in vivo (30 s, 80 Hz frame rate), labeled with OGB-1 AM. The dye application was spatially-restricted, as shown in (A). **(D)** Spontaneous activity of the cells marked in (C). (Figure was adapted from Birkner, Tischbirek et al., Cell Calcium, 2016)*

3.6.2 Imaging all cortical layers of the mouse primary visual cortex *in vivo*

To break the depth limit of two-photon calcium imaging, the two initial major ideas were combined: The reduction of scattering effects of the excitation wavelength with the red-shifted calcium dye Cal-590 AM and the avoidance of background fluorescence by local dye application. Cell populations were labeled in cortical layers 4 to 6 of the mouse primary visual cortex *in vivo* in distinct sets of experiments. For each labeling, single-cells were clearly resolved, even in the deepest cortical layer, layer 6, at around 900 µm below the brain surface (fig. 27) (Tischbirek *et al.*, 2015; Birkner *et al.*, 2017). Spontaneous activity was recorded from single cells in each cortical layer and with high SNR (fig. 27) (Tischbirek *et al.*, 2015). As reported in previous electrophysiological studies, layer 5 showed the highest spontaneous activity, compared to the other layers (de Kock *et al.*, 2007; Niell & Stryker, 2008). The combination with cell-attached recordings at a depth of 740 µm below the pial

surface showed that the sensitivity of the recordings was comparable to that obtained in upper cortical layers (fig. 28) (Tischbirek *et al.*, 2015).


Fig. 27 *Deep two-photon calcium imaging of dense cell populations with single-cell resolution in vivo. **(A)** Two-photon calcium imaging of layer 4 of the mouse primary visual cortex in vivo. The z-projection at the left side shows a side view of the cortex, with cells in layer 4 filled with Cal-590 AM. The two-photon image next to it is an averaged two-photon image of a cell population recorded at a cortical depth of 491 µm (30 s, 80 Hz frame rate). The transients below belong to the three cells marked with red-dotted circles and display spontaneous activity, recorded at 80 Hz. **(B)** Same as in (A) but the cells are labeled in layer 5 of the mouse visual cortex, recorded at a cortical depth of 665 µm in vivo. **(C)** Same arrangement as in (A) and (B). The cells were stained in layer 6 of the mouse primary visual cortex in vivo. The image and transients at the right side were obtained from an imaging depth of 870 µm (80 Hz frame rate). (Figure was adapted from (Tischbirek et al., 2015))*
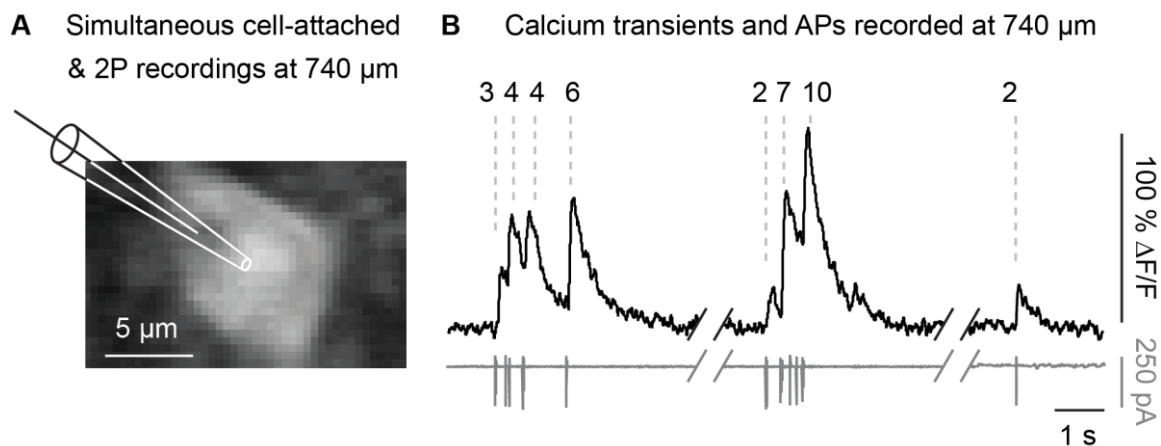

Fig. 28 *Quantification of fluorescence transients reported with Cal-590 AM at a depth of 740 µm below the cortical surface of the mouse in vivo. **(A)** Cell-attach recording from a cell filled with Cal-590 AM, 740 µm below the cortical surface. **(B)** The black transient represents the fluorescence trace recorded from the cell filled with Cal-590 AM. The grey trace below represents the action-potential activity of the cell, recorded simultaneously in the cell-attached mode. The number of action potentials measured with the cell-attach pipette are indicated above the calcium transient. Periods without spontaneous activity were excluded, marked with broken lines. (Figure was adapted from (Tischbirek et al., 2015))*

3.6.3 Layer 6 imaging in the awake behaving mouse

Two-photon calcium imaging in awake behaving mice, head-fixed under the microscope and running on a treadmill became very popular in the past couple of years (for example (Keller *et al.*, 2012; Fu *et al.*, 2014)). Usually these experiments are performed with genetically encoded calcium indicators, which are expressed chronically in specific cell populations. Whether stable recordings can be obtained from deep cortical layers and with acute staining procedures in awake behaving mice was unclear. Therefore, experiments on awake behaving mice were performed, as schematically shown in fig. 29. The mouse was running on a treadmill and the movements were recorded with an incremental encoder attached to the treadmills' axis. Drifting gratings were presented on a LCD screen to the contralateral eye of the mouse to elicit visually-evoked single-cell responses (fig. 29) (Birkner *et al.*, 2017). Figure 30 A gives an example for a recording of layer 6 at 860 µm below the pial surface of the primary visual cortex of the awake behaving mouse (Birkner *et al.*, 2017). The cell highlighted in the image was silent during quiescence and active during running periods (> 1 cm/s), which are indicated with orange bars below the fluorescence transients. The example in fig. 30 B shows a cell in layer 6 which responded strongly to the drifting grating presented on a screen. The largest response amplitudes were recorded during locomotion, representatively shown by the two recordings during quiescence and locomotion in fig. 30 B. This gain increase during locomotion was described before mainly for upper cortical layers (Niell & Stryker, 2010; Keller *et al.*, 2012; Bennett *et al.*, 2013; Polack *et al.*, 2013; Saleem *et al.*, 2013; Fu *et al.*, 2014; Reimer *et al.*, 2014; Pakan *et al.*, 2016; Dadarlat & Stryker, 2017).
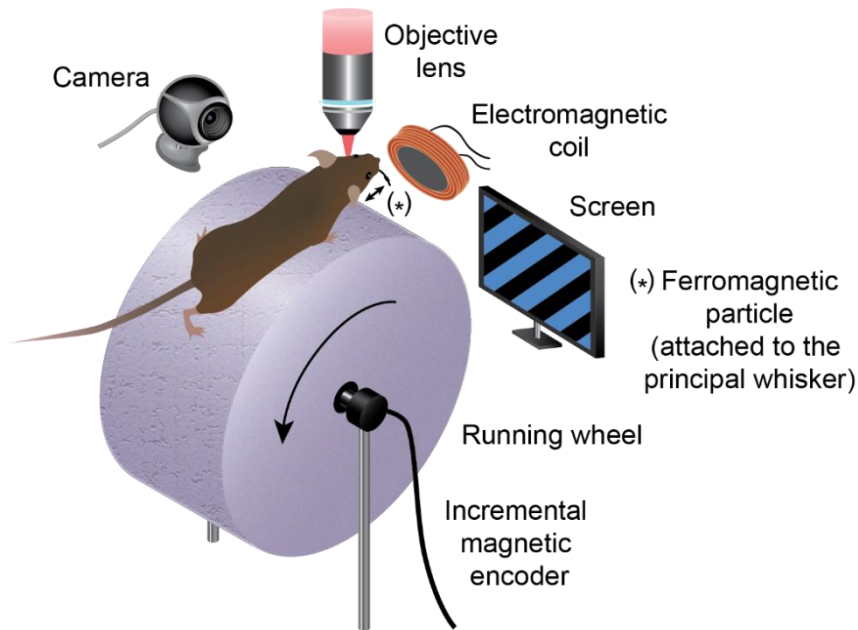
Fig. 29 *Scheme of the experimental setup for two-photon experiments with an awake behaving mouse. The mouse is head-fixed at the microscope but can freely run on a wheel-shaped treadmill with a diameter of 15 cm. The running speed is measured with an incremental magnetic encoder fixed to the central axis of the running wheel. All movements of the animal (including whisking) are observed during the experiment with a small webcam. The recordings were combined with sensory cues, such as visual stimulation with a screen placed in front of the mouse, or whisker stimulation with a magnetic coil and a small ferromagnetic particle glued to the mouse whisker.*
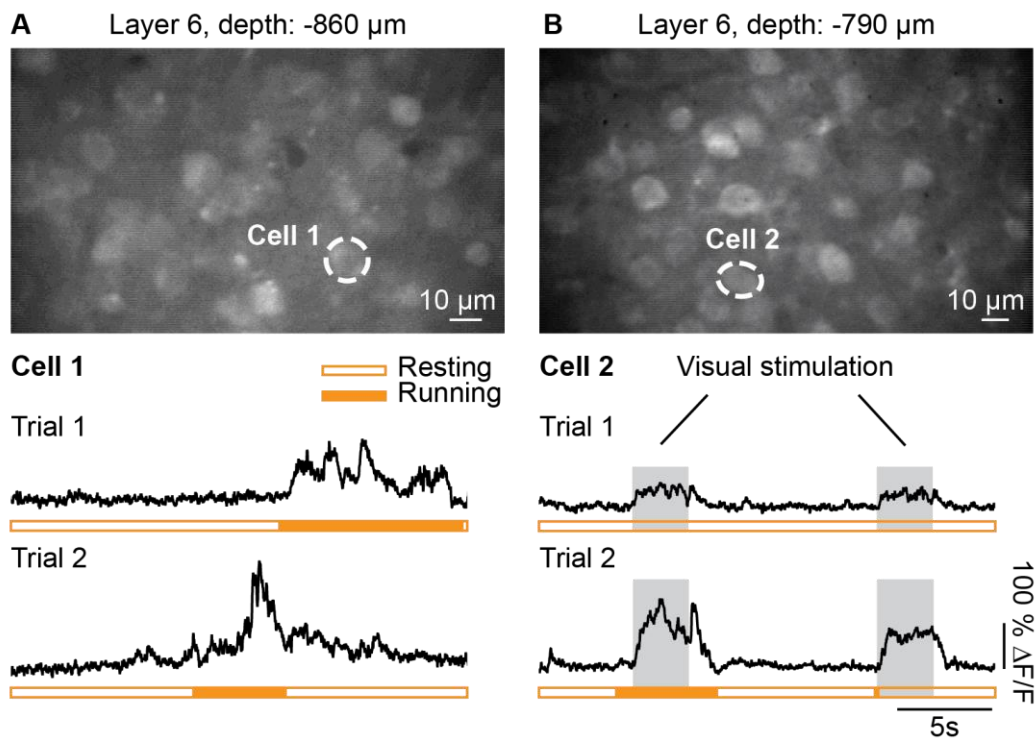
Fig. 30 *Two-photon calcium imaging of cortical layer 6 of the awake behaving mouse. **(A)** Average two-photon image, recorded at 860 µm below the cortical surface (30 s, 80 Hz frame rate). Below: Example calcium transients of the cell marked in white. This particular cell was active during locomotion (> 1 cm/s), which is indicated with filled orange bars below the calcium transients. **(B)** Second example of layer 6 imaging in the cortex of an awake behaving mouse (average of 30 s, 80 Hz). Calcium transients of the cell marked with a white-dotted line are displayed below. Grey bars represent periods of visual stimulation. Locomotion is marked with orange bars. Responses to the visual stimuli were the largest during periods of locomotion. (Figure was adapted from (Tischbirek et al., 2015))*

3.7 Anatomy-function relationship in layer 5 of the mouse barrel cortex

The new deep two-photon calcium imaging method developed in this work finally allows for functional recordings of dense cell populations in layer 5 of the awake behaving mouse with single-cell resolution. The target region for these recordings was the barrel cortex, as it is a widely used model system to study cortical processing of sensory inputs (Petersen, 2007; Feldmeyer, 2012; Feldmeyer *et al.*, 2013). Individual cells were chosen based on their functional properties and targeted for the analysis of single-cell morphologies and subcellular activity.

3.7.1 Targeted imaging of specific barrel fields in cortical layer 5 of the awake behaving mouse

Before each deep two-photon imaging experiment the barrel fields of the mouse cortex were mapped with transcranial widefield flavoprotein imaging, to assign the two-photon imaging field-of-view to a certain principal whisker (fig. 31 A). A craniotomy above the barrel fields was performed and the mouse was transferred to the two-photon microscope and head-fixed with an implant attached to its skull. A cortical region was identified, which is more or less free of superficial blood vessels and which is located in the center of one of the mapped barrel fields. Exactly below that spot at the cortical surface, layer 5 cells were loaded with the fluorescence calcium indicator Cal-590 AM by visually-guided local dye application (Tischbirek *et al.*, 2015; Birkner *et al.*, 2017). To ensure that the dye is ejected at the correct location, the entrance point of the loading pipette at the brain surface, the angle of pipette and the distance to travel into the tissue were determined before dye loading (fig. 31 B). The depth of cell labeling was around 800 µm below the cortical surface, corresponding to the center of layer 5 of the C2 barrel field of the mouse (Lefort *et al.*, 2009). The final location of the pipette tip, in relation to the blood vessel pattern and in depth, was always double-checked before dye application. It should be noted that the mouse barrel cortex is thicker compared to other cortical areas, like for example the primary visual cortex (compare to Allen Institute Atlas (Allen Institute for Brain Science) and (Lefort *et al.*, 2009; Xu *et al.*, 2016)).

Once the dye was ejected, all but the principal whisker were trimmed and a small ferromagnetic particle (< 0.5 mm) was glued to this specific whisker. Afterwards, the isoflurane anesthesia of the mouse was switched off and the mouse was placed on a running wheel (as schematically shown in fig. 29). Movements of the mouse were detected with an incremental magnetic encoder, fixed to the axis of the running wheel and active whisking was captured with a small webcam. 30 to 45 minutes after switching off the isoflurane, the mouse was fully awake, running on the wheel or grooming and the fluorescent calcium dye was uptaken by the cells in layer 5.
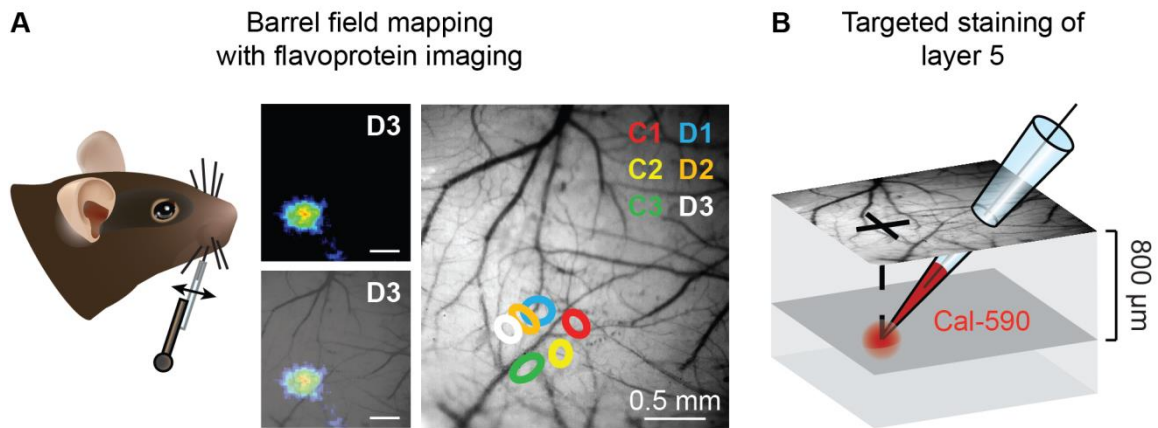
Fig. 31 *Targeted staining of a specific barrel field in layer 5 with Cal-590 AM.* **(A)** *Flavoprotein imaging to map the barrel fields. Left: Schematic display of the whisker stimulation. Single whiskers were placed inside a glass capillary which is connected to a piezoelectric actuator. Whisker by whisker was deflected for 1 s and at a frequency of 10 Hz. Right: Example for flavoprotein imaging during whisker stimulation. The upper left color-coded image shows an average autofluorescence image corresponding to 20 trials of deflecting the whisker D3. The figure below shows a merged image of the skull surface and the averaged autofluorescence image. To generate the barrel field map at the right side of the figure, six whiskers (C1 - C3 and D1 - D3) were stimulated consecutively. The scale bars represent 0.5 mm.* **(B)** *Schematic illustration of the targeted staining procedure. The entrance side of the pipette tip was calculated beforehand to reach the correct position at the targeted cortical depth. The dye (Cal-590 AM) was pressure ejected under visual guidance, until a volume with a diameter of about 150 - 200 µm was filled with fluorescence.*

3.7.2 'Super-responding' (SR) neurons in layer 5 of the awake behaving mouse

An example for two-photon calcium imaging of barrel cortex layer 5 in the awake behaving mouse is shown in fig. 32 A. The principal whisker was deflected by applying current to the magnetic coil (1 s, 10 Hz), whenever the mouse was sitting still and did not actively whisk. Otherwise, locomotion and active movements of the vibrissae would lead to diverse motor-related inputs to the barrel cortex and thus to a more complex situation. In addition, recordings from the quiet awake mouse can be well compared to those obtained from the slightly anesthetized animal, as performed in later experiments. Surprisingly, most of the cells recorded in the awake mouse showed only weak or no sensory-evoked activity, even though layer 5 pyramidal neurons are known to be the most active neurons of the cortex (de Kock & Sakmann, 2008; O'Connor *et al.*, 2010). The distribution of cellular response strengths, defined as the average response amplitude across all trials of sensory stimulation (at least 9), is displayed in fig. 32 B. The resulting histogram steeply declines towards weakly- or non-responding neurons. In accordance to other studies, which analyzed upper cortical layers with two-photon imaging or layer 5 cells with cell-attached recordings, about 10% of all cells (11 of 116 cells, recorded from 3 mice) were responsible for 50% of the sensory-evoked activity (Hromadka *et al.*, 2008; O'Connor *et al.*, 2010). Of these 10% a small subset of neurons responded with large fluorescence transients with amplitudes larger than 30% $\Delta F/F$ and with a high response reliability of more than 80% (fig. 32 D). Here, these neurons are called 'super-responding' (SR) neurons, which make up 4% ± 2% (5 out of 116 cells; average ± SEM) of all layer 5 neurons recorded in the awake animal. A representative

example for a SR neuron is provided in fig. 32 C. This cell was recorded from an awake behaving mouse, which was subsequently slightly anesthetized and the same field-of-view was imaged again. For anesthesia, the animal was sedated with Chlorprothixene (4.5 mg/kg KG) to be able keep the isoflurane at low concentrations of 0.25% - 0.5% in oxygen, because previous studies showed that general anesthesia can influence sensory-evoked cortical activity (Haider *et al.*, 2013; Durand *et al.*, 2016). The super-responding cells identified under awake conditions showed highly similar response profiles to principal whisker stimulation under this low level of anesthesia, as displayed in fig. 32 E. There is no significant difference between the response strength or the response probability of the SR cells under the two states (Wilcoxon signed rank test: $p = 0.06$ (response strength) and $p = 0.50$ (response probability)). The correlation between responses of SR neurons under anesthesia and in the awake animal is very high, with a correlation coefficient of $p = 0.9937$, whereas the responses of the rest of the neurons showed much weaker correlation between the two recording sessions (Pearson's correlation coefficient: $p = 0.5306$).
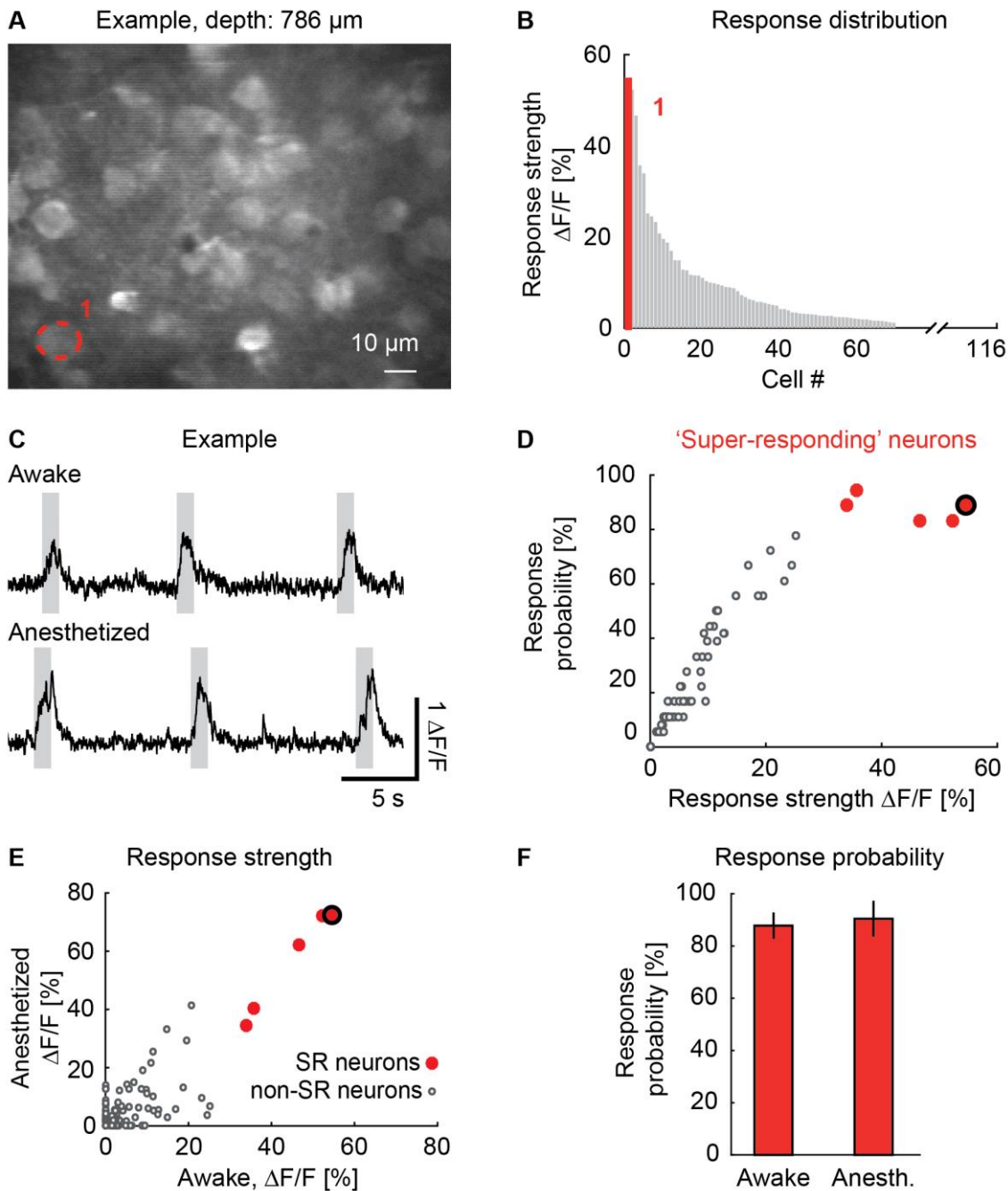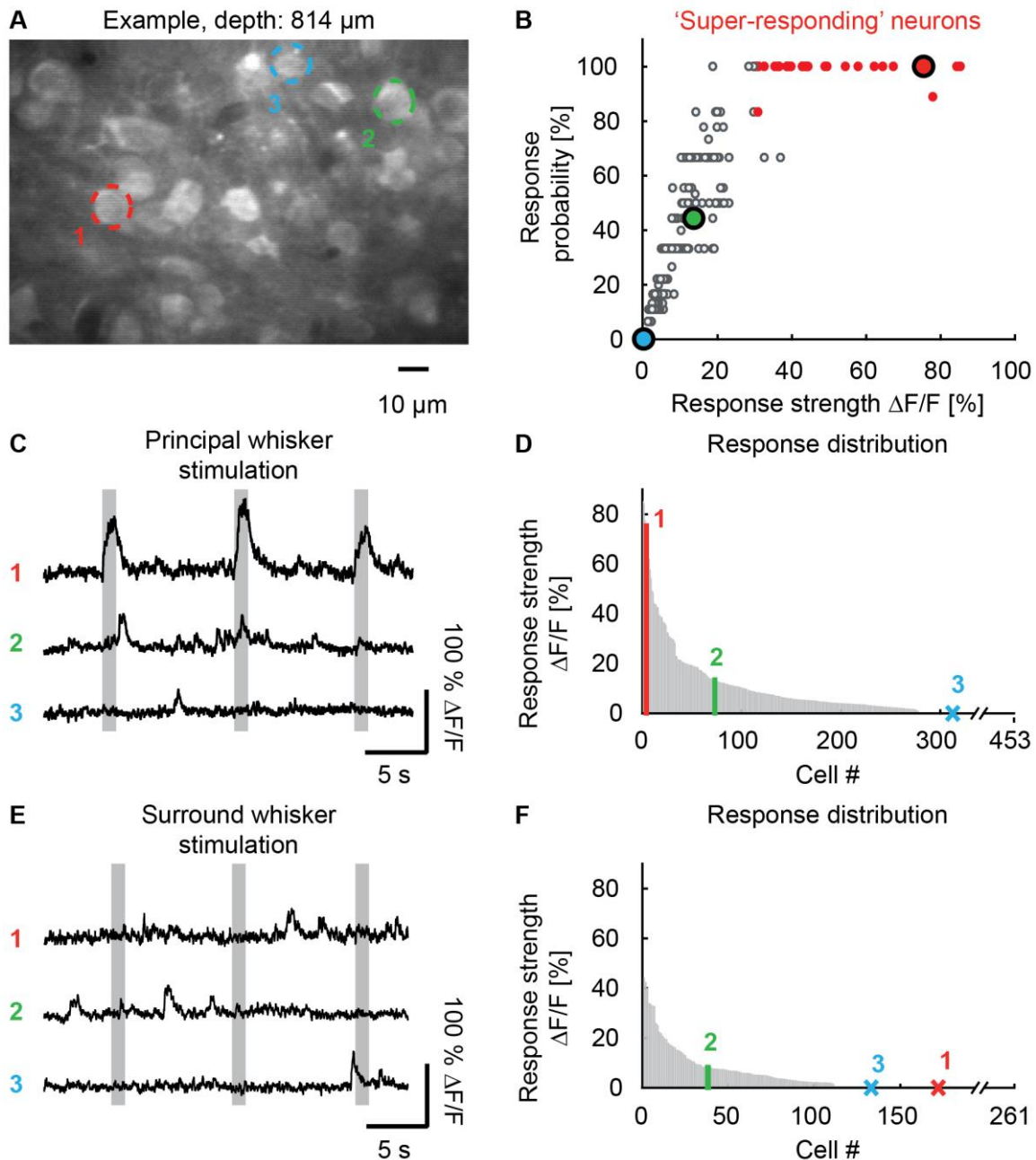
Fig. 32 *Skewed distribution of single-cell sensory-evoked responses in layer 5 of the barrel cortex of the awake behaving mouse. (A) Two-photon image of layer 5 cells in the barrel cortex of the awake behaving mouse (30 s, 80 Hz frame rate). The cells were recorded from a cortical depth of 786 µm and labeled with Cal-590 AM. The cell marked with a red-dotted circle was identified as 'super-responding' (SR) neuron. (B) Distribution of single-cell response strength to principal whisker stimulation (3 mice, 116 cells, 5 SR neurons). The response strength here is defined by the average response amplitude which is plotted cell by cell. The red bar highlights the SR neuron marked in (A). (C) Example calcium transients of the SR neuron indicated in (A) recorded in the awake behaving mouse (upper transient) and in the slightly anesthetized mouse (lower transient). Periods of principal whisker stimulation (1 s at 10 Hz) are displayed with grey bars. (D) Graphical display of the definition of SR neurons. The response probability of each cell is plotted against the response strength. Neurons with an average response amplitude larger than 30% and a response probability higher than 80% are marked in red and were defined as SR neurons (5 out of 116, recorded in 3 mice). The cell marked in (A) is encircled with a black line. (E) Comparison of sensory-evoked responses under anesthetized or awake conditions. The response strengths are plotted cell by cell for measurements in the anesthetized mouse or awake behaving mouse. The SR neurons are marked in red (5 out of 116 cells, 3 mice) and the cell shown in (A) is highlighted with a black circle. (F) Comparison of response probability of SR neurons under anesthesia or in the awake behaving state. There was no significant difference between the two cortical states (mean ± SD: 88.8% ± 4.6% (awake); 90.4% ± 6.5% (anesthetized); Wilcoxon signed-rank test: p = 0.50)*

3.7.3 Single-cell response distributions under light anesthesia

The experiments described above were repeated with animals sedated with Chlorprothixene (4.5 mg/kg) and slightly anesthetized isoflurane (0.25% - 0.5% in O_2), for experiments under a more controlled situation. Under this condition, there are no changes in attention of the animal, effecting the gain of sensory-evoked cortical activity (see for example (Niell & Stryker, 2010)) and no active movements, leading to diverse motor signal inputs to the barrel cortex (Mao *et al.*, 2011; Xu *et al.*, 2012). Moreover, imaging experiments can be combined with local pharmacological manipulations of the cells of interest and with electrophysiological measurements.

Before each experiment, the barrel fields were mapped with flavoprotein imaging, as described before. Subsequently, layer 5 neurons were stained and sensory-evoked single cell responses were recorded with two-photon calcium imaging (fig. 33 A). For these experiments, the individual whiskers were deflected with a glass capillary attached to a piezoelectric actuator, as during widefield flavoprotein imaging. The single-cell responses to principal whisker deflection are distributed similarly, compared to the awake situation (fig. 33 B and D). Again, about 10% of the cells (43 out of 453, recorded from 17 mice) fire half of the sensory-evoked activity and only few neurons (6% ±1% average ± SEM; 28 out of 453) respond with a probability larger than 80% and with large response amplitudes of at least 30% on average (fig. 33 B). Most of the neurons respond weakly or do not show any response. Example transients for a SR neuron, a weakly-responding and a non-responding neuron are provided in fig. xy C. Weakly-responding cells are defined here as cells showing at least one response to the stimulation across six or more trials. Non-responding neurons never show any sensory-evoked activity. The responses were in general lower when stimulating one of the neighboring whiskers of the same whisker row (fig. 33 E and F) as expected from previous studies on receptive field properties of layer 5 neurons. The skewed distribution of cellular responses is preserved for surround whisker stimulation (fig 33 F).

Fig. 33 *Skewed distribution of single-cell sensory-evoked responses in layer 5 of the barrel cortex of the slightly anesthetized mouse.* **(A)** *Average image of layer 5 cells at a cortical depth of 814 µm, labeled with Cal-590 AM (30 s, 80 Hz frame rate). The colored circles mark a SR neuron (red; response amplitude > 30 % and response reliability > 80 %), a weakly-responding (green; at least one response across six or more trials) and a non-responding neuron (blue; no response).* **(B)** *Response probability of each cell plotted against their response strengths. Super-responding cells, defined by a response strength larger than 30% and a response probability of more than 80%, are marked in red (28 SR neurons, out of 453, recorded in 16 mice). The three cells encircled in (A) are highlighted with a blue, green or red dot, encircled with a black line.* **(C)** *Example calcium transients of the three cells marked in (A). The grey bars indicate principal whisker stimulation (1 s at 10 Hz). Cell number 1 represents a SR neuron, whereas cell 2 is hardly responding to the stimulation and cell 3 only shows spontaneous activity.* **(D)** *Distribution of the sensory-evoked responses to principal whisker stimulation, plotted cell by cell (453 cells recorded from 16 mice). The cells marked in (A) are highlighted with corresponding colors.* **(E)** *Same as in (C) but the grey bars represent the stimulation of the surround whisker, which was immediately adjacent to the principal whisker and in the same whisker row.* **(F)** *Same as in (D) but with stimulation of the surround whiskers which were in the same row as the principal whisker and located directly next to the principal whisker (261 cells recorded from 14 mice). The cells marked in (A) are shown with corresponding colors and numbers.*

3.7.4 Dual-color imaging to reveal common properties of SR neurons

Why are 5% of the neurons strongly activated by a certain stimulus and the rest of the population remains almost silent? Do these SR neurons have a common morphology, distinct from the other cells? Or is it a similar subcellular activation causing the high SNR of the sensory-evoked somatic responses? To shine light on these questions, SR neurons were identified within dense cell populations labeled with Cal-590 AM (fig. 34 A) and subsequently targeted with single-cell electroporation of OGB-1 (fig. 34 B). Therefore, the electroporation pipette was filled with the salt version of the calcium indicator OGB-1 (4.5 mM), which is spectrally distinct compared to Cal-590. Additionally, Alexa Fluor 680 (150 µM) was added to the solution to be able to visualize simultaneously the pipette tip and the cell population labeled with Cal-590 AM with a two-photon excitation wavelength of about 1050 nm. While approaching the labeled cells in layer 5 with the electroporation pipette, the principal whisker was stimulated regularly to clearly identify the activated SR neuron. Once the pipette was navigated through the upper cortical layers and positioned close to the cell's membrane, two current pulses were applied (270 nA, 30 ms each) to load the cell with the dye. After waiting 50 min for the diffusion of the dye inside the cell the apical dendrites of the SR neuron were imaged under two-photon excitation at 920 nm (fig. 34 B). This allowed for the reconstruction of the dendritic tufts of the SR neurons and the functional analysis of the dendritic tufts in layer 1 during sensory stimulation (fig. 34 B).
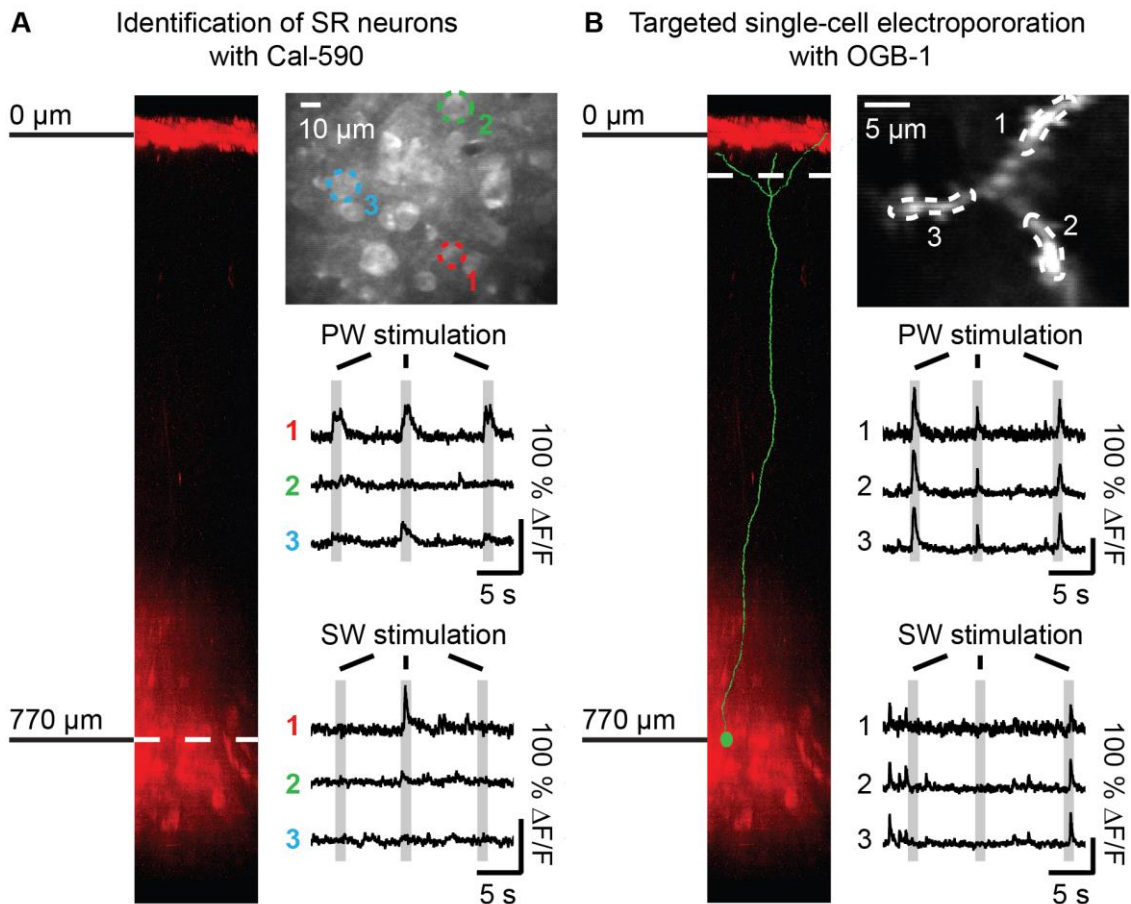
Fig. 34 *Targeted single-cell electroporation for dual-color imaging. **(A)** Example for the identification of a SR neuron with deep two-photon calcium imaging of a cell population labeled with Cal-590 AM. The vertical picture at the left side shows a z-projection of the recording. The cortical surface corresponds to 0 μm and the imaging depth was 770 μm, as indicated with a white-dashed line. The cell population recorded from this depth is displayed next to the projection (30 s, 80 Hz frame rate). The recorded field-of-view is shown with a two-photon image next to the z-stack. The cell marked with a red-dotted circle was identified as SR neuron, whereas the blue and green cells did not or barely respond to principal whisker (PW) deflection, as shown with example transients, displayed below. The grey bars represent periods of sensory stimulation. The calcium transients below represent recordings with surround whisker (SR) stimulation. **(B)** Electroporation of the cell marked with a red-dotted circle in the two-photon image in (A) with OGB-1. The cell was partially reconstructed from a z-stack, recorded with an excitation wavelength of 920 nm, and displayed in green. The recording site here was in layer 1, as indicated with a white-dashed line in the z-projection. The two-photon image shows an average of the tuft dendrites, recorded with 920 nm (30 s, 200 Hz frame rate). The three tuft dendrites were recorded during principal and surround whisker stimulation (PW and SW), as shown in the examples below.*

3.7.5 Slender-tufted morphology of SR neurons

The tuft-dendrites of 19 SR neurons were reconstructed from z-stacks of the electroporated cells. 18 of these neurons were identified to be slender-tufted layer 5 pyramidal neurons, with a somata depth of 796 μm ± 20 μm, a main bifurcation at 147 μm ± 61 μm, with 5 tuft dendrites on average and spanning an area with a maximal diameter of 136 μm ± 47 μm parallel to the pial surface (fig. 35 A) (compare to (Groh *et al.*, 2010)). Only one of the neurons showed a thick-tufted cell morphology, with a large dendritic tree consisting of 18 tuft branches and spanning 209 μm and a deeply located main bifurcation at 355 μm. The depth of the cell bodies was verified by imaging the cell's location in the sliced and fixed brain under a confocal microscope. To mark the neuron for confocal imaging, biocytin was

added in the electroporation pipette and the brain sample was postprocessed with immunohistochemistry by help of my colleagues Zsuzsanna Varga and Valérie Bonfardin (see methods). The depths of the somata were compared to the overall size of the cortex of the corresponding slice (from the pial surface to the white matter), to obtain a measure of depth independent of tissue shrinkage. On average the cells were located at 59% ± 6% of the cortex corresponding to the center of layer 5 and in between layer 5A and layer 5B (compare to Allen Institute Atlas (Allen Institute for Brain Science) and (Lefort *et al.*, 2009)). The axonal arbors of two of the cells were reconstructed by my colleague Zsuzsanna Varga. These cells show strong axonal innervation of upper cortical layers, up to L1, with highest density in supragranular layers and they are not restricted to one barrel column, but innervate horizontally neighboring barrel fields (fig. 35 B). This axonal structure is typical for slender-tufted layer 5 pyramidal neurons (Oberlaender *et al.*, 2011), which generally have additional callosal projections to the contralateral cortex, intracortical projections to, for example, M1 and S2 and projections to the striatum (Hattox & Nelson, 2007). The two cells reconstructed here match this projection pattern. One of the cells has an axonal branch into the ipsilateral striatum and the other one into the ipsilateral M1 (data not shown). In conclusion, the identified SR neurons can be assigned to the group of slender-tufted layer 5 pyramidal neurons.
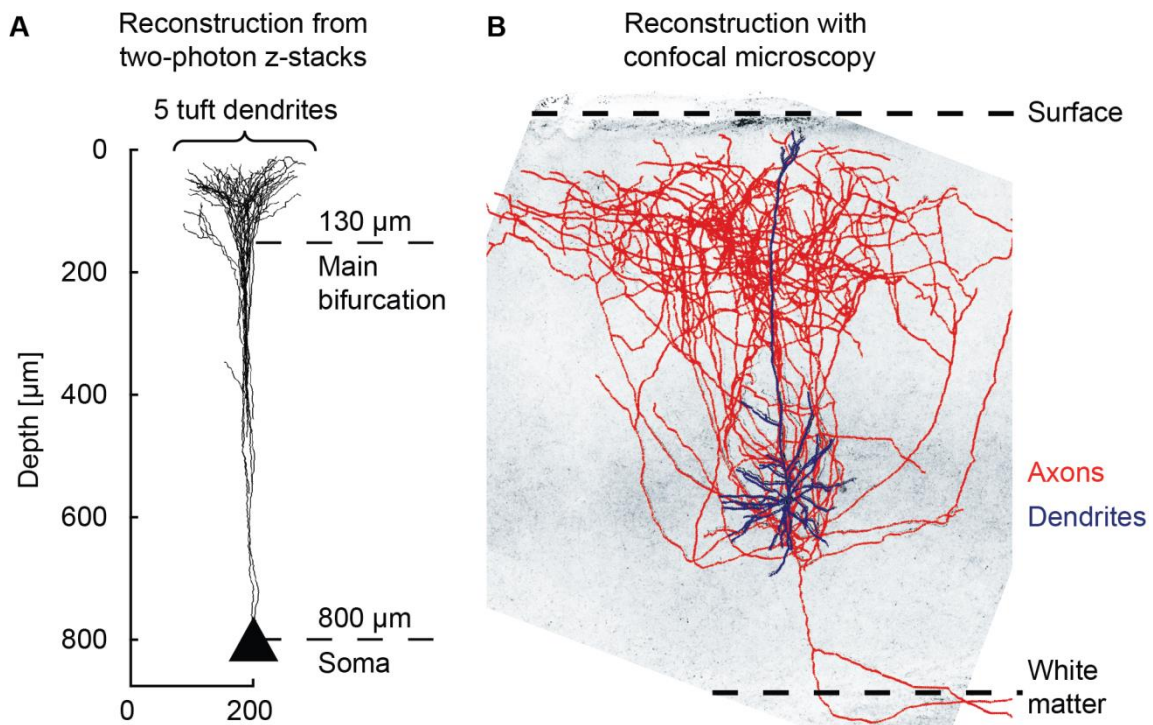
Fig. 35 *Single-cell morphology of SR neurons* **(A)** *Reconstructions of tuft dendrites from two-photon z-stacks (n = 16 cells). The average number of tuft dendrites, the average depth of the main bifurcation of the tuft dendritic tree and the average depth of the somata are indicated in numbers.* **(B)** *Axonal reconstruction of a SR neuron. The axons are displayed in red, the dendrites in blue.*

3.7.6 Calcium spikes in apical dendrites of SR neurons

The single-cell electroporation of the SR neurons can not only be used for morphological reconstructions, but particularly for functional analysis of the apical tuft dendrites. With two-photon excitation of OGB-1 at 920 nm, the tuft dendrites in layer 1 were imaged during sensory stimulation. Surprisingly, the stimulation induced large dendritic calcium events, which were uniformly distributed over the entire dendritic tree in layer 1 (fig 36 A and B). The signal amplitude of these events was the largest at the main bifurcation point of the apical dendrite and decreased with each branching point towards the surface (fig. 36 C). The large signal amplitudes, the spatial extend of these events and their maximum at the main bifurcation, indicate that these signals are dendritic calcium spikes. To validate the synaptic origin of these dendritic events, glutamatergic inputs were blocked and image sequences of the dendrites were acquired before and after blockage. Therefore, sensory-evoked dendritic spikes were recorded close to the main bifurcation, while a patch-pipette pipette was placed close to a more distal dendrite of the neuron in layer 1 (fig. 36 D). The solution inside the patch-pipette contained the NMDA-receptor blocker d(-)-2-amino-5-phosphonovaleric acid (AP5) and the AMPA-receptor blocker 6-cyano-7-nitroquinoxaline-2,3-dione (CNQX) (100 µM each) and an extremely low concentration of Alexa Fluor 594 (5 µM), to visualize the position of the pipette tip. The tuft dendrite close to the main bifurcation was imaged before and after gentle pressure ejection of the solution from the pipette. CNQX and AP5 blocked the strong sensory responses in the tuft dendrite, which recovered after a short waiting time of a couple of minutes (fig. 36 E and F; Wilcoxon signed rank test, $p = 0.028$; $n = 6$). Thus, the dendritic calcium spikes must be at least partially induced by synaptic inputs to the tuft dendrites.
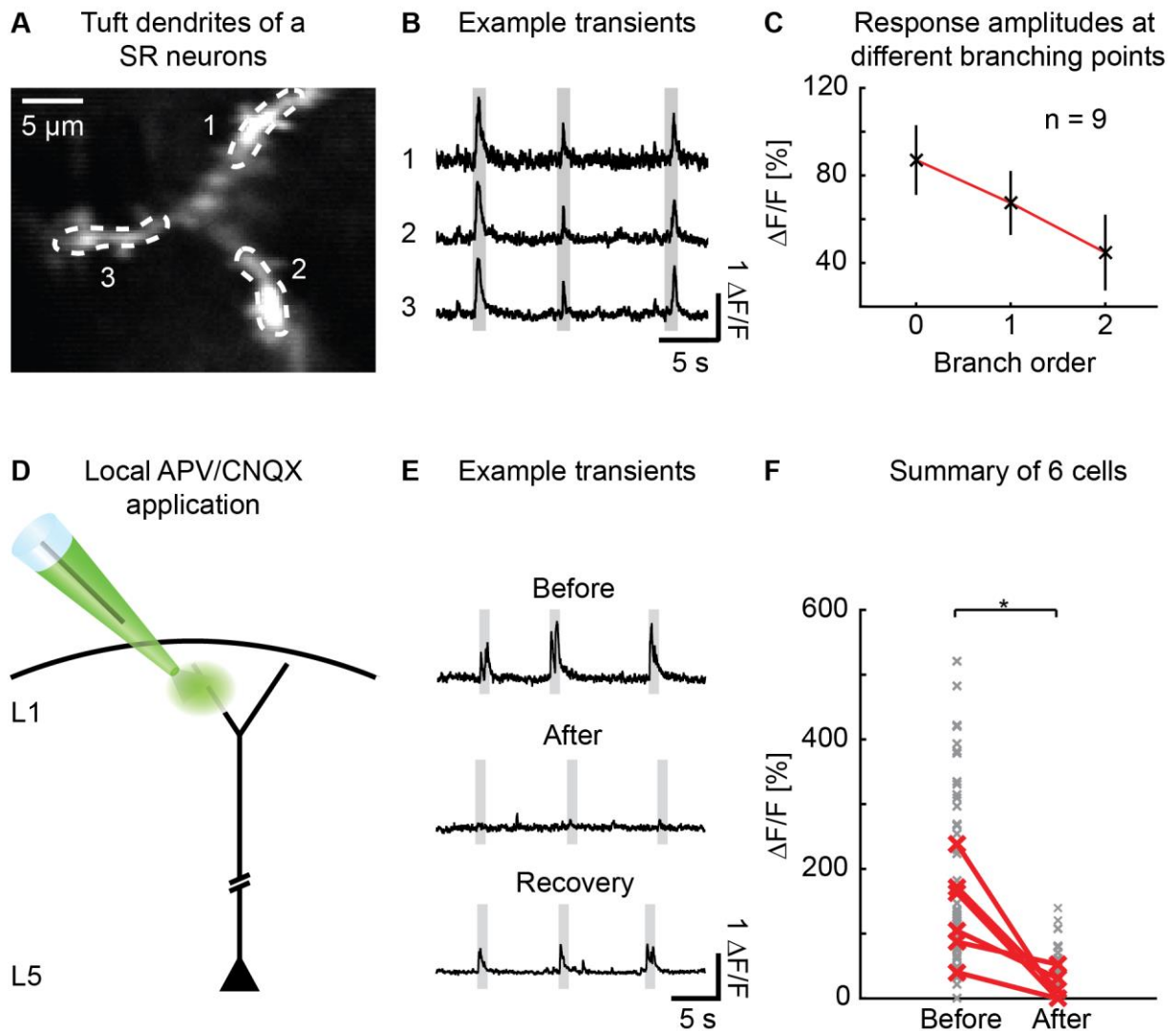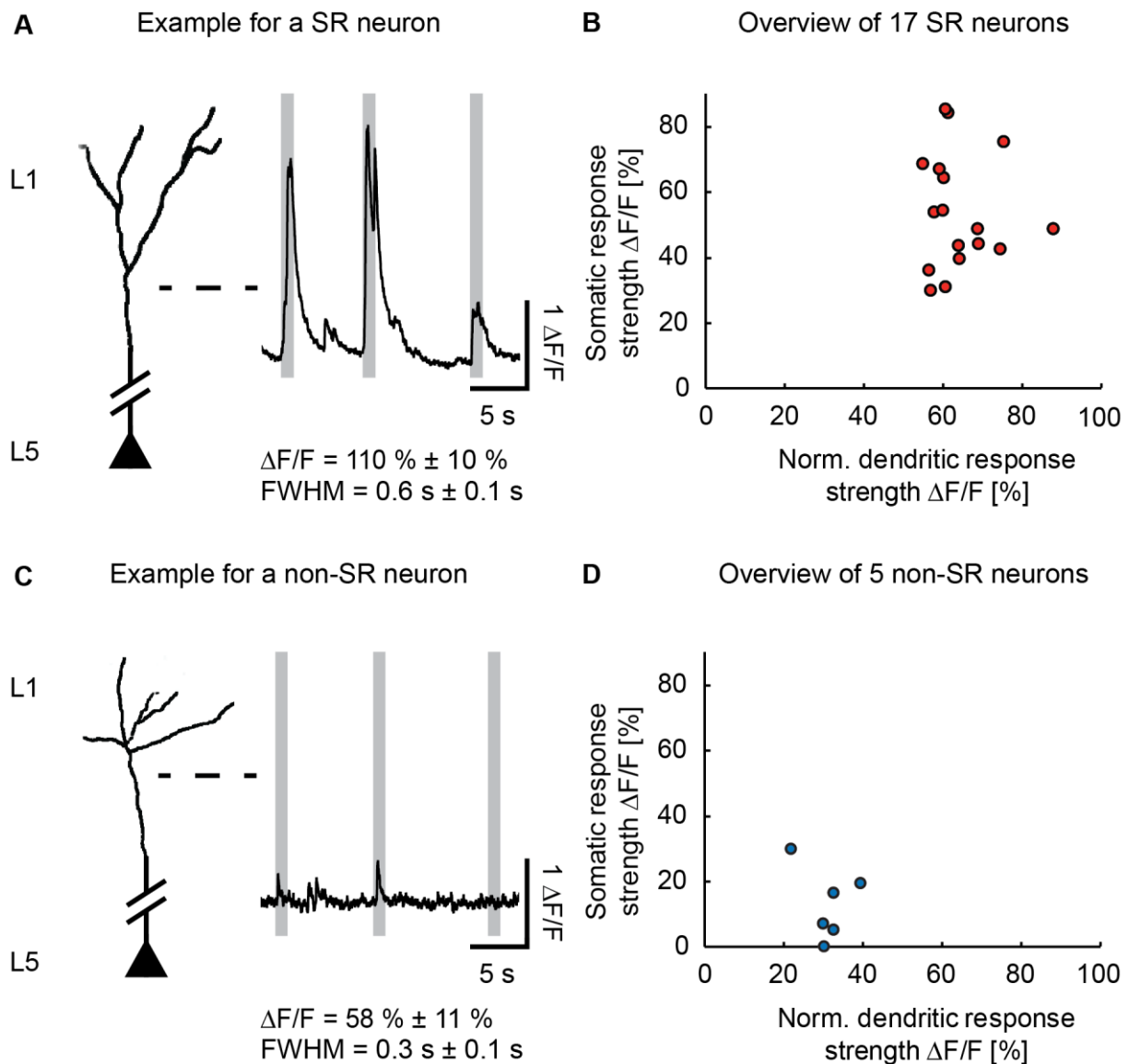
Fig. 36 *Synaptic origin of dendritic calcium spikes. **(A)** On-top view of tuft dendrites of a slender-tufted layer 5 neuron with super-responding characteristics. The two-photon image was recorded at 66 µm below the pial surface corresponding to cortical layer 1 (30 s, 200 Hz frame rate). **(B)** Example calcium transients of the dendrites shown in (A). The grey bars indicate periods of principal whisker deflection (1 s, 10 Hz). **(C)** Average response amplitudes of 9 cells, recorded in 9 mice, at three branching points (mean of the mean single-cell response amplitudes ± SEM). Zero corresponds to the main bifurcation of the tuft dendrites, one is above the first branching point towards the surface and two the second. **(D)** Scheme of the local application of APV/CNQX (100 µM each) to the tuft dendrites in layer 1. **(E)** Example for dendritic tuft responses before and after local application of APV/CNQX. The lowest transient shows an example for the recovery of the responses after a couple of minutes. **(F)** Summary of the dendritic responses before and after local application of APV/CNQX. The grey crosses represent single trial response amplitudes, whereas the red crosses show the average amplitudes of each cell (Wilcoxon signed rank test, p = 0.028; n = 6).*

3.7.7 Sensory-evoked dendritic calcium spikes as a unique property of SR neurons

Whether the sensory-evoked signals in the tuft are a unique property of SR neurons was unclear. Hence, weakly- or non-responding neurons were electroporated as well with OGB-1 to measure tuft activity from these cells during principal whisker deflection. Indeed, these cells did not show strong tuft activation triggered by sensory stimuli, as seen in SR neurons. If sensory stimulation induced a signal in the tuft, then with a small amplitude of 58% ± 11% and a temporal width of 0.3 s ± 0.1 s (fig. 37 C). In comparison, each of the SR neurons showed sensory-evoked dendritic spiking with an average amplitude of 110% ± 10% ΔF/F

and a temporal full-width-at-half-maximum of 0.6 s ± 0.1 s (fig. 37 A). To compare somatic with dendritic responses of both groups of cells, the response strength of the two compartments was displayed graphically for all electroporated cells (fig. 37 B and D). From this plot it seems that the somatic response strength is correlated to the dendritic one. In conclusion, only SR neurons fired large dendritic events in response to principal whisker stimulation, which clearly discriminates them from the rest of the layer 5 cell population.


A Example for a SR neuron

L1

L5

ΔF/F = 110 % ± 10 %
FWHM = 0.6 s ± 0.1 s

B Overview of 17 SR neurons

C Example for a non-SR neuron

L1

L5

ΔF/F = 58 % ± 11 %
FWHM = 0.3 s ± 0.1 s

D Overview of 5 non-SR neurons

Fig. 37 Comparison of dendritic and somatic response strengths of SR neurons with weakly- or non-responding neurons. (A) Example for a SR neuron. At the left side: Partial reconstruction of the apical dendrite. At the right side: Example fluorescence transient during principal whisker stimulation (1 s, 10 Hz) illustrated with grey bars. The numbers below correspond to the mean values ± SEM of the response amplitudes and full-width-at-half-maximum of the response transients of 17 cells. (B) Somatic versus dendritic response strength of 17 SR neurons. The response amplitudes were normalized to the largest response recorded throughout each experiment. (C) Same as in (A) but here the example shows a weakly-responding neuron. (D) Same as (B) but for 6 weakly- or non-responding neurons.

3.7.8 Relationship between dendritic calcium spikes and somatic output firing of SR neurons

To further analyze the correlation between somatic and dendritic responses to sensory stimulation, the two cellular compartments were recorded simultaneously. Therefore, a SR neuron was identified from a cell population labeled with Cal-590 AM in layer 5 and subsequently electroporated with OGB-1. The electroporation pipette was retracted and after the waiting time for intracellular dye diffusion, a second patch-pipette was used to target the cell for cell-attached recordings, as shown schematically in fig. 38 A. Action-potentials were then recorded during spontaneous activity, as well as sensory stimulation. The SR neurons had a spontaneous firing rate of 2.8 Hz ± 0.7 Hz (mean ± SEM) and increased their output firing to 30 ± 5 action-potentials at an average frequency of 79 Hz ± 18 Hz per sensory stimulation (exemplified in fig. 38 B; n = 9; mean ± SEM). Each of these strong somatic responses were accompanied by dendritic calcium spikes in the tuft dendrites, which had quite long latencies between stimulus onset and onset of the fluorescence rising phase of 190.6 ms ± 11.3 ms (mean ± pooled SD; 28 trials, recorded in three cells of three animals). The onset latency between the first action-potential and sensory stimulation was comparably short with 42.8 ms ± 3.6 ms (mean ± pooled SD; 28 trials, recorded in three cells of three animals). The number of sensory-evoked action-potentials correlated with the dendritic response amplitude, with a Pearson's correlation coefficient of p = 0.64 between these two cellular compartments (fig. 38 C; 28 trials, recorded in three cells of three animals). In contrast, during spontaneous activity this strong correlation was not observed (fig. 38 D; Pearson's correlation coefficient: p = 0.56; 944 events, recorded from three cells of three animals). Here, dendritic events with amplitudes larger than 60% ΔF/F were recorded in absence of any action-potential firing and in contrast, some somatic events consisting of more than 10 action-potentials with an interspike interval < 100 ms were not accompanied by any dendritic response (fig. 38 D). This discrepancy indicates variable coupling between the dendritic tuft and the somatic output and suggests that the dendritic events recorded in the tuft are not back-propagating action-potentials, but indeed dendritic spikes.
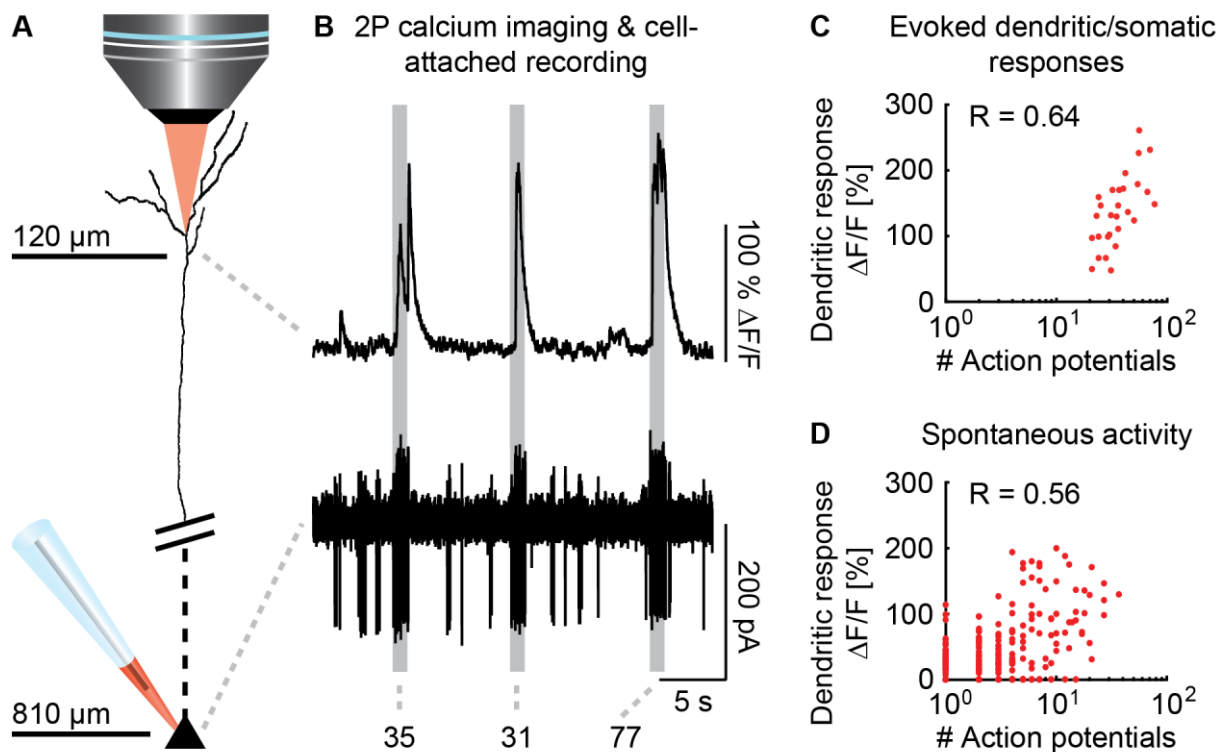
Fig. 38 *Strong correlation between sensory-evoked dendritic and somatic events. **(A)** Schematic display of the experiment: Simultaneous two-photon calcium imaging of the tuft dendrites in layer 1 and cell-attach recordings from the soma in layer 5 in vivo. **(B)** Example for a recording of sensory-evoked dendritic tuft calcium transients at a cortical depth of 120 µm (200 Hz frame rate) and somatic action-potentials recorded from the soma at 810 µm. Principal whisker stimulations are marked with grey bars (1 s, 10 Hz). The numbers of sensory-evoked action-potentials are provided below. **(C)** Sensory evoked dendritic response amplitudes plotted against the number of evoked action-potentials (28 single trials, recorded from three cells in three mice; Pearson's correlation coefficient: p = 0.64). The red dots represent single trials of sensory evoked events. **(D)** Same as in (C) but for spontaneous activity (944 single events, recorded from three cells in three mice; Pearson's correlation coefficient: p = 0.56)*

Dendritic calcium spikes are often associated with high-frequency burst firing of the neuron (Helmchen *et al.*, 1999; Larkum *et al.*, 1999b; de Kock & Sakmann, 2008). Whether slender-tufted neurons fire action-potential bursts elicited by dendritic calcium spikes in the tuft *in vivo* is unknown. For a more detailed analysis of the cell-attached data, the interspike intervals between each pair of action-potentials was calculated, instead of taking the average across trials of whisker stimulation. A burst was defined as a train of action-potentials, elicited at a frequency of at least 100 Hz (de Kock & Sakmann, 2008). Indeed, SR neurons fired bursts of action-potentials at a frequency higher than 100 Hz for each sensory stimulation, as shown in the example in fig. 39 A. The numbers below the action-potential recording indicate the number of action-potentials per burst. On average SR neurons fired 6.5 ± 0.8 bursts of action-potentials per sensory stimulation of one second (fig. 39 B and C; mean ± SD; 111 stimulation trials recorded from 9 cells). During spontaneous activity only 0.3 ± 0.1 bursts were registered within the same time window (mean ± SD, 60 seconds recordings of spontaneous activity at least of 9 cells; Wilcoxon signed rank test, p = 0.0039; n = 9). Each of the sensory-evoked bursts consists of 2 to 16 action-potentials per burst, with a median

value of 2 and an exponential decline towards higher numbers of action-potentials per burst (fig. 39 C & D; n = 9). Only two of 105 stimulation trials, measured in 9 cells, did not elicit somatic burst firing. By measuring dendritic calcium spikes and somatic action-potentials simultaneously, a strong correlation between number of high-frequency bursts and dendritic response amplitude could be demonstrated (fig. 39 E, Pearson's correlation coefficient: p = 0.70; 28 trials, recorded in three cells of three animals). This correlation indicates that the hypothesis of calcium spikes facilitating burst firing holds true for SR slender-tufted pyramidal layer 5 neurons.
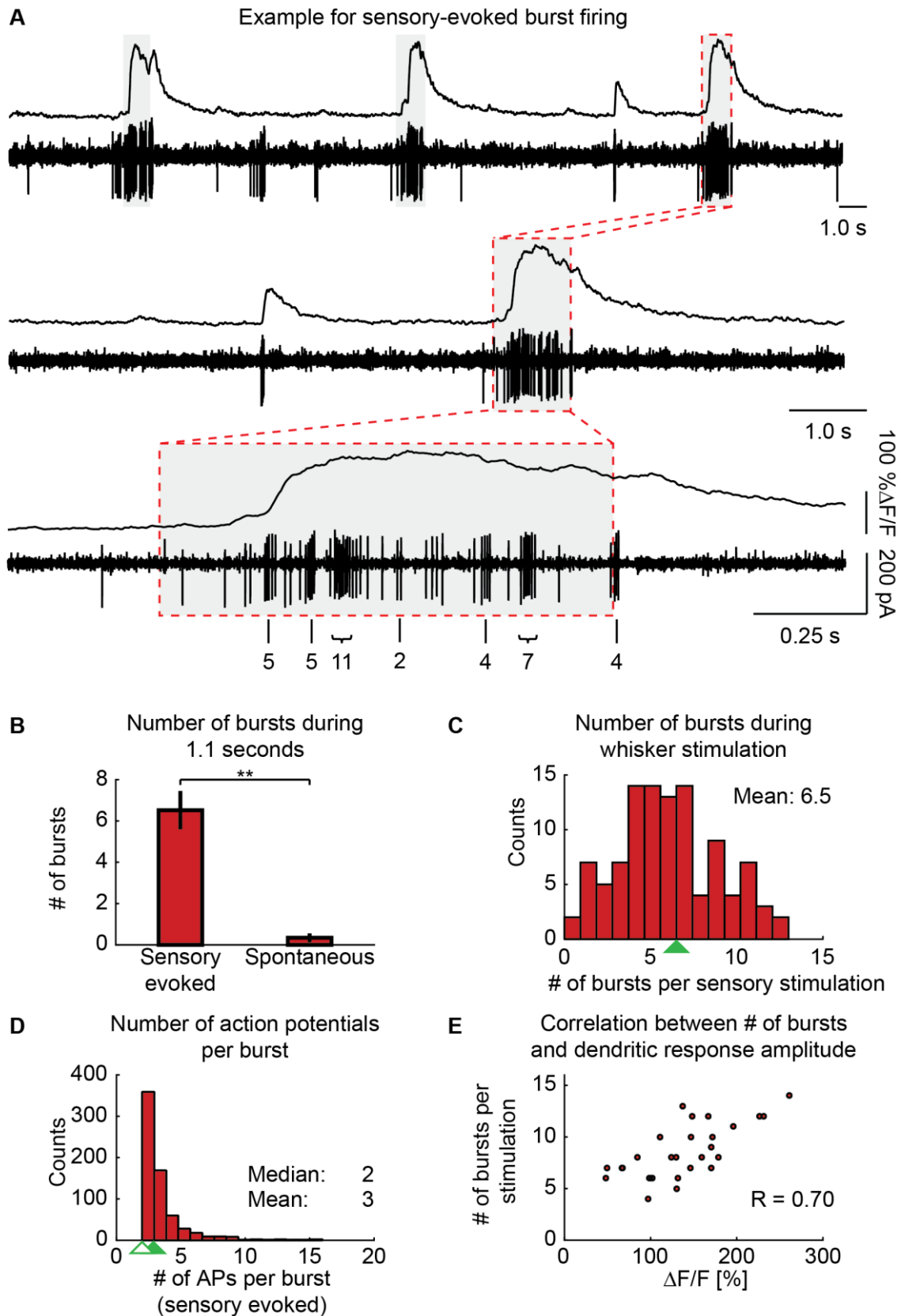
Fig. 39 *Sensory-evoked high frequency burst firing of SR neurons. (A) Example for sensory-evoked responses of a SR neurons with increasing zoom onto a single trial. The numbers below the example with highest zoom indicate the number of action-potentials within each burst (> 100 Hz). (B) Number of bursts during sensory stimulation and spontaneous activity, analyzed within fixed time windows of 1.1 s. The average number of sensory evoked bursts per trial is 6.5 ± 0.8 and is significantly higher than during baseline activity with 0.3 ± 0.1 on average within the same time window (mean ± SD; Wilcoxon signed rank test, p = 0.0039; n = 9) (C)*

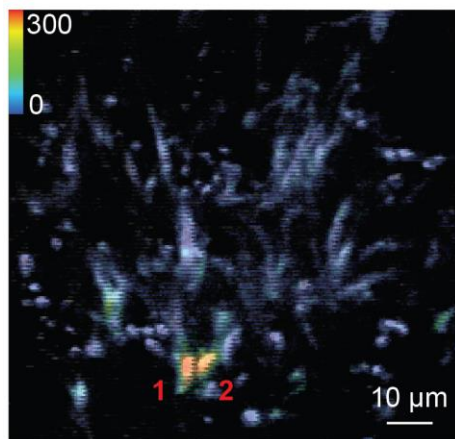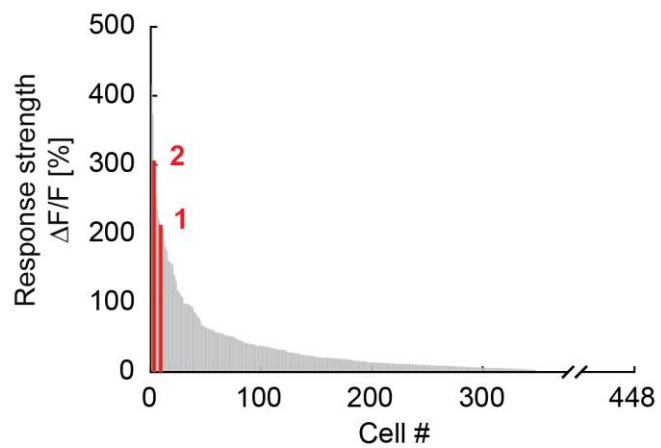### 3.7.9 Dendritic population imaging

The experiments with APV and CNQX showed that glutamatergic inputs to layer 1 tuft dendrites of SR neurons in layer 5 elicit dendritic spikes, which seem to be responsible for burst firing of the cells. However, to understand these signaling mechanisms on a circuit level we need to know where the inputs to layer 1 come from. The most likely candidate is the primary motor cortex (M1), because a previous study showed that inputs from M1 are responsible for dendritic calcium spikes in the superficial dendrites of thick-tufted layer 5 neurons in the mouse barrel cortex (Xu *et al.*, 2012). To test whether this holds also true for slender-tufted L5 neurons, a new experimental approach was be developed. The aim was to image numerous tuft dendrites from cell populations in layer 5 belonging to a specific barrel field and simultaneously block M1 activity. Usually imaging populations of dendrites is challenging, because they are densely packed and each dendrite has only a small diameter. In case of dense cellular labeling, individual dendrites cannot be resolved and their activity can only be recorded as bulk activity of a mesh of dendrites and axons around the resolvable somata. In our approach for deep two-photon calcium imaging, the labeling is restricted to a small volume within the target layer of the cortex. The staining in layer 5 is dense and the basal dendrites of these cells cannot be resolved. However, the tuft dendrites in layer 1 are comparably sparse, because they are distributed across a large volume within the supragranular layers. Thus, the tuft dendrites are not strongly overlapping and can be resolved individually. An example for calcium imaging of a dendritic population filled with Cal-520 AM is given in fig. 40 A. The point- or line-like structures in this field-of-view are tuft dendrites of layer 5 cells, which run perpendicular to the pial surface. Individual dendrites are clearly distinguishable with this technique for imaging planes at 180 µm ± 40 µm (mean ± SD) below the pial surface, corresponding to layer 1 or upper layer 2. If the field-of-view is placed more superficially the number of dendrites increases, due to multiple dendritic branching. Moreover, more and more dendrites are oriented parallel to the surface and thus, overlapping dendrites cannot clearly be distinguished. The optimal imaging depth can be easily determined during the experiment by choosing a field-of-view with good contrast. Individual dendrites were clearly resolved, but note that their baseline level is comparably low, based on low intracellular dye concentrations. The maximum dye concentration inside the dendrites is around 20 µM which is limited by the cellular capacity of intracellular esterases (Stosiek *et al.*, 2003). Calcium concentration changes were reported with large signal amplitudes and high signal-to-noise ratios, as shown in the representable example in fig 40 A and C. The responses to principal whisker deflections are displayed with

pseudocolors, to visualize the response pattern of the dendritic population. In this example two of 36 dendrites were identified as 'SR dendrites' with response reliabilities larger than 80% and average response amplitudes larger than 50% ΔF/F. The corresponding fluorescence transients recorded from this field-of-view are displayed below and the transients belonging to the SR dendrites are marked in red (fig. 40 C and D).

A Imaging depth: 145 μm
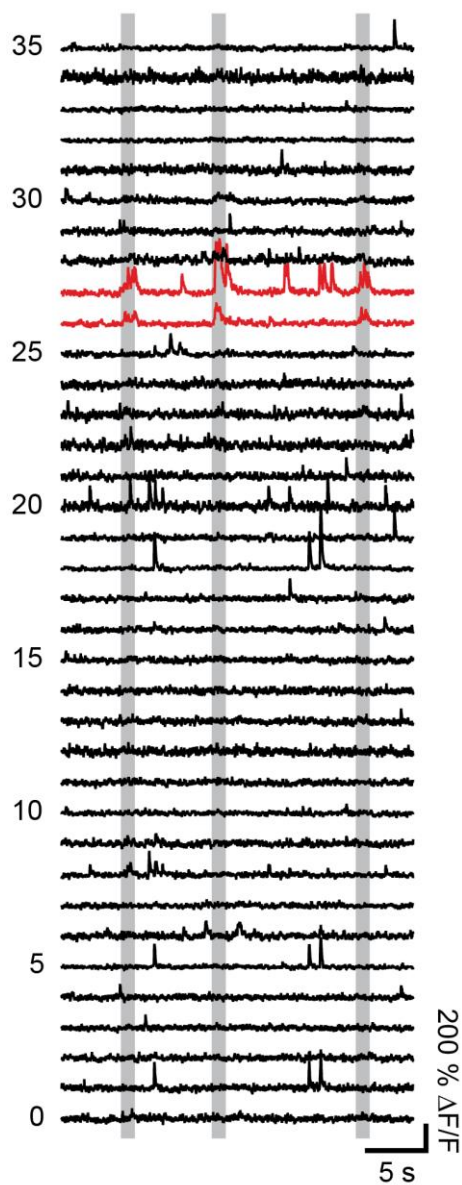
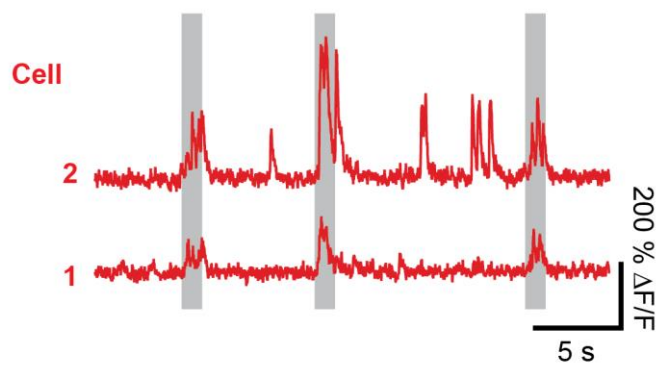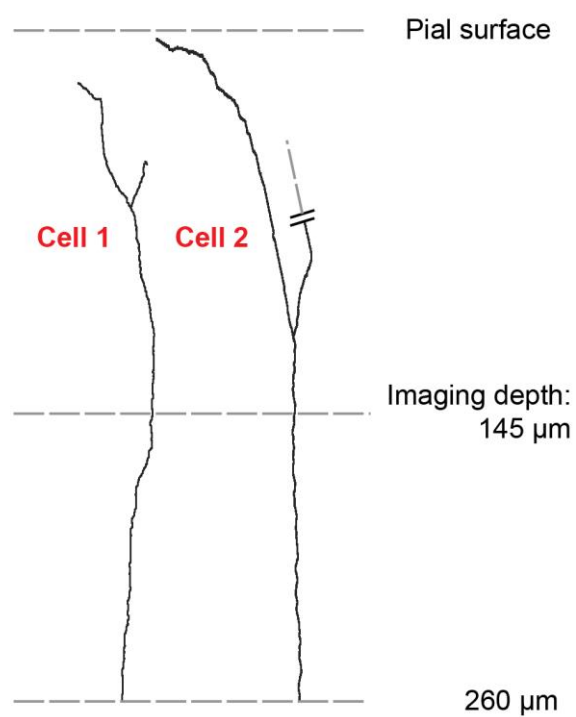**B** Response distribution

C Example calcium transients

D SR dendrites

Cell

2

1

200 % ΔF/F

5 s

E Partial reconstruction of the two cells

Pial surface

Cell 1   Cell 2

Imaging depth: 145 μm

260 μm

200 % ΔF/F

5 s

101

Fig. 40 *Dendritic population imaging of tuft dendrites in layer 1 belonging to pyramidal layer 5 neurons. **(A)** Pseudocolor image of the relative fluorescence overlaid with the black and white image of the averaged two-photon recording of tuft dendrites in layer 1. The pseudocolor scale ranges from 0% to 300% ΔF/F. The imaging field-of-view is 145 μm below the pial surface and was recorded for three times 30 s at a frame rate of 80 Hz. The two dendrites with reliable sensory-evoked responses are marked with red numbers 1 and 2. **(B)** Distribution of sensory-evoked responses of tuft dendrites across cell populations. The individual lines represent single cells, not single dendrites (see text or methods; n = 448 cells from 10 mice). The two cells marked in (A) are highlighted with red thick bars. **(C)** Fluorescence transients from dendrites shown in (A), recorded for 30 s at a frame rate of 80 Hz. Grey bars indicate principal whisker stimulation. The numbers at the left side indicate the ROI number drawn around each dendrite in the field-of-view displayed in (A). The two traces highlighted in red correspond to the two dendrites marked in (A). **(D)** Enlarged view of the calcium transients marked in red in (C). **(E)** Partial reconstruction of the apical dendrites of the two cells from the example in (A) - (D), obtained from a two-photon z-stack. The imaging field-of-view of the recording in (A) as well as the location of the pial surface and the deepest point of the z-stack are indicated with grey dashed lines.*

To analyze these transients cell by cell instead of dendrite by dendrite, dendrites with correlating transients were grouped together (see methods and compare to (Xu *et al.*, 2012)). Therefore, two or more dendrites were averaged and treated as one neurons if the correlation coefficient of the fluorescent transients across all recordings of one experiment was larger than 0.5. The resulting single-cell sensory-evoked responses follow a skewed distribution, as previously observed for somatic imaging in the slightly anesthetized or awake behaving mouse (fig. 40 B). Again, about 10% of the cells (42 out of 448, recorded from 10 mice) fired half of the sensory-evoked activity and only few cells responded reliably and strongly to principal whisker stimulation, whereas most of the cells only respond weakly or not at all. 5% ± 2% of the cells (mean ± SEM; 21 out of 448) respond to principal whisker stimulation with a probability larger than 80%. When the dendritic labeling was sparse enough, tuft dendrites could be reconstructed from z-stacks recorded with the two-photon microscope. In the example shown here, the two dendrites, which fulfill the previously defined condition of super-responsiveness, where reconstructed as shown in fig. 40 E. Even though one branch could not be reconstructed completely, the two dendrites can be assigned to the group of slender-tufted pyramidal neurons with great certainty, because their tuft dendrites are small in width and because of their quite superficial main bifurcation. In summary, a new approach was developed to image populations of dendrites instead of populations of cell bodies, with single-dendrite resolution and high signal-to-noise ratios. Similarly, genetically encoded calcium indicators were used previously to image groups of apical dendrites (Xu *et al.*, 2012; Sheffield & Dombeck, 2015; Sheffield *et al.*, 2017). The authors of these studies labeled cells sparsely with the genetically encoded calcium indicators GCaMP3 or GCaMP6f. In contrast, here we use synthetic calcium indicators and label a dense cell population in layer 5. The tuft dendrites of layer 5 pyramidal neurons showed similar response distribution as their somata, indicating a strong correlation between the sensory-evoked responses of the two cellular compartments.

3.7.10 Possible input sides of tuft dendrites of layer 5 SR neurons

The new approach of dendritic population imaging was initiated with the aim to test whether M1 provides the inputs which elicit dendritic calcium spikes in the tuft dendrites of layer 5 SR neurons. Therefore, dendrites in layer 1 of the barrel cortex were imaged as described before and after M1 was blocked pharmacologically. A second craniotomy was performed above M1 to insert a glass-pipette, filled with the γ-aminobutyric acid (GABA) agonist muscimol (625 µM) and Alexa Fluor 680 (12.5 µM). The pipette was navigated to the center of M1 at a depth of 500 - 600 µm and the solution was slowly pressure-ejected under visual guidance, until a volume of at least 800 µm in diameter was filled with Alexa dye. Subsequently, the imaging field-of-view was set back to the initial location in the barrel cortex, to record sensory-evoked responses from the same dendrites again, which were imaged before the drug application. The muscimol application was repeated blindly, just before each imaging session of 30 s. The dendritic imaging principle is displayed in fig. 41 A - C and the muscimol injection side is indicated in fig. 41 D. In eight SR neurons, recorded from three experiments, the tuft responses did not change significantly by blocking M1 (Wilcoxon signed rank test, $p = 0.41$). Example transients recorded from tuft dendrites in layer 1 before and after muscimol application are displayed in fig. 41 E. The bar graphs in fig. 41 F summarize these results, showing the average responses before and after muscimol application in fig. 41 F. One of the eight cells included here had multiple dendrites in the field-of-view, indicating that this cell could be a thick-tufted layer 5 pyramidal neuron. Even this neuron did not change significantly its dendritic response pattern by blocking M1 inputs (Wilcoxon signed rank test, $p = 0.625$).

Another brain area which is likely to provide inputs to the tuft of SR neurons in layer 1 is the secondary somatosensory area (S2) (Cauller *et al.*, 1998; Yang *et al.*, 2016a). The long latency between sensory stimulation and onset of the dendritic tuft responses indicates that a secondary cortical area could well be the origin of the tuft inputs. In the following set of experiments S2 was blocked with muscimol similarly as described for the blockage of M1 (see methods), while dendritic activity was recorded in the barrel cortex. This time, a significant decrease of dendritic responses was observed (Wilcoxon signed rank test, $p = 0.001$; n = 4 cells recorded from three mice). However, S2 is much closer to the barrel cortex, compared to M1 and a direct inhibition of the barrel cortex induced by the muscimol injection cannot be excluded. In any case, these experiments proof that the muscimol application was effective. Thus, the absence of changes in dendritic responses after blockage of M1 was not due to the ineffectiveness of muscimol but it seems that the dendritic calcium spikes in the tuft dendrites of SR neurons are elicited by inputs of different origin.
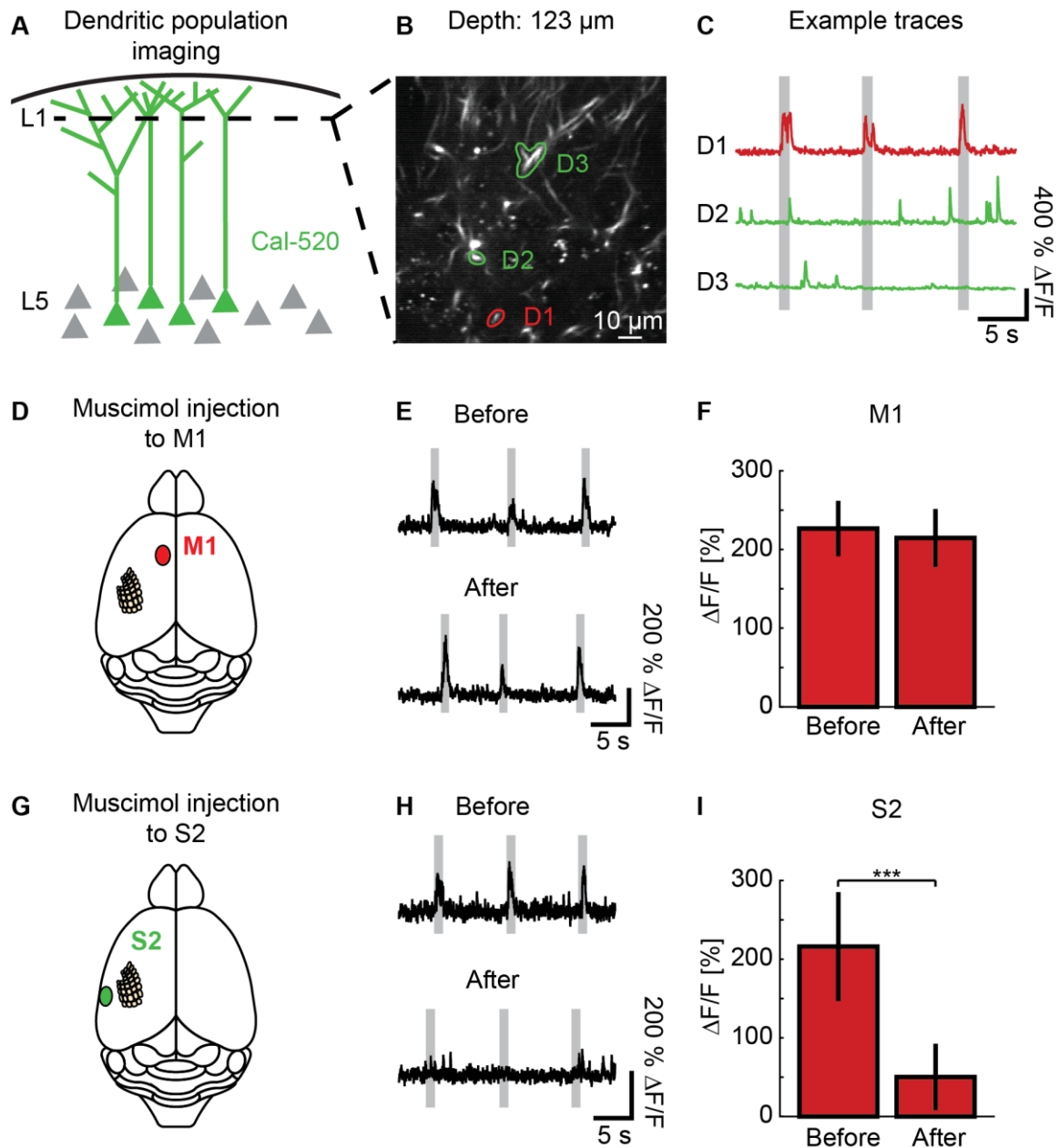
Fig. 41 *M1 is not the input side for slender-tufted SR neurons in layer 5. **(A)** Scheme of dendritic population imaging. Cells in layer 5 are labeled with Cal-520 AM and their dendrites are imaged in layer 1. **(B)** Example field-of-view of a dendritic recording in layer 1, at a cortical depth of 123 µm (average of 30 s, recorded at a frame rate of 80 Hz). **(C)** Example transients of the dendrites marked in (B). The red trace represents a SR neuron. **(D)** Schematic display of the top view of the mouse brain. The spatial location of the primary motor cortex (M1) is indicated in red and the barrel cortex is illustrated by the typical barrel field structure. Two-photon imaging was performed in the barrel cortex, while M1 was blocked by muscimol injection. **(E)** Example traces of SR dendrites before and after the blockage of M1 by muscimol. The grey bars indicate periods of principal whisker deflection (1 s, 10 Hz). **(F)** Summary of the sensory-evoked responses of SR dendrites before and after blockage of M1 (n = 8 cells, recorded from three mice (17 trials of sensory stimulation for each condition); Wilcoxon signed-rank test, p = 0.41). **(G)** Cortical position of the secondary somatosensory cortex (S2) shown in green and the barrel cortex, illustrated by barrel fields. **(H)** and **(I)** Sensory-evoked responses of SR dendrites before and after muscimol application to S2 (n = 4 cells recorded from three mice (11 trials of sensory stimulation for each condition); Wilcoxon signed-rank test, p = 0.001). Similar arrangement as that shown in (E) and (F).*

3.7.11 Determination of strong action-potential output by dendritic calcium spikes

To measure the impact of calcium spikes in the tuft on the somatic output of the SR neurons, electrical recordings from the soma were combined with pharmacological manipulations of the tuft dendrites, as schematically shown in fig. 42 A. The SR neurons in layer 5, which were identified by population imaging with Cal-590 AM, were cell-attached with a patch-pipette. Afterwards, a second pipette, filled with baclofen (100 µM) was located next to the tuft dendrites. Baclofen activates GABA$_B$ receptors which inhibit calcium spikes, by specifically blocking dendritic L-type currents (Perez-Garci *et al.*, 2013). In addition to baclofen, Alexa Fluor 594 (20 µM) was added to the solution inside the pipette to visualize the spread of the Alexa dye during pressure-ejection. To find the ideal position for the drug application, the trunk dendrites of the labeled cells in layer 5 were followed 'upwards' to the surface, comparable to the dendritic population imaging described before. With this trick, the pipette tip containing the baclofen solution could be navigated to the center of the tuft dendrites of the cells imaged in layer 5. The baclofen-solution was pressure-injected at a depth of 100 - 150 µM below the pial surface, until a volume with a diameter of ~150 µm was filled with Alexa. As a result, the number of sensory-evoked action-potentials of the cell-attached SR neuron was significantly reduced by 86% (fig. 42 B and C; Wilcoxon signed rank test, $p = 0.028$; $n = 6$). These experiments demonstrate a strong impact of dendritic calcium spiking of the SR neurons in layer 5 on their action-potential output firing.
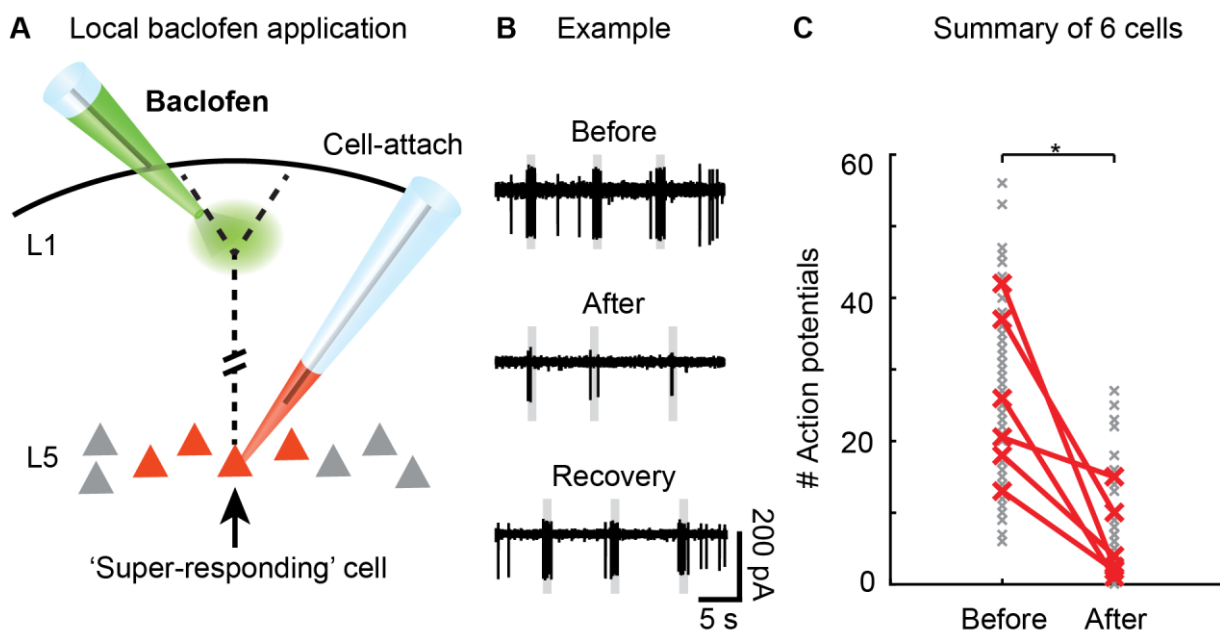
Fig. 42 *Dendritic calcium spikes determine action-potential output. **(A)** Scheme of the experimental procedure: A SR neuron labeled with Cal-590 AM was cell-attached, while a second pipette was used to apply baclofen locally to the dendrites in layer 1, under visual guidance. **(B)** Action-potential recordings of a SR neuron before and after baclofen application to layer 1, as well as after a couple of minutes of recovery time. **(C)** Summary of the sensory-evoked responses before and after baclofen application of six cells. Grey crosses represent single trials, red crosses mark the average response of each cell. (Wilcoxon signed-rank test: $p = 0.03$; $n = 6$)*

4 Discussion

4.1 Deep two-photon calcium imaging *in vivo*

4.1.1 Theoretical consideration of the 3-fold improvement in imaging depth with the new method

For standard imaging of cell populations using AM calcium dyes, the penetration depth limit is about 300 µm below the cortical surface of the living mouse, as demonstrated in the beginning of this work. The new method of deep two-photon calcium imaging shifted this limit down to 900 µm below the cortical surface, providing direct access to the deep cortical layers 4 to 6 in the mouse brain *in vivo (Tischbirek et al., 2015; Birkner et al., 2017)*. Such a drastic improvement was mainly achieved by two factors: first, by a minimization of the background fluorescence due to the spatial restriction of the fluorescent dye application to the cell layer of choice. Second, the use of calcium indicators with red-shifted excitation wavelengths decreased scattering in biological tissue. Classical calcium indicators are two-photon excited at about 800 nm to 950 nm. For example, the widely used calcium dye OGB-1, which was also used here, has its optimal two-photon excitation wavelength at 920 nm. In contrast, the new red-shifted calcium dye, Cal-590, has a two-photon excitation wavelength of about 1050 nm (Tischbirek *et al.*, 2015; Birkner *et al.*, 2017). To evaluate the different in penetration depths of light with 920 nm or 1050 nm in biological tissue, previously published data about attenuation lengths of light in mouse brain tissue can be used (Shi *et al.*, 2016). The expected improvement in depth penetration, derived from these measurements, is less than 50 µm. The increase of about 600 µm achieved here can thus be hardly explained only by the red-shift of the two-photon excitation wavelength. Note that the attenuation lengths were measured in fixed brain tissue and do not reflect the *in vivo* imaging situation (Shi *et al.*, 2016). Despite this difference, the data provided from this work can still serve as a good approximation. Besides the long-wavelength excitation, a major factor for the successful imaging of layers 5 and 6 of the mouse cortex *in vivo* was the visually-guided local application of the fluorescent dye (Birkner *et al.*, 2017). As shown experimentally, it is impossible to perform deep two-photon calcium imaging with standard labeling procedures. The restriction of the fluorescence to the target cell layer increased the imaging depth by several hundred micrometers. Additional micrometers in depth penetration were gained by optimizing the two-photon microscope for deep two-photon imaging: the fluorescence excitation was improved by underfilling the objective lens, which reduces excitation light scattering (Dunn *et al.*, 2000; Helmchen & Denk, 2005; Kondo *et al.*, 2017). The detection was maximized with a hybrid photodetector, located close to the back aperture of the objective lens, which can increase the signal-to-noise ratio of the detected fluorescence signal (Zinter & Levene, 2011; Tischbirek *et al.*, 2015). In addition, to further increase the maximum imaging depth, the surgical procedures involved in the *in vivo* experiments were

optimized as well. For example, the imaging regions were carefully chosen to avoid strongly light-absorbing vasculature.

Overall, multiple factors have to be taken into account to explain the successful increase of the maximum imaging depth. Each of these improvements contributed to set the imaging depth limit a bit further towards the deepest end of the cortex, resulting in an increase in imaging depth of a factor of three compared to the initial experiments.

4.1.2 Comparison of the new deep two-photon calcium imaging method to other approaches

The depth limit of two-photon microscopy is an obvious obstacle, which many researchers tried to overcome. One advantage of the deep imaging method presented here, is that the invasiveness is not increased, compared to standard two-photon imaging procedures *in vivo*. It allows for the direct access of deep cell layers in the intact cortex, located down to 900 µm within the brain tissue. In comparison, a very popular method to directly access deeply located brain regions without any depth limitation for one- or two-photon calcium imaging is the use of microendoscopes (Jung *et al.*, 2004; Grewe *et al.*, 2017; Zong *et al.*, 2017). This was not an option here, because the invasive procedure of implanting a GRIN lens into the cortex destroys intracortical circuits, which were studied here.

Alternatively, low-invasive deep calcium imaging techniques were described in previous work. However, none of these approaches matches the experimental requirements here. For example, the use of a regenerative amplifier to increase the two-photon excitation efficiency was excluded because of its high cost and because it implies the reduction of the imaging speed to about 16 Hz frame rate (Mittmann *et al.*, 2011). Here, we used high-speed imaging at 40 Hz to 500 Hz frame rates, which are solely limited by the speed of the scanner unit used inside the microscope (Tischbirek *et al.*, 2015). In addition, Cal-590-based imaging comes at low cost, because relatively inexpensive Ytterbium fiber lasers can be used for two-photon excitation. Another non-invasive technique for deep imaging is the application of adaptive optics. The spatial resolution and the image contrast were greatly improved with adaptive optics so that even single axonal boutons could be imaged in layer 4 of the mouse primary visual cortex *in vivo* (Sun *et al.*, 2016). In this study, these fine structures were especially brighter in images recorded with adaptive optics compared to images acquired without correction, but the maximum imaging depth was not greatly improved (Wang *et al.*, 2015). For the method developed in the study presented here, we aimed at a more drastic increase of the imaging depth with less complex hardware implementation. The hardware adaptions of the new two-photon microscope were mostly implementations of new optics, which accept red-shifted excitation wavelengths up to 1300 nm and which can be quite easily exchanged in any standard two-photon microscope. In addition, the fluorescence detection

was maximized by exchanging the standard photomultiplier tube with a hybrid photodetector, which was placed near the back aperture of the objective lens. Thus, after minor changes to a generic two-photon microscope and by following the practical guide of biological deep two-photon experiments provided here, two-photon imaging in a depth of 900 µm within brain tissue can be readily performed.

In previous studies, even longer excitation wavelengths beyond 1050 nm were used to increase the two-photon imaging depth. The goal of this approach is to excite the fluorophores with three instead of two photons. In fact, three-photon excitation makes use of the two advantageous effects used in the study here for deep imaging: The reduction of light scattering by red-shifted laser light wavelengths and the minimization of background fluorescence due to the restriction of three-photon excitation to an even smaller volume compared to two-photon excitation. Only recently, three-photon microscopy was applied to *in vivo* calcium imaging, by exciting the standard genetically encoded calcium indicator GCaMP6 with 1300 nm (Ouzounov *et al.*, 2017). Not only the whole cortex, but also the underlying hippocampus were functionally imaged in the intact brain, raising great promises of this technique for future application. One drawback of this method might be the necessity of laser sources with a low duty cycle to provide intensive laser pulses to generate sufficient three-photon excited fluorescence. The laser source used in this three-photon study was a noncollinear optical parametric amplifier pumped by a regenerative amplifier and emitted pulses at a repetition rate of 400 kHz which was doubled with an optical delay line (Ouzounov *et al.*, 2017). Whether more classical lasers with pulse repetition rates of around 80 MHz could be used for three-photon excitation of classical calcium indicators is questionable because three-photon cross-sections of these indicators are usually extremely low. Based on my own experience with three-photon excitation of the calcium dye Indo-1, I would expect that extremely high average laser power values at the tissue surface might be necessary to generate enough fluorescence at deep brain structures with classical laser sources. However, the development of new laser sources, as well as calcium indicators is ongoing and three-photon excitation is a promising strategy for future deep imaging experiment. In comparison to deep imaging with three-photon excitation, the deep imaging method developed here makes use of commercially available Ytterbium-doped fiber lasers. These have multiple benefits, including the emission of high power laser light, their robustness and relatively low cost (Xu & Wise, 2013). Versions with short laser pulses in the range of 50 fs are available and noisy water cooling is not required, which is particularly important for experiments with awake behaving animals, as presented here (Xu & Wise, 2013; Tischbirek *et al.*, 2015; Birkner *et al.*, 2017).

To further improve the deep imaging technique applied here, the combination with other methods could be a promising strategy. For example, it could be combined with adaptive optics to increase the spatial resolution and image contrast at depth. Alternatively, the background fluorescence could be further reduced by using Bessel-beam illumination instead of Gaussian beams (Fahrbach *et al.*, 2010). Another technique to avoid fluorescent background is to introduce aberration to the excitation beam and generate an image on the fluorescence background only, which can be subtracted from the original image (Leray & Mertz, 2006; Leray *et al.*, 2008). However, neuropil fluctuations cannot be canceled out with this strategy.

In summary, each deep imaging approach has its strengths and drawbacks. The advantages of the method described in this work include, among others, a low invasiveness, the relatively simple hardware implementation and the option of high-speed imaging up to a frame rate of 500 Hz. The combination with other deep imaging strategies could increase the imaging depth even further.

4.1.3 Comparison of Cal-590-based imaging with the use of other red-shifted calcium indicators

Red-shifted calcium indicators become more and more popular because of their advantage for deep imaging and due to the possibility of multi-color imaging or simultaneous manipulations with optogenetics (Packer *et al.*, 2015). In parallel, new two-photon laser light sources with emission wavelengths beyond 1000 nm are under ongoing development. We introduced deep calcium imaging with a combination of the new red-shifted calcium indicator Cal-590 and Ytterbium-doped fiber lasers (Tischbirek *et al.*, 2015; Birkner *et al.*, 2017). Besides Cal-590, diverse red-shifted fluorescent probes are commercially available, which were used, for example, to image morphological structures deep inside the mouse brain tissue (Horton *et al.*, 2013a). The design of red-shifted functional fluorescent probes, however, is more challenging (Oheim *et al.*, 2014). Traditional red-shifted calcium indicators, such as Calcium Orange or Calcium Crimson were hardly used *in vitro* or *in vivo* because of diverse difficulties, such as poor SNRs or subcellular compartmentalization (Yaksi & Friedrich, 2006; Oheim *et al.*, 2014). Only few examples show the successful application of red-emitting calcium indicators to functional imaging of neurons *in vivo*, such as the application of Rhod-2 to imaging of neural activity in the living zebrafish. For this reason, Rhod-2 AM was applied in the present work to *in vivo* calcium imaging of neurons in the mouse cortex but the resulting image quality and the calcium reporting properties of Rhod-2 AM were poor compared to Cal-590 AM. An improved version of Rhod-2, Rhod-PEG, with enhanced calcium-sensing sensitivity and less compartmentalization was recently developed, which could lead to better results compared to Rhod-2 (Ponsot *et al.*, 2017). Another rhodamine-based calcium dye, which was successfully used for neuronal calcium

109

imaging in acute mouse brain slices, is CaSir-1 AM (Egawa *et al.*, 2011a). *In vitro* experiments with the red-shifted fluorescein-based calcium dyes Asante-CaRed-1 AM (Hyrc *et al.*, 2013) and CaTM-2 AM (Egawa *et al.*, 2011b) provide promising results, as well as the experiments with CaRuby-Nano (Collot *et al.*, 2012; Collot *et al.*, 2015), which was used for to *in vivo* calcium imaging of cerebellar Purkinje cells. Whether any of these recently developed red-shifted calcium indicators can be applied to deep cortical imaging of the mouse brain *in vivo*, is unclear.

As an alternative approach, red-shifted genetically encoded calcium indicators (GECIs) (Ohkura *et al.*, 2012; Akerboom *et al.*, 2013; Inoue *et al.*, 2015; Dana *et al.*, 2016; Shen *et al.*, 2018) can be used for deep two-photon imaging in the living animal. These indicators have a stable expression for multiple weeks, allowing for chronic imaging experiments (see for example (Chen *et al.*, 2013; Pilz *et al.*, 2016; Bethge *et al.*, 2017)). A second major benefit of GECIs, in general, is the option of targeted expression in specific cell types, brain areas or cortical layers of interest. Out-of-focus fluorescence can be prevented by expressing the indicator either sparsely or solely in deep cortical layers of the mouse brain. For example, a subpopulation of layer 6 neurons was targeted for jRCaMP1a expression by injecting a Cre-dependent adeno associated virus into the cortex of the neurotensin receptor 1 (NTSR1)-Cre mouse line (Gong *et al.*, 2007). Single-cell calcium transients were recorded in layer 6 of the primary visual cortex of these mice *in vivo* (Dana *et al.*, 2016). Recently, another group generated a new mouse line, specifically expressing R-CaMP1.07 (Ohkura *et al.*, 2012) in either of the cortical layers 2/3 to 6 (Bethge *et al.*, 2017). They imaged single-cell activity across all cortical layers of the awake behaving mouse, down to 740 µm below the cortical surface. One year before, the same group successfully recorded calcium activity of dentate granule cells reported by R-CaMP1.07, which was expressed by viral injection (Pilz *et al.*, 2016). In this study, they removed the cortex above the hippocampus surgically to implant a chronic window on top of the hippocampal surface and were able to record dentate granule cell activity at about 600 µm - 800 µm below the hippocampal surface. Again, in this study, background fluorescence was largely avoided by restricting the expression of the fluorescent indicator to dentate granule cells of the hippocampus. This enabled them to record the dentate granule cells even with the bright green-emitting probe GCaMP6s with similar image quality compared to recordings with the red-emitting R-CaMP1.07 (Chen *et al.*, 2013).

All of these studies show a successful application of red-shifted genetically encoded calcium indicators to deep calcium imaging *in vivo*. However, none of these deep calcium imaging recordings were validated by simultaneous recording of the underlying action-potentials.

Thus, the sensitivity of these measurements remains unclear and undetected action-potential activity cannot be excluded.

The combination of targeted single-cell electrophysiology and two-photon calcium imaging *in vivo* is not trivial, especially deep inside the cortical tissue, because the pipette tip needs to remain clean while being navigated through dense cell layers. Here, we calibrated the fluorescence transients measured by combined cell-attached recordings in layer 2/3 of the mouse cortex *in vivo*, but also at a depth of 740 µm below the cortical surface (Tischbirek *et al.*, 2015). In the upper cortical layers, the calcium measurements reported by Cal-590 AM are highly sensitive with single action-potential resolution. Even at deep cortical layers, calcium concentration changes were reported reliably and with a high sensitivity, for events corresponding to two or more action-potentials. The fluorescent transients were characterized by fast kinetics, with a somatic rise time of 2 ms for a single action-potential-evoked event which is more than 20 times faster than that of the fast genetically encoded indicator GCaMP6f (Chen *et al.*, 2013) and the comparably fast red version R-CaMP2 (Inoue *et al.*, 2015). The somatic decay time constant is about 255 ms, which is slightly slower than GCaMP6f (~142 ms) or R-CaMP2 (~170 ms). Moreover, synthetic calcium dyes usually have one binding site for each calcium ion, leading to a fairly linear relationship between calcium concentration and reported fluorescence, compared to genetically encoded calcium indicators with four calcium binding sites for most GECIs (Mank & Griesbeck, 2008; Rose *et al.*, 2014). In addition, compared to GECIs, synthetic calcium dyes can be readily used in acute experiments, but the cell labeling is not long lasting and chronic experiments are impossible. Certainly, genetically encoded and synthetic calcium indicators both have strengths and weaknesses and researchers can benefit from both approaches for functional two-photon microscopy and the toolbox is now enriched by a new protocol for deep imaging.

4.2 Analysis of sensory processing of layer 5 neurons in the mouse barrel cortex

4.2.1 Skewed distributions of sensory-evoked single-cell responses across cell populations

With the help of the new deep calcium imaging method, dense cell populations in layer 5 of the mouse barrel cortex became accessible for functional imaging with single-cell resolution. Neuronal calcium imaging was performed in the awake and anesthetized mouse cortex in the combination with simple sensory stimuli. Under both conditions, only few cells became active in response to principal whisker deflection. Interestingly, the single-cell responses followed a skewed distribution with only 10% of the whole cell population in layer 5 being responsible for 50% of the evoked activity. These findings are well in line with many other studies. Similar results were obtained from two-photon calcium imaging of layer 2/3 of the mouse barrel cortex *in vivo* (O'Connor *et al.*, 2010) and also cell-attached recordings from all cortical layers of the mouse cortex indicate that the sparseness of responses to sensory stimuli is a general feature of cortical processing (Hromadka *et al.*, 2008; O'Connor *et al.*, 2010). In fact, electrophysiological recordings from the cerebral cortex across different species resulted in skewed distributions of firing rates under spontaneous as well as evoked conditions (for review see (Buzsaki & Mizuseki, 2014)). However, these electrophysiological studies were mainly performed by measuring action-potential activity with extracellular recordings, which are biased towards active neurons (Shoham *et al.*, 2006; Hromadka *et al.*, 2008). Alternatively, single-cells were cell-attached to include non-active neurons into the analysis (Hromadka *et al.*, 2008; O'Connor *et al.*, 2010). However, this is only possible for one neuron at a time. The activity of the surrounding neurons remains undetected and the cell type and cell morphology remain unknown as well. In my study, the distribution of single-cell responses of cortical layer 5 neurons to sensory stimuli was analyzed with two-photon calcium imaging. Active as well as inactive neurons were detected in an unbiased way, resulting in a heavily-tailed distribution of single-cell responses, which confirms former electrophysiological studies.

A very small subset of neurons, comprising around 5% of the whole cell population, was characterized by large responses to principal whisker stimulation and with a response probability close to 100%. During one second of stimulation, around 30 action-potentials were evoked, fired at about 80 Hz on average. In contrast, under baseline conditions these cells showed activity at approximately 3 Hz, leading to a high SNR to report sensory input. Usually, one of these 'super-responding' (SR) neuron was identified per mouse experiment, because only a subset of layer 5 cells corresponding to one barrel field was imaged. The estimated overall number of SR neurons in layer 5 of one entire barrel column is around 55, assuming a homogeneous distribution of SR neurons in layer 5 and an overall number of

excitatory neurons of 1095 ± 96 in layers 5A and 5B, as measured by (Lefort *et al.*, 2009). In this study, the responses of SR neurons to principal whisker deflection and surround whisker deflection were analyzed. Whether these cells are tuned to specific deflection directions, for example, is unknown. Hypothetically, the SR neurons could be highly tuned to one feature of the stimulation, such as direction or angle of deflection, and different sets of SR neurons could be activated by different kinds of principal whisker deflections. Alternatively, these cells could be in general more excitable compared to the surrounding cells and could have a broad receptive field. This second hypothesis is supported by previous studies showing quite preserved firing rates of individual neurons in the CA1, measured across different spatial environments of the animal (Mizuseki & Buzsaki, 2013). Weakly responding neurons show a higher variability in response strength, probably because they have weaker synapses which are usually turned over more rapidly, than strong ones (Holtmaat & Svoboda, 2009). In my work, similar results were observed when comparing imaging sessions, performed under anesthetized or awake conditions, in order to record from the same set of neurons at different time points and under different cortical states. SR neurons exhibited robust responses for both recordings, whereas the variability of weaker responding cells was much higher (fig. 32 E). It is well possible that the robust responding SR neurons are activated for different whisker input as well. On the other hand, it is well known that cortical cells can be highly selective to specific features of the sensory stimuli. For example, pyramidal neurons in the primary visual cortex encode different orientations of visual stimuli selectively (Hubel & Wiesel, 1959, 1968, 1969). In the rodent barrel cortex, a similar tuning of neuronal responses could be observed for the principal whisker towards different directions (Simons, 1983; Manns *et al.*, 2004; Lavzin *et al.*, 2012). Future experiments with different sets of whisker stimuli could validate whether the SR neurons found in my work are highly specific to different stimuli features or strongly respond to a broad range of sensory inputs. Moreover, this study could be extended to other cortical layers and other sensory cortical areas, to investigate whether the phenomena found here represent a general mechanism.

4.2.2 Single-cell morphology and connectivity of layer 5 SR neurons

In the present study, five percent of the neural cell population was characterized to be functionally distinct from the rest of the dense neural cell population. To figure out whether these cells are also morphologically or biophysically unique, they were targeted with single-cell electroporation, cell-attached recordings and pharmacological manipulations. Remarkable similarities were found between these cells including a slender-tufted morphology for 17 out of 18 SR neurons (fig. 35 A). Slender-tufted pyramidal neurons are the major cell type in layer 5, comprising 39% of all neurons in that layer (Hattox & Nelson, 2007). Furthermore, the recording site in the present study included mainly layer 5A, whereas thick-tufted layer 5 neurons in the mouse barrel cortex are mainly located in layer

5B. It could well be that more thick-tufted SR neurons are located at a cortical depth approximately 50 µm deeper than the recording side chosen here. Two-photon calcium imaging from layer 2/3 in the mouse barrel cortex indicates the existence of SR neurons in upper cortical layers (O'Connor *et al.*, 2010). It is well possible that each cortical layer comprises of few SR neurons and it will be of major interest to find similarities of these cells across layers in future experiments. Another open question is the origin of the subcellular inputs driving the strong activation of the layer 5 SR neurons. We were able to exclude M1 as most likely candidate, but alternative input sides were not extensively tested. It would be interesting to know whether the SR neurons exclusively obtain inputs from a specific brain region, or whether all layer 5 neurons are similarly connected, but with different synaptic strength.

4.2.3 Underlying mechanisms of 'super-responsiveness'

The subcellular activity of the SR neurons was investigated to gain a deeper understanding of 'super-responsiveness' in a small subpopulation of layer 5 neurons. Therefore, SR neurons were identified across dense cell populations in layer 5 *in vivo* and targeted with single-cell electroporation of a spectrally distinct calcium indicator. After the dye diffused intracellularly, fluorescence changes were recorded from the corresponding tuft dendrites in layer 1. Principal whisker deflection elicited large calcium transients in the tuft dendrites, which occurred globally in all tuft branches. The largest amplitudes of these signals were found close to the main bifurcation point, raising two options of their origin, being either back-propagating action-potentials or dendritic calcium spikes. In general, the amplitude of back-propagating action-potentials decreases along the apical dendrite towards the distal dendritic tree (Larkum & Zhu, 2002; Grewe *et al.*, 2010). However, in case of high-frequency action-potential firing of the soma, back-propagation can induce small calcium transients in the tuft dendrites of slender-tufted layer 5 neurons in the mouse cortex, at least *in vitro* (Grewe *et al.*, 2010). Thus, it is well possible that back-propagation contributes to the dendritic signaling measured here. However, synaptic inputs are required to initiate large amplitude dendritic signals, which does not support the notion that these signals are of purely somatic origin and indicates that the observed signals are indeed dendritic calcium spikes. In previous studies, dendritic calcium spikes lead to high-frequency burst firing of the cells, which could explain the strong activation of the somata recorded here (Helmchen *et al.*, 1999; Larkum *et al.*, 1999b). Indeed, in my study, the pharmacological blockage of L-type calcium channels in layer 1 leads to a drastic reduction of somatic action-potentials, indicating a strong impact of dendritic on somatic output firing. Again, this result suggests that the dendritic events are not back-propagating action-potentials, but calcium spikes initiated in the tuft.

4.2.4 Dendritic spikes in tuft dendrites of layer 5 neurons of the mouse barrel cortex

The relation between tuft signaling and somatic output *in vivo* could only be studied here by simultaneously imaging the tuft dendrites in layer 1 and cell-attaching the soma to record action-potentials. This procedure is experimentally challenging, especially regarding the deep location of the somata. Except for one study, performing blind whole-cell patching of layer 5 cells *in vivo* (Helmchen *et al.*, 1999), the work presented here is to my knowledge the only study performing cell-attached recordings and simultaneous dendritic recordings from layer 5 cells *in vivo.* Other studies on dendritic spikes of layer 5 pyramidal neurons were restricted to imaging populations of tuft dendrites labeled with GCaMPs (Magee, 2000; Cichon & Gan, 2015; Takahashi *et al.*, 2016). In the mouse barrel cortex, large dendritic events were found in a small subset of thick-tufted layer 5 neurons, which occurred preferentially during active object touch. Passive whisker deflection barely elicited calcium transients in tuft dendrites in the awake mouse and never in isoflurane anesthetized mice. Thus, it could well be possible that thick-tufted neurons integrate information about motion and touch, as they receive direct inputs from M1. In contrast, the slender-tufted neurons found here fire dendritic calcium spikes in response to passive whisker deflection and are not influenced by M1. It seems that thick- and slender-tufted neurons encode different information about whisker motion and touch and their interplay will be an interesting research topic for future experiments.

4.2.5 Functional role of somatosensory cortical layer 5 SR neurons

The cellular and subcellular mechanisms underlying sensory-evoked activity in layer 5 of the barrel cortex were elucidated here. However, the functional role of layer 5 cells and SR neurons in particular can only be speculative. Following the convergence of information in the barrel cortex, it might be a node of integration for external sensory stimuli with motor activity (Curtis & Kleinfeld, 2009; de Kock & Sakmann, 2009). Slender-tufted neurons in layer 5A of the rat barrel cortex were activated by free whisking without touch, probably via the paralemnsical pathway to layer 5A (de Kock & Sakmann, 2009). In contrast, thick-tufted pyramidal neurons located in layer 5B were hardly activated by whisker motion, but increased their spiking activity with passive whisker touch (de Kock *et al.*, 2007). Together with anatomical studies, this lead to the hypothesis that slender-tufted layer 5A neurons carry information about whisker motion, whereas thick-tufted layer 5B neurons encode whisker touch (de Kock *et al.*, 2007; de Kock & Sakmann, 2009; Oberlaender *et al.*, 2011). However, this might only be half the truth, because these conclusions are based on an average view across cell populations. Here, we found large difference of sensory-evoked responses on a single-cell level. A small subset of slender-tufted layer 5 neurons was strongly activated by passive whisker touch. As these neurons only comprise 5% of the overall layer 5 cell population, it is well possible that these cells were simply overlooked by previous electrophysiological recordings. To keep the single-cell inputs as reliable and well-defined as

115

possible, only passive whisker deflection was included here without motor input from active whisking. Therefore, layer 5 cells were recorded solely during quiescence of the awake mice or in slightly anesthetized mice. Whether the SR neurons receive additional motion-related inputs can be clarified by future experiments including active whisking.

Besides the integration of whisker motion and touch, the mouse barrel cortex could have more complex functions. Following Michael Brecht's theory it might well be that a representative image of the body is formed in layer 4 of the cortex and predicts or 'simulates' future movements as well as their consequences by help of the interaction of multiple cortical layers (Brecht, 2017). He argues that the cellular sensory responses get more and more elaborate from thalamus to cortical layer 4, to the supra- and infragranular layers, which are unlikely to just serve as multiple relay stations for sensory mapping. The emergence of phantom limbs after limb amputation, or the fact that rats with cortical lesions can still sense their environment but fail in tasks involving knowledge about their body, are other indicators for a cortical role in body representation and prediction (please refer to (Brecht, 2017)). Experimental evidence for this theory is difficult to provide. It is well possible to disturb cortical circuits with lesions or optogenetics, but the provoked or inhibited animal's thoughts are undetectable. Following Brecht's argumentation we can only look for anatomical, physiological or behavioral hints matching his hypothesis. Anatomically, layer 5 can receive motor and sensory inputs and provides the major output of the cortex. The SR neurons investigated here most likely receive inputs to the tuft from higher cortical areas, as indicated by long onset latencies of dendritic spikes found in their tuft dendrites. Simultaneously these cells receive information about external stimuli from the periphery, which turns them into likely candidates to relate the internal body map to externally perceived information. However, this is highly speculative and whether the true function of these cells or layer 5 of the cortex can ever be shown experimentally is an open question.

Recently, the group of Matthew Larkum tried to reveal the role of dendritic calcium spikes in tuft dendrites of layer 5 pyramidal neurons of the mouse barrel cortex in a tactile detection task (Takahashi *et al.*, 2016). By blocking dendritic calcium spikes in layer 1 optogenetically or pharmacologically, the detection threshold of the sensory stimuli decreased significantly, whereas enhanced dendritic activity in layer 1 increased the detection threshold (Larkum *et al.*, 1999b). Feedback signals to primary sensory areas mostly arrive in layer 1 and were shown to be crucial for conscious perception (Manita *et al.*, 2015; Kwon *et al.*, 2016). Thus the authors here argued that by manipulating that feedback loop they influence the perception threshold of the sensory stimuli (Takahashi *et al.*, 2016). This study used bulk loading of genetically encoded indicators and optogenetic probes. Calcium imaging as well as cellular manipulations were performed on a populational level. The role of single-cell and

cellular subtypes in the perception of touch-related signals remains unknown. The experimental results presented in my study point out the importance of dissecting neural populations into subgroups, because small subsets of cells can have major impact on cortical output. The small group of SR neurons provides the major output signal induced by sensory stimulation. The strong output firing is determined by dendritic calcium spikes in tuft dendrites of these cells. Thus, these cells could play a major role in sensory perception.

It might be that all of these hypothesizes about the functional role of the barrel cortex are true and layer 5 of the barrel cortex is involved in the integration of touch and motion information, in generating an internal body map to simulate or predict body actions and in consciously perceiving sensory inputs. All of these functions are highly speculative, but the detailed analysis of anatomy-function relationships of single-cells can lead to a better understanding of the functional role of the cortex.

5 Conclusions

In summary, deep two-photon calcium imaging with Cal-590 plus the spatial restriction of the dye loading, enhanced the imaging depth roughly threefold compared to standard labeling and two-photon imaging procedures. Consequently, deep cortical layers 4 to 6 are now accessible for functional imaging on a single-cell level *in vivo*, which were out of reach with standard procedures used before (Tischbirek *et al.*, 2015; Birkner *et al.*, 2017). The hardware-based changes required for this method can potentially be applied to any two-photon microscope, without major effort but with great improvement in imaging depth. The method can be applied to any cortical region and at any cortical depth without increasing the invasiveness of the experiments. Potentially toxic viral transfections and long waiting periods for genetic expression are not involved and the cells can be readily stained in acute experiments with Cal-590. However, the imaging time is temporally limited to single-day experiments and specific genetically defined cell populations cannot be targeted. Instead, all neural cells within the stained region are homogenously filled with the calcium indicator, which can be advantageous, for example, when screening for functionally specific, instead of genetically defined, cells. Here, dense cell populations where analyzed in view of single-cell responses to simple and well-defined sensory stimuli. In layer 5 of the mouse barrel cortex only few cells reliably respond to the sensory stimuli, whereas the majority of cells remains inactive. This result complements experimental evidence obtained with electrophysiological recordings, which are either biased to active cells or can only target single cells, instead of dense cell populations (Hromadka *et al.*, 2008; O'Connor *et al.*, 2010). It seems likely that the sparse representation of sensory inputs is a general coding mechanism of the cortex but for experimental validation, experiments on a population level need to be performed including all cortical layers and other cortical areas as well. The few cells which stand out with high response reliability and response strength were called 'super-responding' (SR) neurons and were individually targeted for detailed analysis. In these experiments, the new deep imaging approach was combined with more classical approaches, like single-cell electroporation of a standard calcium dye into a specifically targeted neuron (Tischbirek *et al.*, 2015). In addition, cell-attached recordings and pharmacological manipulations were applied and enabled new insights into single-cell processing of sensory inputs of SR neurons. Based on the experimental results, a likely hypothesis of intracellular processes of the slender-tufted SR neurons during sensory stimulation is the following: Sensory inputs to the basal dendrites induce somatic firing, which facilitates dendritic spiking of the tuft dendrites (Larkum *et al.*, 1999a; Larkum *et al.*, 1999b). Coincident synaptic inputs to the tuft initiate dendritic calcium spikes, which in turn amplify the somatic output. The functional role of SR neurons in layer 5 could be versatile. They could simply integrate touch and motion signals, serve to

consciously perceive sensory stimuli or take part in creating an internal self-body picture to interpret and simulate body actions.

6 Acknowledgements

7 References

Akemann W, Sasaki M, Mutoh H, Imamura T, Honkura N & Knopfel T. (2013). Two-photon voltage imaging using a genetically encoded voltage indicator. *Scientific reports* **3,** 2231.

Akerboom J, Carreras Calderon N, Tian L, Wabnig S, Prigge M, Tolo J, Gordus A, Orger MB, Severi KE, Macklin JJ, Patel R, Pulver SR, Wardill TJ, Fischer E, Schuler C, Chen TW, Sarkisyan KS, Marvin JS, Bargmann CI, Kim DS, Kugler S, Lagnado L, Hegemann P, Gottschalk A, Schreiter ER & Looger LL. (2013). Genetically encoded calcium indicators for multi-color neural activity imaging and combination with optogenetics. *Front Mol Neurosci* **6,** 2.

Albota MA, Xu C & Webb WW. (1998). Two-Photon Fluorescence Excitation Cross Sections of Biomolecular Probes from 690 to 960 nm. *Appl Opt* **37,** 7352-7356.

Andermann ML, Gilfoy NB, Goldey GJ, Sachdev RN, Wolfel M, McCormick DA, Reid RC & Levene MJ. (2013). Chronic cellular imaging of entire cortical columns in awake mice using microprisms. *Neuron* **80,** 900-913.

Aronoff R, Matyas F, Mateo C, Ciron C, Schneider B & Petersen CC. (2010). Long-range connectivity of mouse primary somatosensory barrel cortex. *Eur J Neurosci* **31,** 2221-2233.

Balu M, Baldacchini T, Carter J, Krasieva TB, Zadoyan R & Tromberg BJ. (2009). Effect of excitation wavelength on penetration depth in nonlinear optical microscopy of turbid media. *J Biomed Opt* **14,** 010508.

Becker W, Su B, Holub O & Weisshart K. (2011). FLIM and FCS detection in laser-scanning microscopes: increased efficiency by GaAsP hybrid detectors. *Microsc Res Tech* **74,** 804-811.

Bennett C, Arroyo S & Hestrin S. (2013). Subthreshold mechanisms underlying state-dependent modulation of visual responses. *Neuron* **80,** 350-357.

Berridge MJ, Lipp P & Bootman MD. (2000). The versatility and universality of calcium signalling. *Nat Rev Mol Cell Biol* **1,** 11-21.

Bethge P, Carta S, Lorenzo DA, Egolf L, Goniotaki D, Madisen L, Voigt FF, Chen JL, Schneider B, Ohkura M, Nakai J, Zeng H, Aguzzi A & Helmchen F. (2017). An R-CaMP1.07 reporter mouse for cell-type-specific expression of a sensitive red fluorescent calcium indicator. *PLoS One* **12,** e0179460.

Birkner A, Tischbirek CH & Konnerth A. (2017). Improved deep two-photon calcium imaging in vivo. *Cell Calcium* **64,** 29-35.

Bocarsly ME, Jiang WC, Wang C, Dudman JT, Ji N & Aponte Y. (2015). Minimally invasive microendoscopy system for in vivo functional imaging of deep nuclei in the mouse brain. *Biomed Opt Express* **6,** 4546-4556.

Bosman LW, Houweling AR, Owens CB, Tanke N, Shevchouk OT, Rahmati N, Teunissen WH, Ju C, Gong W, Koekkoek SK & De Zeeuw CI. (2011). Anatomical pathways involved in generating and sensing rhythmic whisker movements. *Front Integr Neurosci* **5,** 53.

Brecht M. (2017). The Body Model Theory of Somatosensory Cortex. *Neuron* **94,** 985-992.

Brecht M, Preilowski B & Merzenich MM. (1997). Functional architecture of the mystacial vibrissae. *Behav Brain Res* **84,** 81-97.

Brodmann K. (1909). *Vergleichende Lokalisationslehre der Grosshirnrinde in ihren Prinzipien dargestellt auf Grund des Zellenbaues von Dr. K. Brodmann*. J.A. Barth.

Bruno RM, Hahn TT, Wallace DJ, de Kock CP & Sakmann B. (2009). Sensory experience alters specific branches of individual corticocortical axons during development. *J Neurosci* **29,** 3172-3181.

Brustein E, Marandi N, Kovalchuk Y, Drapeau P & Konnerth A. (2003). "In vivo" monitoring of neuronal network activity in zebrafish by two-photon Ca(2+) imaging. *Pflugers Arch* **446,** 766-773.

Busche MA, Eichhoff G, Adelsberger H, Abramowski D, Wiederhold KH, Haass C, Staufenbiel M, Konnerth A & Garaschuk O. (2008). Clusters of hyperactive neurons near amyloid plaques in a mouse model of Alzheimer's disease. *Science* **321,** 1686-1689.

Buzsaki G & Mizuseki K. (2014). The log-dynamic brain: how skewed distributions affect network operations. *Nat Rev Neurosci* **15,** 264-278.

Callaway EM. (2004). Feedforward, feedback and inhibitory connections in primate visual cortex. *Neural Netw* **17,** 625-632.

Cauller LJ, Clancy B & Connors BW. (1998). Backward cortical projections to primary somatosensory cortex in rats extend long horizontal axons in layer I. *J Comp Neurol* **390,** 297-310.

Chagnac-Amitai Y, Luhmann HJ & Prince DA. (1990). Burst generating and regular spiking layer 5 pyramidal neurons of rat neocortex have different morphological features. *J Comp Neurol* **296,** 598-613.

Chaigneau E, Wright AJ, Poland SP, Girkin JM & Silver RA. (2011). Impact of wavefront distortion and scattering on 2-photon microscopy in mammalian brain tissue. *Opt Express* **19,** 22755-22774.

Chen TW, Wardill TJ, Sun Y, Pulver SR, Renninger SL, Baohan A, Schreiter ER, Kerr RA, Orger MB, Jayaraman V, Looger LL, Svoboda K & Kim DS. (2013). Ultrasensitive fluorescent proteins for imaging neuronal activity. *Nature* **499,** 295-300.

Chen X, Leischner U, Rochefort NL, Nelken I & Konnerth A. (2011). Functional mapping of single spines in cortical neurons in vivo. *Nature* **475,** 501-505.

Chen X, Leischner U, Varga Z, Jia H, Deca D, Rochefort NL & Konnerth A. (2012a). LOTOS-based two-photon calcium imaging of dendritic spines in vivo. *Nat Protoc* **7,** 1818-1829.

Chen Z, Wei L, Zhu X & Min W. (2012b). Extending the fundamental imaging-depth limit of multi-photon microscopy by imaging with photo-activatable fluorophores. *Opt Express* **20,** 18525-18536.

Cheng A, Goncalves JT, Golshani P, Arisaka K & Portera-Cailliau C. (2011). Simultaneous two-photon calcium imaging at different depths with spatiotemporal multiplexing. *Nat Methods* **8,** 139-142.

Chia TH & Levene MJ. (2009). Microprisms for in vivo multilayer cortical imaging. *J Neurophysiol* **102,** 1310-1314.

Cichon J & Gan WB. (2015). Branch-specific dendritic Ca(2+) spikes cause persistent synaptic plasticity. *Nature* **520,** 180-185.

Collot M, Loukou C, Yakovlev AV, Wilms CD, Li D, Evrard A, Zamaleeva A, Bourdieu L, Leger JF, Ropert N, Eilers J, Oheim M, Feltz A & Mallet JM. (2012). Calcium rubies: a family of red-emitting functionalizable indicators suitable for two-photon Ca2+ imaging. *J Am Chem Soc* **134,** 14923-14931.

Collot M, Wilms CD, Bentkhayet A, Marcaggi P, Couchman K, Charpak S, Dieudonne S, Hausser M, Feltz A & Mallet JM. (2015). CaRuby-Nano: a novel high affinity calcium probe for dual color imaging. *Elife* **4**.

Constantinople CM & Bruno RM. (2013). Deep cortical layers are activated directly by thalamus. *Science* **340,** 1591-1594.

Curtis JC & Kleinfeld D. (2009). Phase-to-rate transformations encode touch in cortical neurons of a scanning sensorimotor system. *Nat Neurosci* **12,** 492-501.

Dadarlat MC & Stryker MP. (2017). Locomotion Enhances Neural Encoding of Visual Stimuli in Mouse V1. *J Neurosci* **37,** 3764-3775.

Dana H, Mohar B, Sun Y, Narayan S, Gordus A, Hasseman JP, Tsegaye G, Holt GT, Hu A, Walpita D, Patel R, Macklin JJ, Bargmann CI, Ahrens MB, Schreiter ER, Jayaraman V, Looger LL, Svoboda K & Kim DS. (2016). Sensitive red protein calcium indicators for imaging neural activity. *Elife* **5**.

de Kock CP, Bruno RM, Spors H & Sakmann B. (2007). Layer- and cell-type-specific suprathreshold stimulus representation in rat primary somatosensory cortex. *J Physiol* **581,** 139-154.

de Kock CP & Sakmann B. (2008). High frequency action potential bursts (>or= 100 Hz) in L2/3 and L5B thick tufted neurons in anaesthetized and awake rat primary somatosensory cortex. *J Physiol* **586,** 3353-3364.

de Kock CP & Sakmann B. (2009). Spiking in primary somatosensory cortex during natural whisking in awake head-restrained rats is cell-type specific. *Proc Natl Acad Sci U S A* **106,** 16446-16450.

Denk W, D. W. Piston, and W. W. Webb. (2006). Multi-Photon Molecular Excitation in Laser-Scanning Microscopy. In *Handbook of Biological Confocal Microscopy*, Third Edition. edn, ed. Pawley JB & SpringerLink (Online service), pp. 1 online resource. Springer-Verlag US,, Boston, MA.

Denk W, Strickler JH & Webb WW. (1990). Two-photon laser scanning fluorescence microscopy. *Science* **248,** 73-76.

Douglas RJ & Martin KA. (2004). Neuronal circuits of the neocortex. *Annu Rev Neurosci* **27,** 419-451.

Duemani Reddy G, Kelleher K, Fink R & Saggau P. (2008). Three-dimensional random access multiphoton microscopy for functional imaging of neuronal activity. *Nat Neurosci* **11,** 713-720.

Dunn AK, Wallace VP, Coleno M, Berns MW & Tromberg BJ. (2000). Influence of optical properties on two-photon fluorescence imaging in turbid samples. *Appl Opt* **39,** 1194-1201.

Durand S, Iyer R, Mizuseki K, de Vries S, Mihalas S & Reid RC. (2016). A Comparison of Visual Response Properties in the Lateral Geniculate Nucleus and Primary Visual Cortex of Awake and Anesthetized Mice. *J Neurosci* **36,** 12144-12156.

Ebara S, Kumamoto K, Matsuura T, Mazurkiewicz JE & Rice FL. (2002). Similarities and differences in the innervation of mystacial vibrissal follicle-sinus complexes in the rat and cat: a confocal microscopic study. *J Comp Neurol* **449,** 103-119.

Egawa T, Hanaoka K, Koide Y, Ujita S, Takahashi N, Ikegaya Y, Matsuki N, Terai T, Ueno T, Komatsu T & Nagano T. (2011a). Development of a far-red to near-infrared fluorescence probe for calcium ion and its application to multicolor neuronal imaging. *J Am Chem Soc* **133,** 14157-14159.

Egawa T, Koide Y, Hanaoka K, Komatsu T, Terai T & Nagano T. (2011b). Development of a fluorescein analogue, TokyoMagenta, as a novel scaffold for fluorescence probes in red region. *Chem Commun (Camb)* **47,** 4162-4164.

Eilers J & Konnerth A. (2009). Dye loading with patch pipettes. *Cold Spring Harb Protoc* **2009,** pdb prot5201.

Fahrbach FO, Simon P & Rohrbach A. (2010). Microscopy with self-reconstructing beams. *Nature Photonics* **4,** 780-785.

Feldmeyer D. (2012). Excitatory neuronal connectivity in the barrel cortex. *Front Neuroanat* **6,** 24.

Feldmeyer D, Brecht M, Helmchen F, Petersen CC, Poulet JF, Staiger JF, Luhmann HJ & Schwarz C. (2013). Barrel cortex function. *Prog Neurobiol* **103,** 3-27.

Feldmeyer D, Lubke J & Sakmann B. (2006). Efficacy and connectivity of intracolumnar pairs of layer 2/3 pyramidal cells in the barrel cortex of juvenile rats. *J Physiol* **575,** 583-602.

Flusberg BA, Cocker ED, Piyawattanametha W, Jung JC, Cheung EL & Schnitzer MJ. (2005). Fiber-optic fluorescence imaging. *Nat Methods* **2,** 941-950.

Fox K. (2009). *Barrel cortex*. Cambridge University Press

Fu Y, Tucciarone JM, Espinosa JS, Sheng N, Darcy DP, Nicoll RA, Huang ZJ & Stryker MP. (2014). A cortical circuit for gain control by behavioral state. *Cell* **156,** 1139-1152.

Fukasawa A, Haba J, Kageyama A, Nakazawa H & Suyama M. (2008). High speed HPD for photon counting. *Ieee T Nucl Sci* **55,** 758-762.

Garaschuk O, Milos RI & Konnerth A. (2006). Targeted bulk-loading of fluorescent indicators for two-photon brain imaging in vivo. *Nat Protoc* **1,** 380-386.

Gilbert CD & Sigman M. (2007). Brain states: top-down influences in sensory processing. *Neuron* **54,** 677-696.

Gilbert CD & Wiesel TN. (1979). Morphology and intracortical projections of functionally characterised neurones in the cat visual cortex. *Nature* **280,** 120-125.

Goeppert-Mayer M. (1931). Über Elementarakte mit zwei Quantensprüngen. *Annals of Physics* **401,** 273-294.

Golding NL, Jung HY, Mickus T & Spruston N. (1999). Dendritic calcium spike initiation and repolarization are controlled by distinct potassium channel subtypes in CA1 pyramidal neurons. *J Neurosci* **19,** 8789-8798.

Golding NL & Spruston N. (1998). Dendritic sodium spikes are variable triggers of axonal action potentials in hippocampal CA1 pyramidal neurons. *Neuron* **21,** 1189-1200.

Gong S, Doughty M, Harbaugh CR, Cummins A, Hatten ME, Heintz N & Gerfen CR. (2007). Targeting Cre recombinase to specific neuron populations with bacterial artificial chromosome constructs. *J Neurosci* **27,** 9817-9823.

Gong Y, Huang C, Li JZ, Grewe BF, Zhang Y, Eismann S & Schnitzer MJ. (2015). High-speed recording of neural spikes in awake mice and flies with a fluorescent voltage sensor. *Science* **350,** 1361-1366.

Grewe BF, Bonnan A & Frick A. (2010). Back-Propagation of Physiological Action Potential Output in Dendrites of Slender-Tufted L5A Pyramidal Neurons. *Front Cell Neurosci* **4,** 13.

Grewe BF, Grundemann J, Kitch LJ, Lecoq JA, Parker JG, Marshall JD, Larkin MC, Jercog PE, Grenier F, Li JZ, Luthi A & Schnitzer MJ. (2017). Neural ensemble dynamics underlying a long-term associative memory. *Nature* **543,** 670-675.

Grienberger C, Chen X & Konnerth A. (2014). NMDA receptor-dependent multidendrite Ca(2+) spikes required for hippocampal burst firing in vivo. *Neuron* **81,** 1274-1281.

Grienberger C & Konnerth A. (2012). Imaging calcium in neurons. *Neuron* **73,** 862-885.

Groh A, Meyer HS, Schmidt EF, Heintz N, Sakmann B & Krieger P. (2010). Cell-type specific properties of pyramidal neurons in neocortex underlying a layout that is modifiable depending on the cortical area. *Cereb Cortex* **20,** 826-836.

Guan D, Armstrong WE & Foehring RC. (2015). Electrophysiological properties of genetically identified subtypes of layer 5 neocortical pyramidal neurons: Ca(2)(+) dependence and differential modulation by norepinephrine. *J Neurophysiol* **113,** 2014-2032.

Haider B, Hausser M & Carandini M. (2013). Inhibition dominates sensory responses in the awake cortex. *Nature* **493,** 97-100.

Harnett MT, Xu NL, Magee JC & Williams SR. (2013). Potassium channels control the interaction between active dendritic integration compartments in layer 5 cortical pyramidal neurons. *Neuron* **79,** 516-529.

Harris KD & Shepherd GM. (2015). The neocortical circuit: themes and variations. *Nat Neurosci* **18,** 170-181.

Hattox AM & Nelson SB. (2007). Layer V neurons in mouse cortex projecting to different targets have distinct physiological properties. *J Neurophysiol* **98,** 3330-3340.

Helmchen F & Denk W. (2005). Deep tissue two-photon microscopy. *Nat Methods* **2,** 932-940.

Helmchen F, Svoboda K, Denk W & Tank DW. (1999). In vivo dendritic calcium dynamics in deep-layer cortical pyramidal neurons. *Nat Neurosci* **2,** 989-996.

Hires SA, Gutnisky DA, Yu J, O'Connor DH & Svoboda K. (2015). Low-noise encoding of active touch by layer 4 in the somatosensory cortex. *Elife* **4**.

Holthoff K, Kovalchuk Y & Konnerth A. (2006). Dendritic spikes and activity-dependent synaptic plasticity. *Cell Tissue Res* **326,** 369-377.

Holtmaat A & Svoboda K. (2009). Experience-dependent structural synaptic plasticity in the mammalian brain. *Nat Rev Neurosci* **10,** 647-658.

Horton NG, Wang K, Kobat D, Clark CG, Wise FW, Schaffer CB & Xu C. (2013a). In vivo three-photon microscopy of subcortical structures within an intact mouse brain. *Nat Photonics* **7**.

Horton NG, Wang K, Kobat D, Clark CG, Wise FW, Schaffer CB & Xu C. (2013b). three-photon microscopy of subcortical structures within an intact mouse brain. *Nat Photonics* **7**.

Hromadka T, Deweese MR & Zador AM. (2008). Sparse representation of sounds in the unanesthetized auditory cortex. *PLoS Biol* **6,** e16.

Hubel DH. (1957). Tungsten Microelectrode for Recording from Single Units. *Science* **125,** 549-550.

Hubel DH & Wiesel TN. (1959). Receptive fields of single neurones in the cat's striate cortex. *J Physiol* **148,** 574-591.

Hubel DH & Wiesel TN. (1968). Receptive fields and functional architecture of monkey striate cortex. *J Physiol* **195,** 215-243.

Hubel DH & Wiesel TN. (1969). Anatomical demonstration of columns in the monkey striate cortex. *Nature* **221,** 747-750.

Husson RTaI, Naoum P. (2009). Functional Imaging with Mitochondrial Flavoprotein Autofluorescence: Theory, Practice, and Applications. In *In Vivo Optical Imaging of Brain Function 2nd edition*, pp. 259 pages.

Hyrc KL, Minta A, Escamilla PR, Chan PP, Meshik XA & Goldberg MP. (2013). Synthesis and properties of Asante Calcium Red--a novel family of long excitation wavelength calcium indicators. *Cell Calcium* **54,** 320-333.

Inoue M, Takeuchi A, Horigane S, Ohkura M, Gengyo-Ando K, Fujii H, Kamijo S, Takemoto-Kimura S, Kano M, Nakai J, Kitamura K & Bito H. (2015). Rational design of a high-affinity, fast, red calcium indicator R-CaMP2. *Nat Methods* **12,** 64-70.

Jacques SL. (2013). Optical properties of biological tissues: a review. *Phys Med Biol* **58,** R37-61.

Ji N. (2014). The practical and fundamental limits of optical imaging in mammalian brains. *Neuron* **83,** 1242-1245.

Ji N. (2017). Adaptive optical fluorescence microscopy. *Nat Methods* **14,** 374-380.

Jia H, Rochefort NL, Chen X & Konnerth A. (2010). Dendritic organization of sensory input to cortical neurons in vivo. *Nature* **464,** 1307-1312.

Jia H, Varga Z, Sakmann B & Konnerth A. (2014). Linear integration of spine Ca2+ signals in layer 4 cortical neurons in vivo. *Proc Natl Acad Sci U S A* **111,** 9277-9282.

Jung JC, Mehta AD, Aksay E, Stepnoski R & Schnitzer MJ. (2004). In vivo mammalian brain imaging using one- and two-photon fluorescence microendoscopy. *J Neurophysiol* **92,** 3121-3133.

Kaiser W & Garrett CGB. (1961). Two-Photon Excitation in CaF2: Eu2+. *Phys Rev Lett* **7,** 229-231.

Kapusta P, Wahl M & Erdmann R. (2015). *Advanced Photon Counting : Applications, Methods, Instrumentation*. Springer International Publishing : Imprint: Springer, Cham.

Keller GB, Bonhoeffer T & Hubener M. (2012). Sensorimotor mismatch signals in primary visual cortex of the behaving mouse. *Neuron* **74,** 809-815.

Khateb M, Schiller J & Schiller Y. (2017). Feedforward motor information enhances somatosensory responses and sharpens angular tuning of rat S1 barrel cortex neurons. *Elife* **6**.

Kim EJ, Juavinett AL, Kyubwa EM, Jacobs MW & Callaway EM. (2015). Three Types of Cortical Layer 5 Neurons That Differ in Brain-wide Connectivity and Function. *Neuron* **88,** 1253-1267.

Kitamura K, Judkewitz B, Kano M, Denk W & Hausser M. (2008). Targeted patch-clamp recordings and single-cell electroporation of unlabeled neurons in vivo. *Nat Methods* **5,** 61-67.

Kobat D, Durst ME, Nishimura N, Wong AW, Schaffer CB & Xu C. (2009). Deep tissue multiphoton microscopy using longer wavelength excitation. *Opt Express* **17,** 13354-13364.

Kobat D, Horton NG & Xu C. (2011). In vivo two-photon microscopy to 1.6-mm depth in mouse cortex. *J Biomed Opt* **16,** 106014.

Kondo M, Kobayashi K, Ohkura M, Nakai J & Matsuzaki M. (2017). Two-photon calcium imaging of the medial prefrontal cortex and hippocampus without cortical invasion. *Elife* **6**.

Kwon SE, Yang H, Minamisawa G & O'Connor DH. (2016). Sensory and decision-related activity propagate in a cortical feedback loop during touch perception. *Nat Neurosci* **19,** 1243-1249.

Larkum ME, Kaiser KM & Sakmann B. (1999a). Calcium electrogenesis in distal apical dendrites of layer 5 pyramidal cells at a critical frequency of back-propagating action potentials. *Proc Natl Acad Sci U S A* **96,** 14600-14604.

Larkum ME, Nevian T, Sandler M, Polsky A & Schiller J. (2009). Synaptic integration in tuft dendrites of layer 5 pyramidal neurons: a new unifying principle. *Science* **325,** 756-760.

Larkum ME & Zhu JJ. (2002). Signaling of layer 1 and whisker-evoked Ca2+ and Na+ action potentials in distal and terminal dendrites of rat neocortical pyramidal neurons in vitro and in vivo. *J Neurosci* **22,** 6991-7005.

Larkum ME, Zhu JJ & Sakmann B. (1999b). A new cellular mechanism for coupling inputs arriving at different cortical layers. *Nature* **398,** 338-341.

Larkum ME, Zhu JJ & Sakmann B. (2001). Dendritic mechanisms underlying the coupling of the dendritic with the axonal action potential initiation zone of adult rat layer 5 pyramidal neurons. *J Physiol* **533,** 447-466.

Larsen DD & Callaway EM. (2006). Development of layer-specific axonal arborizations in mouse primary somatosensory cortex. *J Comp Neurol* **494,** 398-414.

Lavallee P, Urbain N, Dufresne C, Bokor H, Acsady L & Deschenes M. (2005). Feedforward inhibitory control of sensory information in higher-order thalamic nuclei. *J Neurosci* **25,** 7489-7498.

Lavzin M, Rapoport S, Polsky A, Garion L & Schiller J. (2012). Nonlinear dendritic processing determines angular tuning of barrel cortex neurons in vivo. *Nature* **490,** 397-401.

Lefort S, Tomm C, Floyd Sarria JC & Petersen CC. (2009). The excitatory neuronal network of the C2 barrel column in mouse primary somatosensory cortex. *Neuron* **61,** 301-316.

Leray A, Lillis K & Mertz J. (2008). Enhanced background rejection in thick tissue with differential-aberration two-photon microscopy. *Biophys J* **94,** 1449-1458.

Leray A & Mertz J. (2006). Rejection of two-photon fluorescence background in thick tissue by differential aberration imaging. *Opt Express* **14,** 10565-10573.

Leybaert L, de Meyer A, Mabilde C & Sanderson MJ. (2005). A simple and practical method to acquire geometrically correct images with resonant scanning-based line scanning in a custom-built video-rate laser scanning microscope. *J Microsc* **219,** 133-140.

London M & Hausser M. (2005). Dendritic computation. *Annu Rev Neurosci* **28,** 503-532.

Longair MH, Baker DA & Armstrong JD. (2011). Simple Neurite Tracer: open source software for reconstruction, visualization and analysis of neuronal processes. *Bioinformatics* **27,** 2453-2454.

Low RJ, Gu Y & Tank DW. (2014). Cellular resolution optical access to brain regions in fissures: imaging medial prefrontal cortex and grid cells in entorhinal cortex. *Proc Natl Acad Sci U S A* **111,** 18739-18744.

Magee JC. (2000). Dendritic integration of excitatory synaptic input. *Nat Rev Neurosci* **1,** 181-190.

Maiman TH. (1960). Stimulated Optical Radiation in Ruby. *Nature* **187,** 493 - 494.

Major G, Larkum ME & Schiller J. (2013). Active properties of neocortical pyramidal neuron dendrites. *Annu Rev Neurosci* **36,** 1-24.

Manita S, Suzuki T, Homma C, Matsumoto T, Odagawa M, Yamada K, Ota K, Matsubara C, Inutsuka A, Sato M, Ohkura M, Yamanaka A, Yanagawa Y, Nakai J, Hayashi Y, Larkum ME & Murayama M. (2015). A Top-Down Cortical Circuit for Accurate Sensory Perception. *Neuron* **86,** 1304-1316.

Mank M & Griesbeck O. (2008). Genetically encoded calcium indicators. *Chem Rev* **108,** 1550-1564.

Manns ID, Sakmann B & Brecht M. (2004). Sub- and suprathreshold receptive field properties of pyramidal neurones in layers 5A and 5B of rat somatosensory barrel cortex. *J Physiol* **556,** 601-622.

Mao T, Kusefoglu D, Hooks BM, Huber D, Petreanu L & Svoboda K. (2011). Long-range neuronal circuits underlying the interaction between sensory and motor cortex. *Neuron* **72,** 111-123.

Margrie TW, Brecht M & Sakmann B. (2002). In vivo, low-resistance, whole-cell recordings from neurons in the anaesthetized and awake mammalian brain. *Pflugers Arch* **444,** 491-498.

Markram H, Toledo-Rodriguez M, Wang Y, Gupta A, Silberberg G & Wu C. (2004). Interneurons of the neocortical inhibitory system. *Nat Rev Neurosci* **5,** 793-807.

Masters BR & So PTC. (2008). *Handbook of biomedical nonlinear optical microscopy*. Oxford University Press, New York.

Meyer HS, Egger R, Guest JM, Foerster R, Reissl S & Oberlaender M. (2013). Cellular organization of cortical barrel columns is whisker-specific. *Proc Natl Acad Sci U S A* **110,** 19113-19118.

Minta A, Kao JP & Tsien RY. (1989). Fluorescent indicators for cytosolic calcium based on rhodamine and fluorescein chromophores. *J Biol Chem* **264,** 8171-8178.

Mittmann W, Wallace DJ, Czubayko U, Herb JT, Schaefer AT, Looger LL, Denk W & Kerr JN. (2011). Two-photon calcium imaging of evoked activity from L5 somatosensory neurons in vivo. *Nat Neurosci* **14,** 1089-1093.

Mizuseki K & Buzsaki G. (2013). Preconfigured, skewed distribution of firing rates in the hippocampus and entorhinal cortex. *Cell Rep* **4,** 1010-1021.

Mountcastle VB. (1997). The columnar organization of the neocortex. *Brain* **120 (Pt 4),** 701-722.

Muller M, Squier J, Wolleschensky R, Simon U & Brakenhoff GJ. (1998). Dispersion pre-compensation of 15 femtosecond optical pulses for high-numerical-aperture objectives. *J Microsc* **191,** 141-150.

Mutze J, Iyer V, Macklin JJ, Colonell J, Karsh B, Petrasek Z, Schwille P, Looger LL, Lavis LD & Harris TD. (2012). Excitation spectra and brightness optimization of two-photon excited probes. *Biophys J* **102,** 934-944.

Nachabe R, Evers DJ, Hendriks BH, Lucassen GW, van der Voort M, Wesseling J & Ruers TJ. (2011). Effect of bile absorption coefficients on the estimation of liver tissue optical properties and related implications in discriminating healthy and tumorous samples. *Biomed Opt Express* **2,** 600-614.

Nadella KM, Ros H, Baragli C, Griffiths VA, Konstantinou G, Koimtzis T, Evans GJ, Kirkby PA & Silver RA. (2016). Random-access scanning microscopy for 3D imaging in awake behaving animals. *Nat Methods* **13,** 1001-1004.

Nevian T & Helmchen F. (2007). Calcium indicator loading of neurons using single-cell electroporation. *Pflugers Arch* **454,** 675-688.

Niell CM & Stryker MP. (2008). Highly selective receptive fields in mouse visual cortex. *J Neurosci* **28,** 7520-7536.

Niell CM & Stryker MP. (2010). Modulation of visual responses by behavioral state in mouse visual cortex. *Neuron* **65,** 472-479.

Nimmerjahn A, Kirchhoff F, Kerr JN & Helmchen F. (2004). Sulforhodamine 101 as a specific marker of astroglia in the neocortex in vivo. *Nat Methods* **1,** 31-37.

O'Connor DH, Peron SP, Huber D & Svoboda K. (2010). Neural activity in barrel cortex underlying vibrissa-based object localization in mice. *Neuron* **67,** 1048-1061.

Oberlaender M, Boudewijns ZS, Kleele T, Mansvelder HD, Sakmann B & de Kock CP. (2011). Three-dimensional axon morphologies of individual layer 5 neurons indicate cell type-specific intracortical pathways for whisker motion and touch. *Proc Natl Acad Sci U S A* **108,** 4188-4193.

Oheim M, Beaurepaire E, Chaigneau E, Mertz J & Charpak S. (2001). Two-photon microscopy in brain tissue: parameters influencing the imaging depth. *J Neurosci Methods* **111,** 29-37.

Oheim M, van 't Hoff M, Feltz A, Zamaleeva A, Mallet JM & Collot M. (2014). New red-fluorescent calcium indicators for optogenetics, photoactivation and multi-color imaging. *Biochimica et biophysica acta* **1843,** 2284-2306.

Ohkura M, Sasaki T, Kobayashi C, Ikegaya Y & Nakai J. (2012). An improved genetically encoded red fluorescent Ca2+ indicator for detecting optically evoked action potentials. *PLoS One* **7,** e39933.

Ouzounov DG, Wang T, Wang M, Feng DD, Horton NG, Cruz-Hernandez JC, Cheng YT, Reimer J, Tolias AS, Nishimura N & Xu C. (2017). In vivo three-photon imaging of activity of GCaMP6-labeled neurons deep in intact mouse brain. *Nat Methods* **14,** 388-390.

Packer AM, Russell LE, Dalgleish HW & Hausser M. (2015). Simultaneous all-optical manipulation and recording of neural circuit activity with cellular resolution in vivo. *Nat Methods* **12,** 140-146.

Pakan JM, Lowe SC, Dylda E, Keemink SW, Currie SP, Coutts CA & Rochefort NL. (2016). Behavioral-state modulation of inhibition is context-dependent and cell type specific in mouse visual cortex. *Elife* **5**.

Palmer LM, Shai AS, Reeve JE, Anderson HL, Paulsen O & Larkum ME. (2014). NMDA spikes enhance action potential generation during sensory input. *Nat Neurosci* **17,** 383-390.

Paredes RM, Etzler JC, Watts LT, Zheng W & Lechleiter JD. (2008). Chemical calcium indicators. *Methods* **46,** 143-151.

Pawley JB. (2006). Handbook of biological confocal microscopy. 3rd edn, pp. 29. Springer, New York, NY.

Perez-Garci E, Larkum ME & Nevian T. (2013). Inhibition of dendritic Ca2+ spikes by GABAB receptors in cortical pyramidal neurons is mediated by a direct Gi/o-beta-subunit interaction with Cav1 channels. *J Physiol* **591,** 1599-1612.

Peterka DS, Takahashi H & Yuste R. (2011). Imaging voltage in neurons. *Neuron* **69,** 9-21.

Petersen CC. (2007). The functional organization of the barrel cortex. *Neuron* **56,** 339-355.

Petersen CC & Sakmann B. (2000). The excitatory neuronal network of rat layer 4 barrel cortex. *J Neurosci* **20,** 7579-7586.

Petreanu L, Mao T, Sternson SM & Svoboda K. (2009). The subcellular organization of neocortical excitatory connections. *Nature* **457,** 1142-1145.

Pierret T, Lavallee P & Deschenes M. (2000). Parallel streams for the relay of vibrissal information through thalamic barreloids. *J Neurosci* **20,** 7455-7462.

Pilz GA, Carta S, Stauble A, Ayaz A, Jessberger S & Helmchen F. (2016). Functional Imaging of Dentate Granule Cells in the Adult Mouse Hippocampus. *J Neurosci* **36,** 7407-7414.

Polack PO, Friedman J & Golshani P. (2013). Cellular mechanisms of brain state-dependent gain modulation in visual cortex. *Nat Neurosci* **16,** 1331-1339.

Ponsot F, Shen W, Ashokkumar P, Audinat E, Klymchenko AS & Collot M. (2017). PEGylated Red-Emitting Calcium Probe with Improved Sensing Properties for Neuroscience. *ACS Sens* **2,** 1706-1712.

Rall W. (1967). Distinguishing theoretical synaptic potentials computed for different soma-dendritic distributions of synaptic input. *J Neurophysiol* **30,** 1138-1168.

Rall W, Burke RE, Smith TG, Nelson PG & Frank K. (1967). Dendritic location of synapses and possible mechanisms for the monosynaptic EPSP in motoneurons. *J Neurophysiol* **30,** 1169-1193.

Rall W & Rinzel J. (1973). Branch input resistance and steady attenuation for input to one branch of a dendritic neuron model. *Biophys J* **13,** 648-687.

Reimer J, Froudarakis E, Cadwell CR, Yatsenko D, Denfield GH & Tolias AS. (2014). Pupil fluctuations track fast switching of cortical states during quiet wakefulness. *Neuron* **84,** 355-362.

Rochefort NL, Jia H & Konnerth A. (2008). Calcium imaging in the living brain: prospects for molecular medicine. *Trends Mol Med* **14,** 389-399.

Rose CR, Kovalchuk Y, Eilers J & Konnerth A. (1999). Two-photon Na+ imaging in spines and fine dendrites of central neurons. *Pflugers Arch* **439,** 201-207.

Rose T, Goltstein PM, Portugues R & Griesbeck O. (2014). Putting a finishing touch on GECIs. *Front Mol Neurosci* **7,** 88.

Rudy B, Fishell G, Lee S & Hjerling-Leffler J. (2011). Three groups of interneurons account for nearly 100% of neocortical GABAergic neurons. *Dev Neurobiol* **71,** 45-61.

Sachidhanandam S, Sreenivasan V, Kyriakatos A, Kremer Y & Petersen CC. (2013). Membrane potential correlates of sensory perception in mouse barrel cortex. *Nat Neurosci* **16,** 1671-1677.

Sakata S & Harris KD. (2009). Laminar structure of spontaneous and sensory-evoked population activity in auditory cortex. *Neuron* **64,** 404-418.

Sakmann B & Neher E. (1984). Patch clamp techniques for studying ionic channels in excitable membranes. *Annu Rev Physiol* **46,** 455-472.

Saleem AB, Ayaz A, Jeffery KJ, Harris KD & Carandini M. (2013). Integration of visual motion and locomotion in mouse visual cortex. *Nat Neurosci* **16,** 1864-1869.

Sasaki T, Matsuki N & Ikegaya Y. (2012). Targeted axon-attached recording with fluorescent patch-clamp pipettes in brain slices. *Nat Protoc* **7,** 1228-1234.

Schiller J, Schiller Y, Stuart G & Sakmann B. (1997). Calcium action potentials restricted to distal apical dendrites of rat neocortical pyramidal neurons. *J Physiol* **505 (Pt 3),** 605-616.

Sepehri Rad M, Choi Y, Cohen LB, Baker BJ, Zhong S, Storace DA & Braubach OR. (2017). Voltage and Calcium Imaging of Brain Activity. *Biophys J* **113,** 2160-2167.

Sheffield ME & Dombeck DA. (2015). Calcium transient prevalence across the dendritic arbour predicts place field properties. *Nature* **517,** 200-204.

Sheffield MEJ, Adoff MD & Dombeck DA. (2017). Increased Prevalence of Calcium Transients across the Dendritic Arbor during Place Field Formation. *Neuron* **96,** 490-504 e495.

Shen Y, Dana H, Abdelfattah AS, Patel R, Shea J, Molina RS, Rawal B, Rancic V, Chang YF, Wu L, Chen Y, Qian Y, Wiens MD, Hambleton N, Ballanyi K, Hughes TE, Drobizhev M, Kim DS, Koyama M, Schreiter ER & Campbell RE. (2018). A genetically encoded Ca(2+) indicator based on circularly permutated sea anemone red fluorescent protein eqFP578. *BMC Biol* **16,** 9.

Shi L, Sordillo LA, Rodriguez-Contreras A & Alfano R. (2016). Transmission in near-infrared optical windows for deep brain imaging. *J Biophotonics* **9,** 38-43.

Shoham S, O'Connor DH & Segev R. (2006). How silent is the brain: is there a "dark matter" problem in neuroscience? *J Comp Physiol A Neuroethol Sens Neural Behav Physiol* **192,** 777-784.

Simons DJ. (1983). Multi-whisker stimulation and its effects on vibrissa units in rat SmI barrel cortex. *Brain Res* **276,** 178-182.

Smith SL, Smith IT, Branco T & Hausser M. (2013). Dendritic spikes enhance stimulus selectivity in cortical neurons in vivo. *Nature* **503,** 115-120.

So PT, Dong CY, Masters BR & Berland KM. (2000). Two-photon excitation fluorescence microscopy. *Annu Rev Biomed Eng* **2,** 399-429.

Sofroniew NJ, Cohen JD, Lee AK & Svoboda K. (2014). Natural whisker-guided behavior by head-fixed mice in tactile virtual reality. *J Neurosci* **34,** 9537-9550.

Spruston N, Schiller Y, Stuart G & Sakmann B. (1995). Activity-dependent action potential invasion and calcium influx into hippocampal CA1 dendrites. *Science* **268,** 297-300.

Sreenivasan V, Esmaeili V, Kiritani T, Galan K, Crochet S & Petersen CCH. (2016). Movement Initiation Signals in Mouse Whisker Motor Cortex. *Neuron* **92,** 1368-1382.

Storace DA, Braubach OR, Jin L, Cohen LB & Sung U. (2015). Monitoring brain activity with protein voltage and calcium sensors. *Scientific reports* **5,** 10212.

Stosiek C, Garaschuk O, Holthoff K & Konnerth A. (2003). In vivo two-photon calcium imaging of neuronal networks. *Proc Natl Acad Sci U S A* **100,** 7319-7324.

Stuart GJ & Sakmann B. (1994). Active propagation of somatic action potentials into neocortical pyramidal cell dendrites. *Nature* **367,** 69-72.

Stuart GJ & Spruston N. (2015). Dendritic integration: 60 years of progress. *Nat Neurosci* **18,** 1713-1721.

Sun W, Tan Z, Mensh BD & Ji N. (2016). Thalamus provides layer 4 of primary visual cortex with orientation- and direction-tuned inputs. *Nat Neurosci* **19,** 308-315.

Tada M, Takeuchi A, Hashizume M, Kitamura K & Kano M. (2014). A highly sensitive fluorescent indicator dye for calcium imaging of neural activity in vitro and in vivo. *Eur J Neurosci* **39,** 1720-1728.

Takahashi K, Hishida R, Kubota Y, Kudoh M, Takahashi S & Shibuki K. (2006). Transcranial fluorescence imaging of auditory cortical plasticity regulated by acoustic environments in mice. *Eur J Neurosci* **23,** 1365-1376.

Takahashi N, Oertner TG, Hegemann P & Larkum ME. (2016). Active cortical dendrites modulate perception. *Science* **354,** 1587-1590.

Theer P & Denk W. (2006). On the fundamental imaging-depth limit in two-photon microscopy. *J Opt Soc Am A Opt Image Sci Vis* **23,** 3139-3149.

131

Theer P, Hasan MT & Denk W. (2003). Two-photon imaging to a depth of 1000 microm in living brains by use of a Ti:Al2O3 regenerative amplifier. *Opt Lett* **28,** 1022-1024.

Thomas D, Tovey SC, Collins TJ, Bootman MD, Berridge MJ & Lipp P. (2000). A comparison of fluorescent Ca2+ indicator properties and their use in measuring elementary and global Ca2+ signals. *Cell Calcium* **28,** 213-223.

Thomson AM & Lamy C. (2007). Functional maps of neocortical local circuitry. *Front Neurosci* **1,** 19-42.

Tian GF, Takano T, Lin JH, Wang X, Bekar L & Nedergaard M. (2006). Imaging of cortical astrocytes using 2-photon laser scanning microscopy in the intact mouse brain. *Adv Drug Deliv Rev* **58,** 773-787.

Tischbirek C, Birkner A, Jia H, Sakmann B & Konnerth A. (2015). Deep two-photon brain imaging with a red-shifted fluorometric Ca2+ indicator. *Proc Natl Acad Sci U S A* **112,** 11377-11382.

Trageser JC, Burke KA, Masri R, Li Y, Sellers L & Keller A. (2006). State-dependent gating of sensory inputs by zona incerta. *J Neurophysiol* **96,** 1456-1463.

Tsien RY. (1981). A non-disruptive technique for loading calcium buffers and indicators into cells. *Nature* **290,** 527-528.

Turner RW, Meyers DE, Richardson TL & Barker JL. (1991). The site for initiation of action potential discharge over the somatodendritic axis of rat hippocampal CA1 pyramidal neurons. *J Neurosci* **11,** 2270-2280.

Varga Z, Jia H, Sakmann B & Konnerth A. (2011). Dendritic coding of multiple sensory inputs in single cortical neurons in vivo. *Proc Natl Acad Sci U S A* **108,** 15420-15425.

Veinante P & Deschenes M. (1999). Single- and multi-whisker channels in the ascending projections from the principal trigeminal nucleus in the rat. *J Neurosci* **19,** 5085-5095.

Velez-Fort M, Rousseau CV, Niedworok CJ, Wickersham IR, Rancz EA, Brown APY, Strom M & Margrie TW. (2014). The Stimulus Selectivity and Connectivity of Layer Six Principal Cells Reveals Cortical Microcircuits Underlying Visual Processing. *Neuron* **84,** 238.

Viaene AN, Petrof I & Sherman SM. (2011). Synaptic properties of thalamic input to the subgranular layers of primary somatosensory and auditory cortices in the mouse. *J Neurosci* **31,** 12738-12747.

Wang C, Liu R, Milkie DE, Sun W, Tan Z, Kerlin A, Chen TW, Kim DS & Ji N. (2014). Multiplexed aberration measurement for deep tissue imaging in vivo. *Nat Methods* **11,** 1037-1040.

Wang K, Sun W, Richie CT, Harvey BK, Betzig E & Ji N. (2015). Direct wavefront sensing for high-resolution in vivo imaging in scattering tissue. *Nat Commun* **6,** 7276.

Wertz A, Trenholm S, Yonehara K, Hillier D, Raics Z, Leinweber M, Szalay G, Ghanem A, Keller G, Rozsa B, Conzelmann KK & Roska B. (2015). PRESYNAPTIC NETWORKS. Single-cell-initiated monosynaptic tracing reveals layer-specific cortical network modules. *Science* **349,** 70-74.

Williams SR & Stuart GJ. (2000). Site independence of EPSP time course is mediated by dendritic I(h) in neocortical pyramidal neurons. *J Neurophysiol* **83,** 3177-3182.

Wimmer VC, Bruno RM, de Kock CP, Kuner T & Sakmann B. (2010). Dimensions of a projection column and architecture of VPM and POm axons in rat vibrissal cortex. *Cereb Cortex* **20,** 2265-2276.

Woolsey TA & Van der Loos H. (1970). The structural organization of layer IV in the somatosensory region (SI) of mouse cerebral cortex. The description of a cortical field composed of discrete cytoarchitectonic units. *Brain Res* **17,** 205-242.

Xu C & Wise FW. (2013). Recent Advances in Fiber Lasers for Nonlinear Microscopy. *Nat Photonics* **7**.

Xu C, Zipfel W, Shear JB, Williams RM & Webb WW. (1996). Multiphoton fluorescence excitation: new spectral windows for biological nonlinear microscopy. *Proc Natl Acad Sci U S A* **93,** 10763-10768.

Xu J & Stroud R. *Acousto-optic devices : principles, design, and applications*.

Xu NL, Harnett MT, Williams SR, Huber D, O'Connor DH, Svoboda K & Magee JC. (2012). Nonlinear dendritic integration of sensory and motor input during an active sensing task. *Nature* **492,** 247-251.

Xu X, Olivas ND, Ikrar T, Peng T, Holmes TC, Nie Q & Shi Y. (2016). Primary visual cortex shows laminar-specific and balanced circuit organization of excitatory and inhibitory synaptic connectivity. *J Physiol* **594,** 1891-1910.

Yaksi E & Friedrich RW. (2006). Reconstruction of firing rate changes across neuronal populations by temporally deconvolved Ca2+ imaging. *Nat Methods* **3,** 377-383.

Yang H, Kwon SE, Severson KS & O'Connor DH. (2016a). Origins of choice-related activity in mouse somatosensory cortex. *Nat Neurosci* **19,** 127-134.

Yang HH, St-Pierre F, Sun X, Ding X, Lin MZ & Clandinin TR. (2016b). Subcellular Imaging of Voltage and Calcium Signals Reveals Neural Processing In Vivo. *Cell* **166,** 245-257.

Yao J & Wang LV. (2013). Photoacoustic Microscopy. *Laser Photon Rev* **7**.

Yu C, Derdikman D, Haidarliu S & Ahissar E. (2006). Parallel thalamic pathways for whisking and touch signals in the rat. *PLoS Biol* **4,** e124.

Yuste R, MacLean J, Vogelstein J & Paninski L. (2011). Imaging action potentials with calcium indicators. *Cold Spring Harb Protoc* **2011,** 985-989.

Zinter JP & Levene MJ. (2011). Maximizing fluorescence collection efficiency in multiphoton microscopy. *Opt Express* **19,** 15348-15362.

Zipfel WR, Williams RM & Webb WW. (2003). Nonlinear magic: multiphoton microscopy in the biosciences. *Nat Biotechnol* **21,** 1369-1377.

Zong W, Wu R, Li M, Hu Y, Li Y, Li J, Rong H, Wu H, Xu Y, Lu Y, Jia H, Fan M, Zhou Z, Zhang Y, Wang A, Chen L & Cheng H. (2017). Fast high-resolution miniature two-photon microscopy for brain imaging in freely behaving mice. *Nat Methods* **14,** 713-719.

8 Publications

Published:

Tischbirek C (*), Birkner A (*), Jia H, Sakmann B & Konnerth A. (2015). Deep two-photon brain imaging with a red-shifted fluorometric Ca2+ indicator. *Proc Natl Acad Sci U S A* **112,** 11377-11382.

Birkner A (*), Tischbirek CH (*) & Konnerth A. (2017). Improved deep two-photon calcium imaging in vivo. *Cell Calcium* **64,** 29-35.

Tischbirek CH (*), Birkner A (*) & Konnerth A. (2017). In vivo deep two-photon imaging of neural circuits with the fluorescent Ca(2+) indicator Cal-590. *J Physiol* **595,** 3097-3105.

(*) Equal distribution

In preparation:

Birkner A, Varga Z, Bonfardin VD, Tohmi M, Sakmann B & Konnerth A. A subset of 'super-responding' (SR) neurons dominates output signaling in layer 5A of mouse barrel cortex.